TRANSPORT PROPERTIES OF 3D AND 2D DISORDERED ELECTRONIC MATERIALS

by

Anindya Nath

A Dissertation
Submitted to the
Graduate Faculty
of
George Mason University
in Partial Fulfillment of
The Requirements for the Degree
of
Doctor of Philosophy
Electrical and Computer Engineering

Committee:

_____	Dr. Mulpuri V. Rao, Dissertation Director
_____	Dr. D. Kurt Gaskill, Committee Member
_____	Dr. Yuri Mishin, Committee Member
_____	Dr. Qiliang Li, Committee Member
_____	Dr. Dimitris E. Ioannou, Committee Member
_____	Dr. Monson H. Hayes, Department Chair
_____	Dr. Kenneth Ball, Dean, Volgenau School of Engineering
Date: _____	Fall Semester 2014 George Mason University Fairfax, VA

Transport Properties of 3D And 2D Disordered Electronic Materials

A Dissertation submitted in partial fulfillment of the requirements for the degree of Doctor of Philosophy at George Mason University

by

Anindya Nath
Master of Science
George Mason University, 2012

Director: Mulpuri V. Rao, Professor
Department of Electrical and Computer Engineering

Fall Semester 2014
George Mason University
Fairfax, VA

DEDICATION

This is dedicated to the memory of my grandparents Akshay Kumar and Shanti Rani Nath and to my parents Arun Kumar and Bina Pani Nath for their support and endless love.

ACKNOWLEDGEMENTS

During the course of this thesis, I was surrounded by a great team of supervisors, mentors and colleagues. I want to thank my supervisor, Dr. Rao Mulpuri, for supporting me through thick and thin during the last 6½ years. Thank you for being the finest advisors that one could possibly hope for.

I would like to thank my co-adviser Dr. Kurt Gaskill, who helped me through the last three years with sound and practical advice at all times. I am also grateful to him for giving me the freedom to pursue my ideas. Thank you for providing me the opportunity to work in such an exciting field with so many great researchers.

My sincere gratitude to Dr. Roberta Nipoti for being my mentor. Thank you for always being there and answering all my questions.

I benefited greatly from many useful discussions with Dr. Marc Currie in various technical matters.

Dr. Mike Osofsky has been like a mentor for last three years of my research at Naval Research Lab. Thank you for introducing me to the world of disordered electronics.

I am short of words to express my deepest gratitude to my colleagues Dr. Virginia Wheeler, Dr. Nelson Garces, Dr. Zachary Robinson and Dr. Sandra Hernandez for their constant guidance, highly valued advice and suggestions about the research especially when the tasks seemed overwhelming and never-ending. No work is too difficult when one has colleagues and friends like you. Thank you so much for everything.

I would also like to acknowledge my wonderful colleagues and collaborators Dr. Anutosh Chaterjee, Dr. Rajib Banerjee, Dr. S.B.Qadri, Dr. Andrew Koehler, Dr. Raffale Scaburri, Dr. Marko Tadjer, Dr. Rachael Ward, Dr. Chip Eddy, Dr. Y.L.Tian, Dr. David Meyer, Dr. Konrad Bussmann, Dr. Nadeem Mahadik, Dr. Luke Nyakiti, Dr. Neeraj Nepal, Dr. Glenn Jernigan, Dr. Doe Park and David Zapotok for their encouragement and help at different stages of my career. I am thankful to Dr. Anthony Boyd and Dr. Virginia Anderson for putting up with me at the same office, which I am sure was not easy.

And last but not the least, I would like to express my gratitude to my family, specially to my sister Amrita Nath and my cousin Anushirsa Nath, whose continuous love, sacrifice, support and encouragement have allowed me to pursue my ambitions. I am thankful to my friends Dr. Sohan Seth, Arindam Majumder, Tuhin Mohanta and Arpita Mukherjee for their never-ending support and faith in my success.

TABLE OF CONTENTS

LIST OF TABLES

LIST OF FIGURES

LIST OF ABBREVIATIONS

AFM ..... atomic force microscopy
BOE ..... buffered oxide etch
CVD ..... chemical vapor deposition
DI ..... deionized
EBSD ..... electron backscatter diffraction
FET ..... field effect transistor
GaN ..... Gallium Nitride
MBE ..... molecular beam epitaxy
RIE ..... reactive ion etch
Rpm ..... revolutions per minute
RTA ..... rapid thermal anneal
sccm ..... standard cubic centimeter per minute
SEM ..... scanning electron microscope
TEM ..... transmission electron microscopy
UV ..... Ultra violet
XRD ..... X-ray diffraction

ABSTRACT

TRANSPORT PROPERTIES OF 3D AND 2D DISORDERED ELECTRONIC MATERIALS

Anindya Nath, Ph.D.

George Mason University, 2014

Dissertation Director: Dr. Mulpuri V. Rao

In the real world, the crystalline states are exceptions rather than the rule. Disorder exists in varying forms and degrees, ranging from a few impurities or voids in otherwise perfect crystals to the strongly disordered amorphous materials and alloys. Due to the lack of periodicity and translational symmetry of disordered materials, one might expect that the universal features of crystalline materials would disappear as well. Yet the possibility of corresponding universal features in the electronic structure of disordered materials which are different from perfect crystals, made the study of the disordered material is one of the most intriguing topics in solid-state physics. This doctoral dissertation addresses application oriented challenges and some of the related basic science questions about transport properties of two such disordered materials of different dimensionality. Ion-implanted Silicon Carbide (SiC) near degeneracy is studied as an example of a three dimensional (3D) disordered material. Epitaxial gaphene grown

on SiC and systematically damaged by the introduction of low temperature plasma is studied an example of two dimensional (2D) disordered material.

Chapter One: Introduction

From the emergence of quantum mechanics, crystalline materials have been studied intensively. In a perfect crystal, the atoms are arranged periodically in space which establishes long-range translational order that leads to several universal features in the electronic structure. The most significant outcome of the fact that the electronic wavefunction can be modeled as plane waves modulated by the lattice periodicity which results in energy bands separated by gaps and crystal momentum description by quantum number. These universal features are the building blocks of Bloch's theory of electron state in a periodic lattice which enables the band structure calculations of rather complicated crystalline materials.

The basic theory of perfect crystals with non-interacting particles can explain few observable properties of solids. Moreover when accompanied with a many-body kinetic theory it provides the conceptual foundations for most of solid-state physics. Unfortunately, in the real world, the crystalline states are the exceptions rather than the rule. Disorder exists in varying degree, ranging from a few impurities or voids in an otherwise perfect crystals to the strongly disordered amorphous structures. Due to the lack of periodicity and translational symmetry of such materials one might expect that the universal features of crystalline materials would disappear as well. Yet the possibility of corresponding universal features in the electronic structure of disordered materials which

are different from perfect crystals make the study of disordered material one of the most intriguing topics in solid-state physics. In the next section we will briefly describe the theoretical and application oriented interests in disordered materials.

1.1 Motivation

Disorders and defects of various degrees are introduced intentionally or un-intentionally in all practical electronic systems. Defects like stacking faults, basal plane and threading screw/edge dislocations, interstitials, vacancies, grain-boundaries etc. can be introduce during crystal growth, doping, annealing, device fabrication or even by end-users during device operation. Moreover in extrinsic semiconductors, the impurity ions occupy random positions in lattice which break the crystalline order and symmetry. When such impurity concentration is small, the quasi-particles exhibit a thermally activated charge transfer. However, above a critical level, the carriers behave like a degenerate electron gas and charge transfer becomes temperature independent. Hence, the theoretical interest of studying disorder systems is two-fold. First it provides the opportunity of studying metallic to non-metallic conduction and vice versa, known as metal to insulator transition (MIT). The second point of interest is understanding the concept of mobility in such disordered systems. Such studies are expected to strengthen the current physical, mathematical and simulation models and will lead to better performing devices with higher yields. Moreover, another huge advantages of amorphous electronic materials is the ability to be prepared in large areas in a cost-effective way for what may be coined ‘macroelectronics’, such as displays, scanners,

solar cells, image sensors, position sensors, and similar applications. Admittedly, due to the existence of charge scattering, grain boundary and multiple trapping in shallow localized states, such disordered systems have low carrier drift mobilities compared to their crystalline counterparts and limit the use of these materials in high-speed or high-gain applications. Yet for several low-speed electronics such as flat panel displays, xerography (photocopying and printing) photoconductors, high-gain avalanche rushing photoconductor (HARP) etc. where drift mobility is not the crucial parameter, disordered systems are drawing huge attention. In the next section, the basic concepts of transport properties of such disordered systems are briefly discussed.

1.2 Weak scattering theory

As stated earlier in ideal crystalline semiconductors, the standard theory of electron transport phenomena is based on Bloch waves which determines single-electron eigenstates. An immediate outcome of such approach is the description of quasi-continuous energy bands separated by bandgaps. However, a finite concentration of randomly distributed impurities of equal potential (positional disorder) or substitutional disorders modifies the electron wavefunctions and the density of state (DOS) of the system.

The wavefunction of a perfect periodic potential can be described as

$$\Psi(r) = A(r)\mathrm{e}^{i\Phi(r)}$$

where the amplitude A(r) is a periodic function of r and the phase φ(r) is given by

$$\varphi(r)=k\cdot r.$$

The presence of weak disorders usually only create phase incoherence and the electronic states in such systems can be described by almost free quasi-particles modified by the interaction with the random potentials (related to static deviations of the potential in the crystal from periodicity or lattice vibrations) and by the electron– electron interaction. The wavefunctions remain extended over the entire sample and transport is described using the Boltzmann equation which leads to the following expression:

$$\sigma = \frac{ne^2}{m}\tau \text{ provided } \lambda << l$$

Where σ is the conductivity, n is the concentration, m is the effective mass, τ is the momentum relaxation time, λ is the de Broglie wavelength and $l = v\tau$ (v=characteristic velocity) is the mean-free path of the quasi-particles.

1.3 Localization, mobility edge and metal to insulator transition

In disordered systems (e.g. amorphous solids and liquids, degenerately doped semiconductors etc.), mesoscopic order exists and the electron energy spectrum preserves the characteristic features of the band structure. However, increasing disorder not only affects the phase but the amplitude as well and the wavefunction exhibits strong special amplitude fluctuation. For sufficiently strong disorder it is possible to have $A(r) \rightarrow 0$ for $r \rightarrow \infty$ (usually exponentially), also known as localization of extended states (Anderson localization) [1][2].

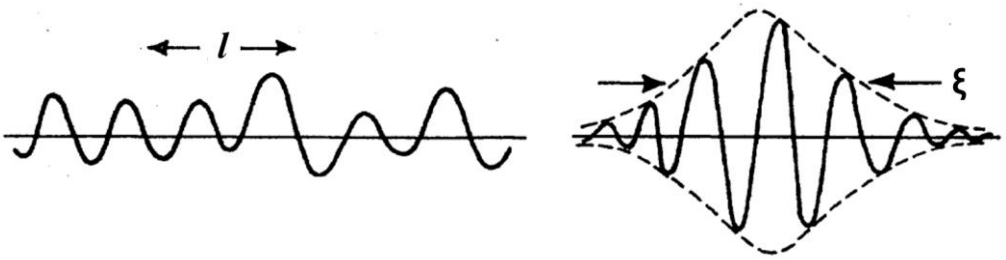

Figure 1.1: Typical wave functions of (a) extended state with mean free path (b) localized state with localization length ξ [2]

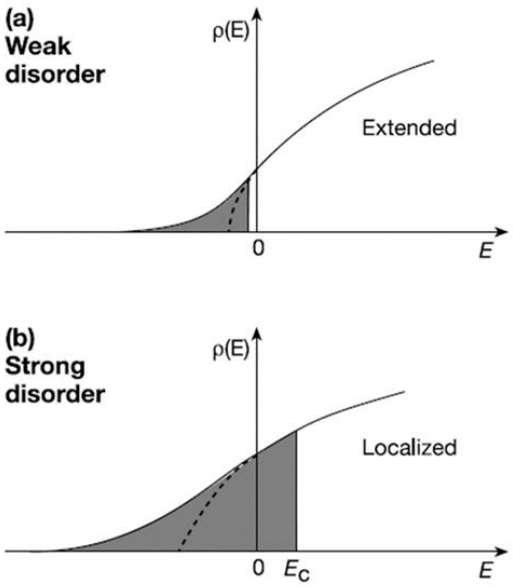

Figure 1.2: (*a*) One-electron DOS in a random potential for weak disorder. (*b*) As the disorder is increased, the mobility edge (E_C) eventually moves into the positive-energy regime.

However, states with different energies are affected differently by such disorders and the coexistence of localized and extended states in the same system is possible [3][4]. As an example, for intermediate disordered systems, the states in the middle of the band may remain extended whereas states near the band edges may be localized (Fig 1.2). The critical energy that separates the extended and localized states is called the mobility edge [5]. If the Fermi energy (ε_F) is above the mobility edge, the system exhibits a finite conductance even at 0 K (metallic state), whereas a vanishing conductivity is obtained if the ε_F lies below the mobility edge (insulator). Hence the mobility edge defines the *metal-insulator transition* (MIT) in a disordered system. However, it should be noted that there is no singularity in the DOS at the mobility edge.

For strong structural disorders such as degenerately doped semiconductors, the electronic states are different from Bloch states and the conventional Boltzmann theory is not expected to be relevant. Surprisingly, the weak-scattering theory can be applied to describe carrier transport in such systems if the Fermi level lies in the extended states and is not very close to the mobility edge.

However, such applicability is only valid if the condition for applicability of this theory is $na_B^3 \gg 1$ where n is the carrier concentration (~ doping impurity concentration) and a_B is the Bohr radius. If the impurity concentration is not too high and the average distance between the impurities is much greater than the lattice period, the Bloch electrons will be scattered by screened atomic impurity potential with random special distribution. Due to screening, such scattering is considered as weak and the Born

approximation of weak-scattering theory can be applied to obtain qualitative agreement with experimental results [4].

1.4 Temperature dependence

Inelastic phonon scattering is the predominant mechanism that gives resistivity a positive temperature coefficient as the number of phonons increases with increasing temperature. At high temperatures, the phonon population is proportional to $\frac{KT}{\hbar\omega}$ (where ω is the phonon frequency and K is the Boltzmann constant) and $\sigma \sim T^{-1}$, whereas at low temperature conductivity dependence is stronger: $\sigma \sim T^{-5}$ (Bloch–Grüneisen).

In the low-temperature regime, charge carrier scattering is dominated by elastic impurity scattering. The conductivity is almost independent of temperature or ionized impurities and the dependence is $\sigma \sim T^{3/2}$ and remains finite at T=0.

Static disorder (impurities and defects) scattering may also dictates an auxiliary temperature dependence of the conductivity which is related mainly to the screening effects. At higher temperature screening becomes weaker leading to a positive temperature coefficient of the resistivity.

In a degenerate electron gas, another source of inelastic scattering is through electron–electron interaction mechanism. The probability of such scattering is proportional to T^2 as only the electrons within the energy distribution of KT near the Fermi level can be scattered.

1.5 Weak localization

In the low temperature regime, the temperature dependence of the classical conductivity described by the Boltzmann theory becomes less significant and the quantum interference of scattered electron waves becomes important. The quantum corrections to the Drude conductivity can be understood by the interference of the electron wavefunctions which favors backscattering. In this regime, localization length exceeds all other relevant lengths in the system and is called weak localization (WL). The temperature dependent correction to the conductivity for 2-dimensional (2D) and 3-dimensional crystals (3D) can be given as:

$$\Delta\sigma_{3D}(T) = -\left(\frac{e^2}{\pi^3\hbar}\right)\left(\frac{1}{l} - \frac{1}{a}T^{\frac{p}{2}}\right)$$

$$\Delta\sigma_{2D}(T) = -\left(\frac{pe^2}{2\pi^2\hbar}\right) ln\left(\frac{T}{T_0}\right)$$

where p is an index depending on the scattering mechanism, l is the elastic mean free path and $T_o = (a/l)^{2/p}$

Hence at low temperature, where the Drude conductivity is temperature independent, such correction due to WL yields non-trivial modifications and the conductivity decreases with decreasing temperature. However, several phase-breaking mechanisms such as effect of a magnetic field, magnetic impurity and spin-orbit scattering destroys the time reversal symmetry and mitigates the effect of weak-localization. Moreover, it should be noted that low mobility samples and low

temperature are required to observe such weak-localized corrections as under such condition the phase-breaking path is much larger than the elastic mean free path.

1.6 Interaction effect:

The Fermi-liquid theory is not applicable for nonideal "dirty" metals as the interaction effects are substantially different from the case of almost free electrons. If the elastic momentum relaxation time (τ) is smaller than the characteristic time ($\hbar$/KT), the quasi-particle interaction is in the "diffusive regime" (i.e. two interacting particles diffuse coherently before exchanging an energy of about KT) and yields similar correction to conductivity both in three and two dimension. However, unlike weak-localization, such enhanced electron-electron interaction is not suppressed by magnetic field. Another distinguishing factor between these two effects is, unlike WL, the Hall coefficient (R_H) is altered due to e-e interaction.

1.7 Hopping transport in disordered system

In disordered systems at high enough temperature, the electron transport through extended states dominates as a significant fraction of charge carriers resides in these states. However, as temperature decreases the concentration of such carriers decrease exponentially and carrier transport through tunneling between localized states dictates the conductivity. Such phonon-assisted transport phenomena is called hopping conduction.

At low temperature the hopping probability between the states will be proportional to the overlap integral of the two wavefunctions which depends exponentially on their spatial distance, and a Boltzmann factor containing their mean energetical distance. Depending on the temperature and the energy spread of the localized states involved into the charge transport process nearest neighbor hopping (NNH) or variable range hopping (VRH) dominates. At relatively high temperature, if the thermal energy KT is higher than the energy separation between the spatially nearest-neighboring sites, hopping through nearest neighbor dictates the conduction. However, if such sites have very different energies, the Boltzmann factor will decrease the probability of carrier transition between these sites. In such conditions it would be more favorable for the carriers to hop to a distant site provided the mean energy separation is less than that to the nearest neighbor. Hence with decreasing temperature the typical length of carrier transition increases in a disordered system and such regime is called VRH. For a *d* dimensional system, the temperature-dependent conductivity in the VRH regime can be expressed by: $\sigma \sim T^{(d+1)}$.

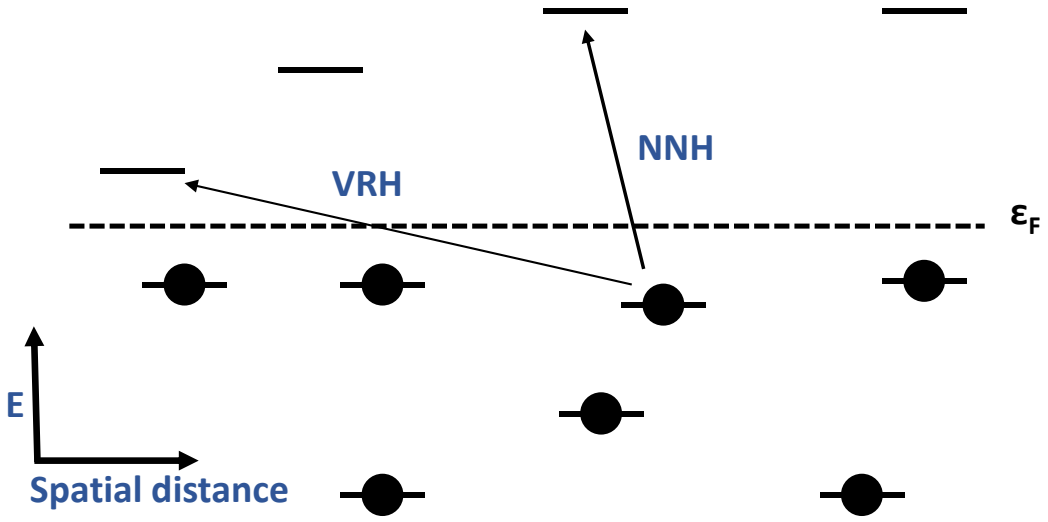

Figure 1.3: Nearest Neighbor and Variable range hopping

1.8 Scaling theory

The conceptual framework of the early formulation of scaling theory envisioned constructing a sample of size $(2L)^d$ in d dimensions by putting together squares or cubes of size L^d . One would expect that the nature of the eigenstates of the $(2L)^d$ system can be predicted by the nature of the states of the L^d system. However, the more intriguing question is, if the systems can be described by only one or few parameters close to the transition between localized and extended states. Since the dc conductivity vanishes at T=0K in the localized states, it cannot be employed to describe transport in finite systems. Hence, an alternative description of conductance was introduced for 1D disordered system in terms of their transmission properties which gives explicitly the

scaling properties of the conductance as a function of the length of the system[2][6]. This approach (introduced by Landauer) can be considered as the precursors of the one-dimensional scaling theory. For arbitrary dimensions, to describe the conductance of L^d hypercube system, the logarithmic derivative of the conductance was introduced:

$$\beta = \frac{dlng}{dlnL}$$

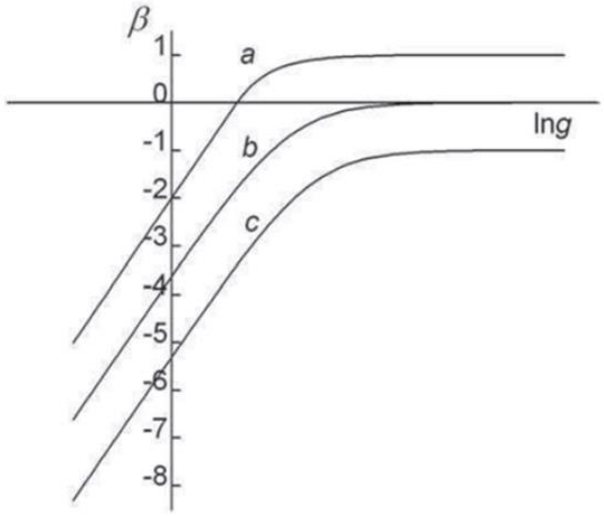

Figure 1.4: The shape of the scaling function *β(g)* for systems of different dimensionalities: (*a*) *d* = 3; (*b*) *d* = 2; (*c*) *d* = 1 [4]

It was assumed that the term β depends only on the conductance and not on disorder, energy or L separately. Assuming $\beta(g)$ is a continuous and monotonically increasing

function, the qualitative behavior of $\beta(g)$ was obtained by interpolating from the asymptotic behavior of large and small conductance. If $\beta > 0$, the conductance increases with the size of the sample (metallic behavior). The metallic regime can be described by classical behavior ($\beta(g) = d - 2$) and is obtained from the classical relation between the conductance and the conductivity. When the random potential is small (i.e less disorder), for a large piece of metal (L>> *mean free path, l*) the $g(L) = \sigma L^{d-2}$ (Ohm's law). However, if the states near Fermi energy are localized, the relevant length scale is the localization length ξ, and for a large system (L>> ξ), $\beta(g) = lng$ and $g(L)\alpha e^{-L/\xi}$, which is clearly a non-Ohmic scale dependence. Moreover, a fixed point where $\beta(g_c)$=0, corresponds to a disorder-induced MIT. One of the key features of one dimensional scaling theory is that such MIT can exist only in three dimensional systems where β can be both positive and negative (see Fig. 1.4. However, for two and one dimensional cases the insulating regime always exists in the thermodynamic limit at T=0 K for non-interacting electrons and in the absence of magnetic scattering effects.

1.9 The critical behavior:

A further development of the one-parameter scaling theory concerns the critical behavior at the MIT (for an Anderson transition) and the DC conductivity (σ_{dc}) and localization length(ξ) near the mobility edge are expected to behave according to

$\sigma_{dc}\ \alpha\ (E-E_c)^s$ and $\xi\ \alpha\ (E_c-E)^{-\nu}$ and $s=\nu$ can be calculated from the scaling relations. Experiments yielded $s=\nu=1/2$ (for P doped Si) and $s=\nu=1$ (for $Al_xGa_{1-x}As$). It is believed

that the exponent ½ is due to the presence of local magnetic moments by Columbic interaction whereas the exponent 1 is ascribed to an Anderson transition.

1.10 Minimum metallic conductivity

Ioffe and Regel argued [4] that in order to apply the weak-scattering theory, the electron wavelength (λ) must be shorter than the mean-free path (*l*) and both should exceed the interatomic spacing a. However, at T=0, for a degenerate electron gas the de Broglie's wavelength λ increases as the system energy approaches the mobility edge and eventually becomes comparable to *l*. Extending the weak-scattering theory near mobility edge, Mott has concluded that the minimum metallic conductivity,

$$\sigma_{\min\_3d} = \frac{e^2}{3\pi^2\hbar l} \text{ for 3D and}$$

$$\sigma_{\min\_2d} = C\frac{e^2}{\hbar} \text{ for 2D}$$

where C =0.1 [3], this is a universal behavior (no length scale)

According to Mott as the conductivity at T=0 cannot be lower than these values, once the Fermi energy crosses the mobility edge, the conductivity goes to zero, which means the metal to insulator transition is discontinuous. However, Mott's argument contradicts one-parameter scaling theory of localization both in three and two dimension as the scaling theory [7] expects continuous metal-insulator transition in 3D and two dimension scaling theory doesn't predict the existence of mobility edge.

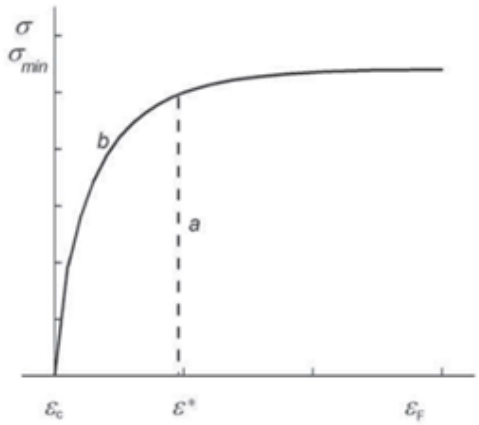

Figure 1.5: Behavior of the conductivity at $T = 0$ K near the mobility edge ε_c (schematic). (*a*) Discontinuous transition implied by Mott's concept of the minimum metallic conductivity; (*b*) continuous variation predicted by the scaling theory of localization; the critical region corresponds to the energies $\varepsilon_c < \varepsilon < \varepsilon^*$, where the boundary of the critical region ε^* is the energy at which $\sigma(\varepsilon^*) = \sigma_{min}$ [4]

1.11 Temperature dependence near metal-insulator transition:

The extrapolation of the finite temperature conductivity to T=0K is required to compare between theoretical predictions and experimental results at zero-temperature. To accomplish that, the temperature dependence conductivity at low temperature can be written as: $\sigma(T)=\sigma_0-AT^s$, where σ_0 is the residual conductivity due to impurity scattering and s is the temperature coefficient.

For classical metals with weak disorders, Boltzmann equations can be used and both A and s are positive ($s \geq 2$, for e-e scattering s=2). However, with increasing disorder, conductivity decreases at zero-temperature and the temperature coefficient of the metallic conductivity is expected to change its sign at the boundary of classical to critical region. Depending on the degree of quantum correction, system energy and dimensionality the temperature dependence forms may take the form: $\sigma(T)=a_1-b_1T^{1/2}$ or $\sigma(T)=a_2-b_2T^{1/3}$.

1.12 Accomplishments

This doctoral dissertation addresses application-oriented challenges and some of the related basic science questions about transport properties of two disordered materials having different dimensionality. Phosphorus and aluminum ion-implanted 4H-Silicon Carbide (SiC) near degeneracy is studied as an example of a three dimensional (3D) disordered material. The p-type resistivity bottleneck which impedes the full potential of SiC based bipolar devices is addressed. The obtained n type (70 Ω/ □) and p type (550 Ω/ □) sheet resistances are among the lowest reported values in the literature. Moreover strategies to reduce surface roughness introduced during high temperature post-implantation anneal is discussed. A metal to insulator (MIT) transition was observed when SiC was implanted by phosphorus near its solubility limit. For aluminum implanted SiC samples, semiconductor behavior was preserved where intra-band conduction and conduction via nearest neighbor hopping were observed.

Epitaxial gaphene grown on SiC is studied as an example of two dimensional (2D) disordered materials. This work focuses on obtaining a clean graphene surface after standard device fabrication and understanding and controlling the graphene-metal interaction which is governed by both intrinsic and extrinsic factors. It is demonstrated that the contact resistance is primarily limited by graphene-metal vertical carrier transmission, and intentional edge-contact is necessary to achieve a contact resistance limited only by intrinsic quantum resistance. Contact resistance (140 $\Omega \cdot \mu m$) near the quantum resistance limit was obtained by employing edge-contact and a polymer assister conventional lithography technique. Moreover, systematic damaging of graphene via the introduction of chemical moieties revealed the existence of a two dimensional MIT in epitaxial graphene, where the strongly localized state is separated from the metallic state by a weakly localized phase with conductivity as a logarithmic function of temperature ($\sigma \sim \log T$). Magneto-transport and Hall measurements show that both weak localization (WL) and enhanced electron-electron interaction effect contribute to the observed behavior, with the WL effects dominating as the system approaches the strongly localized phase.

1.12 Organization of the dissertation

The dissertation is presented in seven major chapters.

Chapter 1 (this chapter): Introduction Chapter gives a brief introduction to the reader about the motivation and the different transport properties of disordered materials of different dimensionality.

Chapter 2: Describes Phosphorus implantation of SiC near its solubility limit. Strategies to maintain a low surface roughness during high temperature post-implantation annealing is addressed. Implantation induced lattice damage recovery is discussed. Detailed electrical characterization is presented to discuss sheet resistance, mobility model, dopant activation and metal to insulator transition (MIT).

Chapter 3 and 4: Describes Aluminum implantation of SiC near its solubility limit. The p-type resistivity bottleneck of SiC is addressed. Furthermore, this chapter describes low temperature transport properties of Aluminum implanted SiC near degeneracy. Conduction through an impurity band (IB) and nearest neighbor hopping is analyzed. Also the Hall scattering factor paradox is discussed.

Chapter 5 and 6: These chapters analyze the importance of lattice disorder in graphene at the graphene-metal interface to obtain contact resistance limited only by intrinsic quantum resistance. The major limiting factors contributing to high and inconsistent contact resistance reported in literature are discussed. Moreover, strategies to obtain a clean graphene surface after standard device fabrication is described and temperature dependence of graphene-metal contact resistance is analyzed using Landauer-Büttiker model.

Chapter 7: Describes two dimensional (2D) metal to insulator transition in epitaxial graphene synthesized on SiC via controlled exposure to low temperature fluorine, nitrogen and oxygen plasmas.

Chapter Two: Phosphorus Implanted 4H-SiC Near Solubility Limit

Motivation and background

Silicon Carbide (SiC) has gained its popularity in the last two decades for its favorable properties for high temperature and high power applications. The 4H polytype of SiC is widely considered due to its higher and somewhat anisotropic electron mobility with respect to other SiC polytypes [8], [9]. Ion-implantation is the only feasible planar selective area doping technique available for SiC due to the low diffusion coefficient of most of the doping species in SiC. A good surface morphology, a low lattice defect concentration, and a high electrical activation in the implanted layers are required to achieve optimum device performance. A cap film on the implanted SiC wafer during the very high temperature post implant annealing helps to preserve the surface morphology [10]and a very high annealing ramping rate provides favorable electrical properties to the implanted SiC [11], [12]. Radio-frequency (inductively) heated furnaces and microwave heating systems are rapid heating systems. It is well known that doped SiC is an excellent absorber of microwaves due to its high complex dielectric constant. Microwaves (~ 1 GHz) from a source can be amplified and directly coupled to a SiC sample to be annealed through a microwave heating head [13]. Since the sample is placed in microwave transparent surroundings, the microwaves are absorbed by the SiC sample only, leading to extremely high heating and cooling rates. This feature contrasts microwave annealing

with resistive and inductive heating furnaces, where the heating source not only heats the sample but also the surrounding ambient. Hence, microwave heating provides ultra-fast ramp rates and very-high annealing temperatures (up to 2100°C) which are optimum conditions for annealing ion-implanted 4H-SiC. Moreover, improved electrical activation and lattice recovery after microwave annealing of ion-implanted SiC has already been shown [14][15].

Phosphorus (P) is the preferred donor (n-type) impurity in SiC at elevated doping concentrations because of a higher electrical activation with respect to Nitrogen (N) [16]–[18]. In 4H-SiC for an implanted P^+ concentration up to 10^{20} cm^{-3} an almost complete electrical activation [18] and an implanted layer resistivity as low as $2 - 3 \times 10^{-3}$ Ωcm at room temperature (RT) has been reported for conventional annealing at 1700° C [17], [18]. At such elevated P concentration, the onset of an impurity band conduction has been observed, however the P substitutional fraction from experimental Hall data was not obtained [18]. But the reduction of the electrical activation for increasing P concentration above 3×10^{20} cm^{-3} and the asymptotic trend of the implanted layer resistivity towards 10^{-3} Ωcm [10] may indicate that a phenomenon limiting the electrical activation of the implanted P^+ ions occurs for high P concentrations in 4H-SiC.

In most of the studies, the maximum annealing temperatures of P^+ implanted 4H-SiC have been limited to 1700°C for conventional heating [10], [17]–[19] and 1950°C for the ultra-fast microwave heating [14], [20] to avoid SiC material loss from the implanted SiC surface [17], [18], [20]. The use of a protective C-cap would have permitted much higher annealing temperatures by avoiding Si sublimation, though

typically it has been restricted to 1700°C even with C-cap [10], [15]. This may be due to the fact that different authors [10], [17], [18], [20] had measured an asymptotic trend for the sheet resistance of P^+ implanted 4H-SiC layers for increasing annealing temperature and annealing time above 1600°C and a few minutes, respectively. A very high doping concentrations and low defect densities are required to minimize device parasitic resistances and device reverse leakage currents, respectively. These attributes lead to low power dissipation and fast switching time.

This work is aimed at determining the conditions to obtain minimum possible *n*-type resistivity and to study a possible metal to insulator transition (MIT) in phosphorus implanted 4H-SiC near its solubility limit. The implanted dopant concentration and post implantation annealing temperatures employed in this study are in the ranges 5×10^{19} – 8×10^{20} cm^{-3} and 1700 - 2050°C, respectively. Both a conventional radio frequency heated furnace and a microwave heating system [21] were used for the annealing process.

2.1 Experimental

2.1.1 Ion-implantation

Large pieces of high purity <0001> 8° off-axis semi-insulating 4H-SiC wafers purchased from CREE Research Inc. were implanted at 500°C with P^+ ions for obtaining almost flat profiles over a depth of about 150 nm next to the wafer surface. The implant schedules were computed by Pearson IV simulation [22]. Ion energy values and ion doses were varied to obtain plateau heights of 5×10^{19}, 1×10^{20}, 4×10^{20}, and 8×10^{20} cm^{-3} that correspond to integral doses of 7.37×10^{14}, 1.92×10^{15}, 7.68×10^{15}, and 1.54×10^{16} cm^{-2},

respectively. Table 2.1 provides the corresponding implantation schedules. The as implanted P^+ depth profiles of few samples were measured by Secondary Ion Mass Spectrometry (SIMS). A Cameca IMS-4f spectrometer was used with 14.5 KeV Cs^+ primary ion beam. The integral of each SIMS spectrum was set equal to the corresponding P^+ ion dose and the obtained depth profile was compared with the computed Pearson IV profile as shown in Fig. 2.1 for the 7.37×10^{14} and 1.92×10^{15} cm^{-2} doses. The computed and measured P depth profiles are in good agreement for plateau heights, plateau thicknesses and profile tails towards the substrate except for a deep P tail above the SIMS detection limit for the sample that has been implanted at the higher dose. In this study the full width at half-maximum (FWHM) values of the Pearson IV profiles is considered as implanted layer thickness values for the analysis of the electrical data.

Table 2.1 Implant schedules obtained by Pearson IV simulations with semi-empirical coefficients from ref. 19 for P^+ ions in crystalline SiC

	P plateau value (cm^{-3})			
Energy (keV)	**5×10^{19}**	**1×10^{20}**	**4×10^{20}**	**8×10^{20}**
	P dose per single energy value (cm^{-2})			
20	2.03×10^{13}	0	0	0
30	8.13×10^{13}	1.63×10^{14}	6.50×10^{14}	1.30×10^{15}
50	9.65×10^{13}	1.93×10^{14}	7.72×10^{14}	1.54×10^{15}
70	1.02×10^{14}	2.03×10^{14}	8.13×10^{14}	1.63×10^{15}
100	1.93×10^{14}	3.86×10^{14}	1.54×10^{15}	3.09×10^{15}
150	2.44×10^{14}	4.88×10^{14}	1.95×10^{15}	3.90×10^{15}
170	0	4.88×10^{14}	1.95×10^{15}	3.90×10^{15}
	Total dose per sample (cm^{-2})			
	7.37×10^{14}	1.92×10^{15}	7.68×10^{15}	1.54×10^{16}

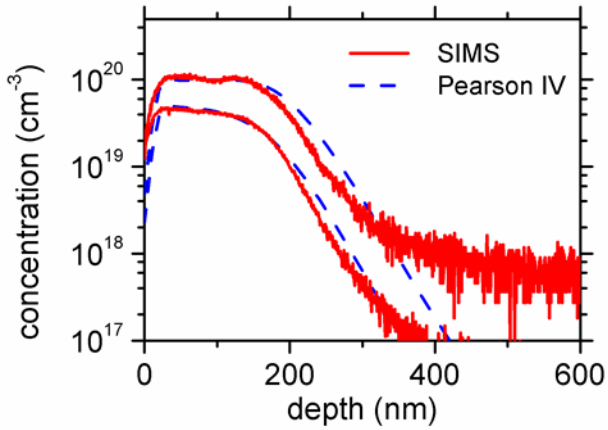

Figure 2.1: Simulated (pearson IV) and measured (SIMS) as implanted P^+ ion depth profiles in 4H-SiC for the implantation schedules of Table 2.1 corresponding to the 5×10^{19} and 1×10^{20} cm^{-3} plateau values.

2.1.2 Graphite-cap formation, annealing and vdP device fabrication

The implanted 4H-SiC surfaces were covered by a spin coated photo-resist film and annealed at 900°C for 2 min in forming gas (90% N_2 and 10% H_2) with a temperature ramp-up $\geq$ 110°C/s. During this annealing the photo-resist pyrolyzes and transforms into an amorphous carbon based material that is rich in graphite nanoflakes [23]. These samples were cut into 5 mm × 5 mm samples and subsequently were annealed in an inductively heated furnace (RFA samples) or in a prototype microwave annealing system(MWA samples) [21]. In the RFA specimens, the annealing time has been fixed to

5 min while annealing temperature has ranged between 1700°C and 1950°C. In MWA samples, the annealing duration has been fixed to 30 s while the annealing temperature has ranged between 1950°C and 2050°C. The temperature ramp-ups that have been used in this study are at least one order of magnitude higher than the maximum rump-up rates of commercial furnaces for SiC post implantation annealing.

After post implantation annealing, C-cap forms an ohmic contact layer on the Phosphorus implanted 4H-SiC surface [23] and can be exploited for the fabrication of ohmic pads on the four corners of the square $5\,\text{mm} \times 5\,\text{mm}$ 4H-SiC samples by a selective Reactive Ion Etching (RIE) in an O_2 assisted plasma, to transform the samples into Van der Pauw (VdP) devices. The C-cap was completely removed by a 800°C treatment in an O_2 ambient for 10 min. On these samples ohmic contacts for VdP devices were fabricated by ultrasonically bonding several 10 μm Al(1%Si) wires directly on the four corners of the square SiC specimens. These unconventional methods for the fabrication of ohmic contacts have been important simplifications of the sample processing while fulfilling the need to have thermally stable ohmic contacts for electrical characterizations at elevated temperatures up to 450°C.

Square four-point sheet resistance and Hall effect measurements in the temperature range RT – 450°C have been performed on VdP devices with samples placed in a low vacuum ambient. A magnetic field of 1 T parallel to the <0001> axis and currents in the range 1×10^{-6} A – 5×10^{-3} A along a direction orthogonal to the <0001> axis have been used for these measurements. In this current range sheet resistance and Hall coefficient values remain constant. Taking into account the extension of the contact

pads with respect to the sample size the measured bias values have been corrected as suggested in ref. [24]. The Hall factor for electrons in 4H-SiC has been assumed equal to 1 over the entire temperature range of measurements [25]. Carrier mobility has been obtained as the ratio of the sheet resistance to the Hall coefficient. Assuming an implanted layer thickness equal to the FWHM of the simulated Pearson IV profiles, sheet resistance and sheet carrier concentration have been converted into resistivity and volume carrier concentration, respectively.

2.1.3 Surface morphology and structural characterization

The surface morphology of the as implanted and of the post implantation annealed samples, with C-cap and after C-cap etching, has been characterized by Atomic Force Microscopy (AFM) in the tapping mode. The Root Mean Square (RMS) roughness over an area of $4\ \mu m \times 4\ \mu m$ or $5\ \mu m \times 5\ \mu m$ has been taken as a metric for surface morphology of the samples.

High-resolution X-ray diffraction scans were obtained with a Rigaku ATX-E 4-circle diffractometer system using a truly monochromatic Cu $K\alpha 1$ radiation from a rotating-anode X-ray generator, operated at 50 kV and 200 mA. Monochromaticity of the X-ray beam is measured by the ratio $\Delta\lambda/\lambda$. Here λ is the wavelength, $\Delta\lambda$ is the FWHM of the incident X-ray wave. The diffractometer employed here has $\Delta\lambda/\lambda \approx 5\times10^{-4}$. The angular resolution was $\Delta(2\theta) = 0.001°$. Since the SiC (0001) was a miss-cut crystal by nearly 8°, the appropriate diffraction condition for SiC(0004) was obtained by searching

ω, ϕ and χ for optimum intensity. The rocking curves were measured using a step size of 0.0005° inω. The penetration depth in 4H-SiC of X-rays used in this study is ≈ 3μm.

2.2 Results and discussion

2.2.1 Surface morphology

The surface morphology of different regions of the same RFA 1×10^{20} cm^{-3} P^+ Another Subsection implanted 4H-SiC sample has been depicted in Fig. 2.2. The RMS roughness after 1950°C, 5 min annealing without C-cap, with C-cap and after C-cap etching are (5.4 ± 0.1), (1.4 ± 0.2) and (0.28 ± 0.02) nm, respectively. The RMS roughness of a virgin 4H-SiC surface (not shown in Fig. 2.2) is (0.089 ± 0.009) nm. Fig. 2.3 represents the RMS surface roughness of C-cap films and of underlying SiC surface (measured after cap removal) versus post implantation annealing temperature for samples that have been implanted with different P^+ doses. No dependence of the RMS roughness on the P^+ ion dose has been observed in this study. Though an increase in the RMS surface roughness for both the C-cap and the underlying SiC with increasing annealing temperature is evident, the values still remain below 1 nm which is highly compatible with device fabrication. These results show the high quality of the C-cap that has been used in this study which can withstand annealing temperatures up to 2050°C during microwave annealing. Moreover, the smoothness of the annealed C-cap film itself is of the order of 1 nm suggesting that such a film could be integrated in a planar device fabrication processing for ohmic contacts or for conductive stripes.

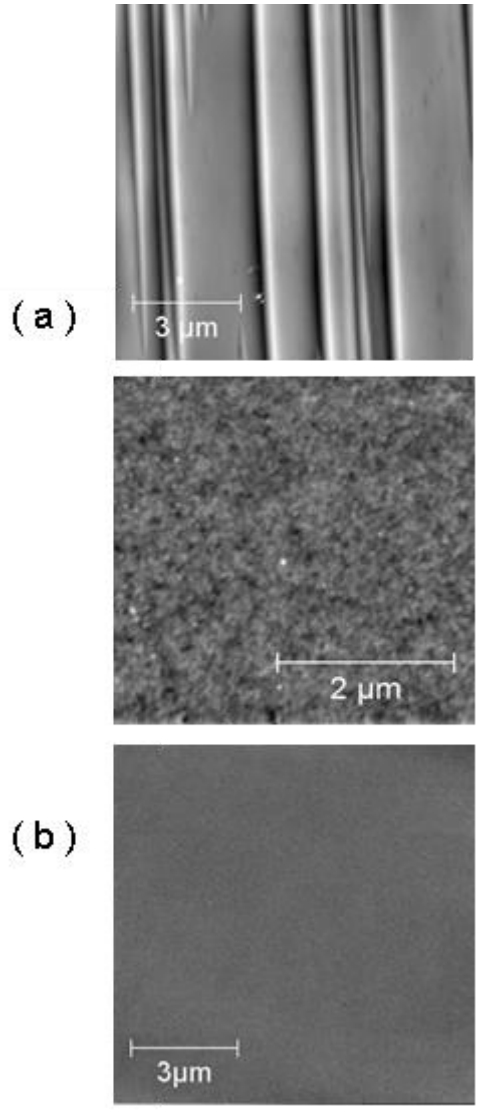

Figure 2.2: AFM images of the same 1×10^{20} cm^{-3} P^{+} implanted 4H-SiC specimen after 1950°C, 5 min RFA: (a) area annealed without C-cap, (b) area with preserved C-cap, (c) area where C-cap has been etched by thermal oxidation

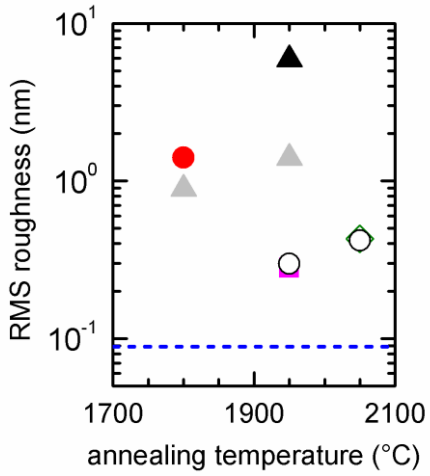

Figure 2.3: RMS surface roughness of RFA (close markers) and MWA(open markers) P^+ implanted 4H-SiC specimens versus post implantation annealing temperature. Results for (▲) C-cap surfaces, 4H-SiC surfaces (△, ○, ■, ●) after C-cap etching, and (▲) after post implantation annealing without C-cap are shown. These values are independent of P^+ dose values that vary in the range 1.92×10^{15} - 1.54×10^{16} cm^{-2}. The (*dashed line*) RMS surface roughness of a virgin 4H-SiC is also plotted for comparison. The data error bars are smaller than the markers dimensions.

2.2.2 Electrical characterization

Figs. 2.4(a-b) reveal that the sheet resistance of P^+ implanted 4H-SiC layers decreases up to a saturation value of about 70 Ω/□ for implanted P^+ plateau values $\geq 4 \times 10^{20}$ cm^{-3} and for post implantation annealing temperatures $\geq$ 2000°C. These results confirm what is expected, i.e. that the sheet resistance of P^+ implanted 4H-SiC layers decreases and saturates for increasing post implantation annealing temperature and P^+ implanted dose [17], [18], [20]. But, in this study saturation takes place at a P^+ dose and at a post

implantation annealing temperature that are higher than those published to date in the literature. Moreover, the saturation sheet resistance value obtained in this study corresponds to an implanted material resistivity of about 1.5×10^{-3} Ωcm which is a factor of two lower than the minimum published value which corresponds to a 1650°C - 1700°C post implantation annealing [17], [18], [20]. The minimum resistivity obtained in this study is consistent with the value published by Negoro et al. [10] for an implanted P^+ concentration of 3×10^{20} cm^{-3} and a post implantation annealing of 1700°C.

Sheet resistance/resistivity, Hall carrier density and Hall mobility of both RFA and MWA specimens show similar trends versus measurement temperature in the range RT – 450 °C as shown in Figs. 2.5(a-c). Independent of the implanted P^+ dose, the sheet resistance increase with increasing sample temperature indicating a conventional metallic behavior. However, with increasing measurement temperature, the electron density tends to saturate towards a value of 1.5×10^{20} cm^{-3} for implanted P^+ plateau values $\geq 4 \times 10^{20}$ cm^{-3} irrespective of the post implantation annealing method. The corresponding electron mobility shows a negative slope with measurement temperature and a shift towards lower values over the whole measurement temperature range for increasing implanted P^+ concentrations. The former is consistent with phenomenon where mobility is governed by phonon scattering [26]. However, here phonon scattering is not the only dominating mechanism as in such a case, at elevated temperatures, one would expect to obtain almost equal mobility values for different dopant concentrations, which is not apparent in this study. The mobility decreases for increasing implanted P^+ concentrations suggesting that an impurity scattering mechanism should be effective at high temperatures as well. But

ionized impurity scattering due to the partial ionization of the electrically activated P atoms cannot be the only dominant scattering because the variation of carrier density with temperature is rather weak as depicted in Fig. 2.5(b). Theoretical studies show that at thermal equilibrium the P atoms that are in substitutional lattice sites in 4H-SiC are also electrically active. For an higher amount of P in the 4H-SiC crystal the formation of phosphorus-vacancy complexes become relevant [27]. The values of the P substitutional concentrations in 4H-SiC range from 6×10^{18} cm^{-3} at 1400°C to 2×10^{20} cm^{-3} at 2200°C [27].

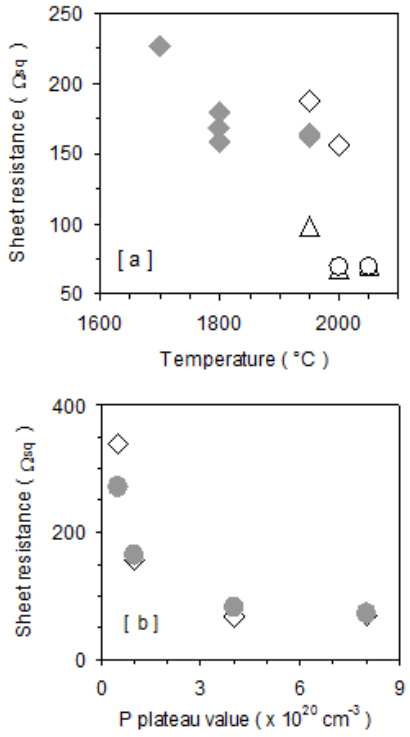

Figure 2.4: The RT sheet resistance of various RFA (close markers) and MWA(open markers) P^+ implanted 4H-SiC specimens versus (a) the post implantation annealing temperature and (b) the implanted P^+ plateau values. In (a) different markers indicate different implanted P^+ plateau values: (◆,◇) 1×10^{20} cm^{-3}, (△) 4×10^{20} cm^{-3}, and (○) 8×10^{20} cm^{-3}. In (b) different markers indicate different post implantation annealing processes: (●) RFA at 1950°C for 5 min and (◇) MWA at 2000°C for 30s. The data error bars have dimensions comparable with those of symbols.

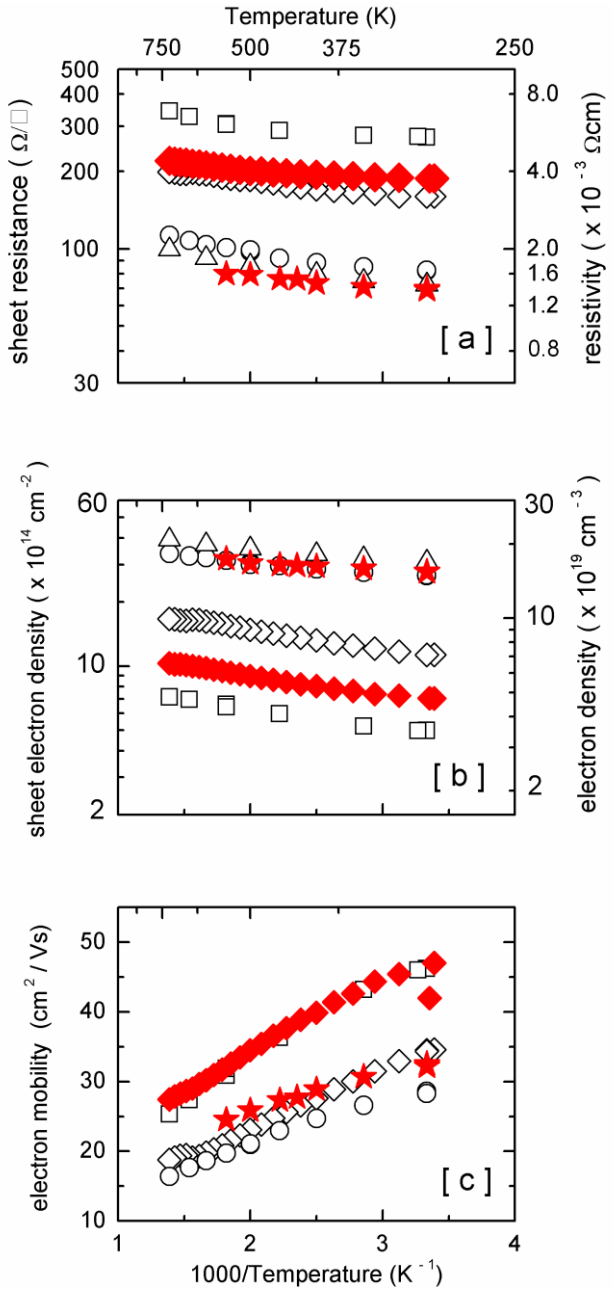

Figure 2.5: (a-c).Electrical characterizations of RFA (open markers) and MWA(close markers) P^+ implanted 4H-SiC layers versus the reciprocal of the temperature of measurement: (a) VdP sheet resistance and resistivity, (b) Hall sheet and volume electron concentrations, and (c) Hall sheet electron mobility. RFA specimens have been implanted with different P^+ concentrations of (□) 5×10^{19} cm^{-3}, (◇) 1×10^{20} cm^{-3}, (○) 4×10^{20} cm^{-3}, and (△) 8×10^{20} cm^{-3} and annealed at 1950°C for 5 min. MWA specimens have been (◆) 1×10^{20} cm^{-3} P^+ implanted and annealed at 1950°C for 30 s, and (★) 8×10^{20} cm^{-3} P^+ implanted and annealed at 2050°C for 30 s. The data error bars have dimensions comparable with those of symbols.

Such theoretical results allow to infer that the maximum carrier density that has been measured in this study is limited by the value of P equilibrium concentration in substitutional lattice positions in 4H-SiC at the temperatures of the post implantation annealing, while carrier mobility is determined by a combined scattering contribution of phonon, ionized impurities and phosphorus-vacancy complexes.

The almost unchanged slope of the electron density versus measurement temperature curves depicted in Fig. 2.5(b) could indicate the activation of an electron transport by impurity band conduction. The absence of an appropriate solution of the charge neutrality equation for degenerated semiconductors prohibits one to infer the P substitutional fraction from the temperature dependence of the electron density curves. An alternate way to appreciate the electrical activation after post implantation annealing is to compute the ratio of the electron density to the implanted P^+ concentration. Fig. 2.6 shows these results at RT and 450°C for MWA and RFA samples that were annealed at the same temperature of 1950°C but different annealing time of 30 s and 5 min, respectively. The RT data for P^+ implanted 4H-SiC from ref. 23 are also shown for comparison. The dashed lines of Fig. 2.6 correspond to a 97% and a 67% ratio between electron concentration and implanted P^+ ion concentration. These lines fit the 450°C and RT data, respectively, when implanted P concentrations are $\leq 1 \times 10^{20}$ cm^{-3} above which a saturation is evident. RFA and MWA data have similar trend, even if absolute values of the latter are lower than those of the former because of the shorter post implantation

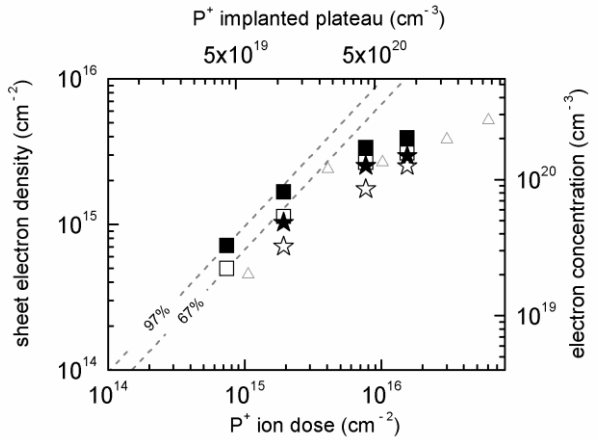

Figure 2:6 Sheet electron density and volume electron density versus P^+ implant dose and implanted P^+ plateau values, respectively, at RT (□, ☆) and at 450°C (■, ★). Samples that have been annealed by RFA at 1950°C for 5 min (□, ■) and by MWA at 1950°C for 30 s (☆,★) are shown. For comparison, RT data for 1700ºC post implantation annealing temperature (△) reported by Negoro et al. [3] are also shown. The data error bars are smaller than the symbol dimensions.

annealing time. Comparing the published results on P^+ implanted and 1700°C annealed 4H-SiC, the RT results of Fig. 6 are similar to those of 600-700°C implanted specimens [17], [20] but are better than those of the 500°C implanted ones [10], [18], [28]. Taking into account that primary ion damage is dependent on the implantation temperature and that the samples were implanted at 500°C, it is inferred that an improvement of the SiC post implantation annealing process is possible by increasing the annealing temperature from 1700°C to 1950-2050°C.

Figs. 2.4(b) and 2.5(a) demonstrate marginally lower saturation sheet resistance for identical P^+ implantation schedule in favor of MWA samples, but, these were annealed at higher temperatures. A lower electrical activation in the MWA sample for

same annealing temperature and same P^+ implantation schedule can be seen in Figs. 2.5(b) and 2.6, but annealing time in MWA was lower than in RFA. These results suggest that the optimum annealing condition for P^+ implanted 4H-SiC can be a temperature as high as 2000°C and a time longer than few minutes.

In Fig. 2.5, the comparison of the carrier density and mobility curves of the 5×10^{19} P^+ cm^{-3}, 1950°C, 5 min RFA specimens with those of the 1×10^{20} P^+ cm^{-3}, 1950°C, 30 s MWA specimen shows equal mobility but a higher carrier density for the MWA sample in spite of the fact that this sample has a higher primary ion damage because of the larger P^+ dose and a shorter annealing time. The comparison of the curves of the 8×10^{20} P^+ cm^{-3}, 1950°C, 5 min RFA sample, with those of the 8×10^{20} P^+ cm^{-3}, 2050°C, 30 s MWA sample shows overlapping carrier densities but higher mobility values for the MWA sample. In this comparison, the primary ion damage is the same but the post implantation annealing temperature is higher in the case of MWA. These results indicate that the electrical transport in the MWA P^+ implanted 4H-SiC layers is better than in the comparable RFA ones.

A further reasonable qualifying test for the electrical performance of the MWA and RFA processed P^+ implanted 4H-SiC is the comparison of the measured electron mobility with that of in-situ doped epitaxial 4H-SiC materials [29], [30]. Such a comparison is shown in Fig. 2.7, where data for P^+ implanted 4H-SiC from ref. 23 are also plotted. As epitaxial and implanted material data fall in wide electron density ranges, i.e. 10^{17} cm^{-3} for the former and $10^{19} - 10^{20}$ cm^{-3} for the later, a simulated electron mobility curve for 4H-SiC, computed by the Caughey-Thomas model [31], [32], has been

plotted in Fig. 2.7 to show that the carrier mobility of the MWA and RFA specimens of this study, as well as those published in ref. 23, fall in the expected region for an ideal uncompensated 4H-SiC material.

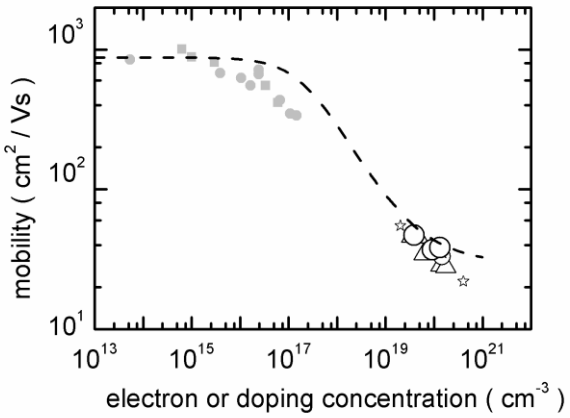

Figure 2.7: RT electron mobility versus electron concentration in epitaxial 4H-SiC (close symbols) adopted from refs. 26-27 and in P^+ implanted specimens (open symbols) adopted from ref. 3 (☆) and results of this work: MWA (○) and RFA(△) samples. The dashed curve is a description of the electron mobility in 4H-SiC versus doping concentration through the empirical Caughey-Thomas model [28] using the parameters from ref. [29].

2.2.3 X-ray diffraction study

Fig. 2.8 shows the (0004) diffraction scan of the as-implanted 4H-SiC sample with a P^+ concentration of 1×10^{20} cm^{-3}. A main peak at $2\theta = 35.652°$ which corresponds to out-of-plane lattice parameter *c* equal to 10.064 Å is originated from the un-implanted region of the sample. The farthest peak on the low-angle side indicates the presence of a

sub-lattice with larger inter-planar spacing corresponding to the ion damaged region that is rich of P, Si and C interstitials. In the case of Fig. 2.8 such farthest peak is at 35.296° and measured sub-lattice value is 10.163 Å (9.9×10^{-2} Å larger than virgin 4H-SiC). The sub-lattice values for different implanted P^+ doses and different annealing processes are shown in Fig. 2.9(a). In the case of the as-implanted 4H-SiC crystals, the lattice enlargement is more visible for P^+ concentrations $\geq 4 \times 10^{20}$ cm^{-3}. After annealing, irrespective of the annealing type, the lattice enlargement is apparent even in the sample that has been implanted with the lower P^+ concentration of 1×10^{20} cm^{-3}. Actually, after post implantation annealing the lattice parameter increase is higher than that measured in as-implanted sample for any P^+ dose except for the highest dose of 8×10^{20} cm^{-3}, for which both the as-implanted and annealed specimens have identical lattice parameters. This trend can be explained with the hypothesis that unintentionally channeled P^+ ions [33]–[36] generate an enlargement of the 4H-SiC lattice when they reside on interstitial positions and that a further increase of the lattice parameter takes place when they occupy substitutional positions after post implantation annealing. An additional contribution to the lattice parameter enlargement after post implantation annealing may come also from the in-diffusion of Si and C interstitial atoms from the implanted layer towards the bulk during post implantation annealing[37].

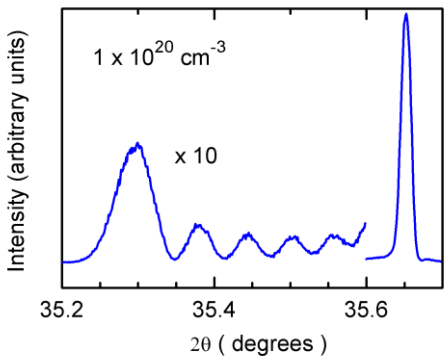

Figure 2.8: High resolution 2θ/θ scan of an as-implanted 1×10^{20} cm^{-3} P^+ 4H-SiC specimen. The spectrum intensity for $2\theta \leq 35.6°$ has been enlarged by a factor of 10 for making visible a satellite peak at the farthest angle from the main peak and fringes in between these two peaks.

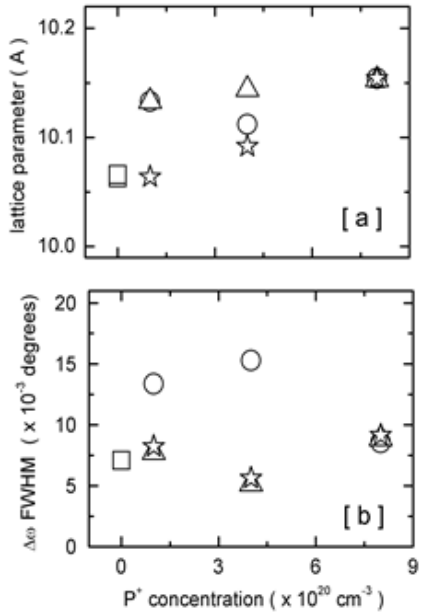

Figure 2.9: (a-b): The (a) lattice parameters and (b) the Δω FWHM that have been computed from the X-ray (0004) Bragg scans and rocking curves, respectively, are plotted versus implanted P^+ concentration for virgin 4H-SiC (□), P^+ as-implanted (☆); 1950°C, 5 min RFA (○); and 2000 - 2050°C, 30 s MWA (△) 4H-SiC specimens. The data error bars are smaller than the symbol dimensions.

Fig. 2.9(a) shows, may be for the first time that the average lattice parameter of a 4H-SiC crystal over a depth of about 3 μm underneath a very thin P^+ implanted layer is enlarged with respect to that of a virgin material. It should be emphasized that the penetration depth of the X-rays in the 4H-SiC material is 3 μm.

The additional subsidiary peaks that appear in Fig. 2.8 between the main peak and that of the defect sub-lattice, sometimes referred to as Kiessig fringes, are the result of an interference between X-rays reflected from the top and bottom faces of the P-implanted SiC damaged layer whose thickness can been calculated from the equation:

$$t = \frac{\lambda}{2(sin\theta_n - sin\theta_{n-1})}$$

where t is the thickness, λ the wavelength of the X-rays, and θ_n the Bragg angle of the n_{th} Kiessig fringe. Using successive two-theta positions of the Kiessig fringes, the thickness of the implanted layer is calculated to be 160 nm for the sample of Fig. 2.1. This value is in very good agreement with 150 nm obtained from the FWHM of SIMS and simulated Pearson IV profiles of the same sample.

The FWHM of rocking curves are shown in Fig. 2.9(b) for virgin, as-implanted, 1950°C, 5 min RFA and 2000°C, 30 s MWA 4H-SiC samples as a function of implanted P^+ concentration. The X-ray rocking curves provide information about both un-implanted bulk and implanted surface layer. As the sample was originally 8° off-cut from the c-axis, depending on the incident X-ray beam angle, the additional subsidiary peaks can be well separated from the main peak (either side of the main peak) or can actually overlap with the main peak, in such a case it is difficult to obtain information about implanted region as it is not possible to resolve subsidiary peaks. When measurable, the FWHM of the

satellite peaks of the rocking curves of MWA and RFA specimens have very similar values. This indicates that the homogeneity of the crystalline order in these implanted layers is independent of the annealing technique, at least for the annealing temperatures and durations that have been used in this study.

Conclusion

The pyrolysis of a spin-coated photo-resist film at 900°C in forming gas $N_2(10\%H_2)$ produces a C-cap suitable for the post implantation annealing of 4H-SiC at temperatures as high as 2050°C. The RMS surface roughness of this C-cap and that of the underling SiC are lower than 1 nm, independent of the post implantation annealing temperature and the implanted P^+ dose used, which is well-suited for planar electronic device fabrication technology.

The saturation of the material resistivity of P^+ implanted 4H-SiC towards a value in the low 10^{-3} Ωcm decade is confirmed by this study which is in agreement with previously published results. But this work has also shown that the asymptotic resistivity value can be reduced by a factor of two by increasing the post implantation annealing temperature from 1700°C to 2000°C and by increasing the implanted P^+ concentration up to a value of 4×10^{20} cm^{-3}. An increase of the implant/annealing parameters beyond these values does not bring any apparent benefit. A minimum material resistivity of about 1.5×10^{-3} Ωcm that corresponds to a minimum sheet resistance of 70 Ω/□ has been obtained in this study.

The measured upper limit of about 1.5×10^{20} cm^{-3} for the electron concentration at RT in P^+ implanted layers after annealing at 1950 - 2000°C is in good agreement with the modeled substitutional concentration at thermal equilibrium and maximum electrical activation of P in 4H-SiC between 1400°C and 2200°C. Such an agreement indicates a fast quenching rate of the studied thermal processes, both RFA and MWA that enables the incorporation of P in the substitutional position of 4H-SiC lattice to its thermal equilibrium value at the post implantation annealing temperature.

The electrical characterization of the P^+ implanted 4H-SiC layers shows minor differences between MWA and RFA samples. A higher electron mobility for identical carrier density in the MWA specimens than the RFA ones may indicate a superior crystalline quality of the former, however this phenomenon is not reflected in the results of the structural characterization.

The bulk crystal structure of 4H-SiC below the implanted layer is better in the case of the MWA specimens than in that of the RFA specimens. This could be a crucial feature in favor of the MWA because the depletion region surrounding the implanted n^+ layers penetrates into the bulk unimplanted region.

Chapter Three: Addressing p-type Bottleneck of 4H-SiC by Aluminum Implantation near Degeneracy

Motivation and background

Ion-implantation is the only feasible selective area doping technique for SiC because most of the doping species in SiC have an extremely low diffusion coefficient. Aluminum (Al) and Boron (B) are the most common acceptor (p-type) impurities in SiC. The former has a lower ionization energy and is immobile during post implantation annealing up to a temperature of 2100°C [19], therefore, the implantation of Al ions is preferred when elevated free hole concentrations are required. However, after conventional post implantation annealing treatments at a temperature as high as 1800°C, the Hall carrier density in an Al+ implanted 4H-SiC layer increased for increasing implanted Al+ concentration, from 2×10^{20} cm^{-3} to 1.5×10^{21} cm^{-3}, but then saturated for a further increasing of implanted Al+ up to 3×10^{21} cm^{-3} [10]. A much more efficient implanted Al electrical activation was obtained by a post implantation microwave annealing of implanted Al+ concentration of about 1×10^{20} cm^{-3} and maximum microwave annealing temperature of 1900°C [15]. In this article, the results of a post implantation microwave annealing at temperatures > 2000°C on Al+ implanted 4H-SiC with various Al concentrations up to 8×10^{20} cm^{-3} are presented.

3.1 Experimental

Semi-insulating 4H-SiC wafers 8° miss-cut from the <0001> axis have been Al+ implanted at 400°C for obtaining almost flat profiles of 5×10^{19}, 1×10^{20}, 4×10^{20}, and 8×10^{20} cm^{-3} over about 330 nm depth from the wafer surface. Fig. 3.1 shows the Secondary Ion Mass Spectrometry (SIMS) Al depth profiles of these samples. A Cameca IMS-4f spectrometer has been used with a 8 KeV O+ primary ion beam. The integral of each Al SIMS spectrum has been set equal to the corresponding Al+ ion implanted dose. The full width at half maximum (FWHM) of these SIMS profiles is about 390 nm for all the samples.

The as-implanted SiC wafers have been protected by a pyrolysed photo-resist film (C-cap) that has been processed as described in [23]. The use of a C-cap during the annealing of ion implanted SiC has been first proposed in ref. [38]. A proprietary microwave annealing technology developed by LT Technologies LLC [21] has been employed for the post implantation annealing of the implanted samples in the temperature range of 2000-2100˚C for 30 s. The microwave field is coupled efficiently to the implanted sample using close proximity of a heavy doped n-type SiC dummy sample, which plays the role of heater [21]. Due to the close contact between the two samples and the gas ambient (95% N2 and 5% H2 forming gas at 1 atm pressure) used during annealing, the temperature of the two samples can be considered equal within a few degrees. Temperature of the dummy sample was measured by a pyrometer. In this work, a solid state based microwave power source, with a capability of varying operating frequency from 400 MHz to 1000 MHz and output power from zero to 350 W, was used.

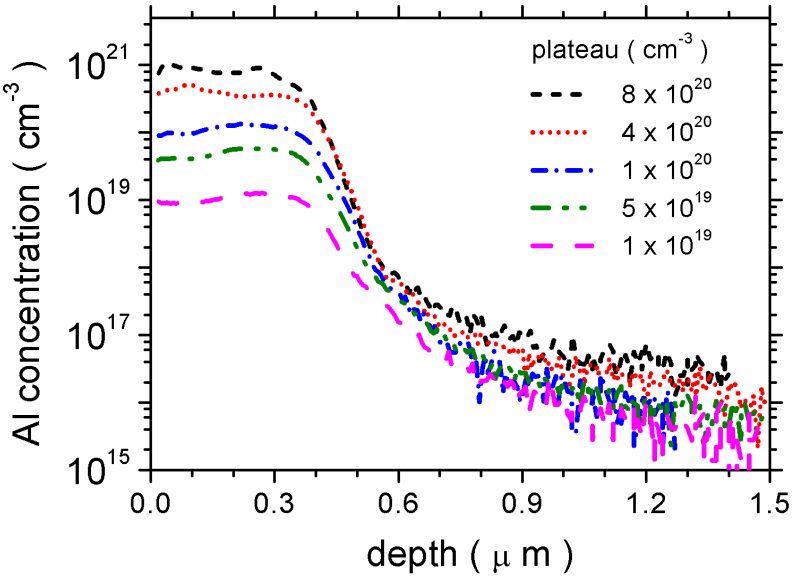

Figure 3.1: SIMS Al depth profiles of the as-implanted 4H-SiC specimens. Al plateau values are shown in the legend.

Square van der Pauw (vdP) samples of 5 mm × 5 mm have been fabricated on the annealed specimens for measuring the sheet resistance, the Hall hole density and the Hall hole mobility of the Al+ implanted and activated layers. All the electrical characterizations have been performed at room temperature (RT). Sheet resistance and Hall voltage values have been corrected for taking into account the contacts and VdP relative dimensions [24]. The sign of the Hall voltage in our samples has always been what is expected for positive charge carriers.

Two sets of Hall hole density values have been computed: one with a Hall factor r_H of 1 [39] and one with and an rH of 0.77 [40]. These different r_H values correspond to two alternative ways to treat the Hall carrier data of SiC samples that contain an elevated Al doping concentration. Often these samples have a temperature dependence of the Hall carrier sheet density that corresponds to an electrically activated Al sheet concentration higher than the implanted dose, which is not practically possible. In the literature, this fact has been justified by two different ways. Koizumi et al. [39] attributed a fundamental role to the Al excited states in the evaluation of the Al ionization efficiency, which gives an rH of about 1 at RT. Other groups [15], [41] extended the Hall factor temperature dependence that has been obtained on very lightly Al doped SiC specimens [40] to high doping concentrations. Hence, in this paper we present Hall carrier results obtained for both the r_H values.

Ohmic contacts have been fabricated with a Ti-Al bi-layer following the procedure described in ref. [10]. After contact alloying, a SiC surface cleaning in an oxygen plasma has been performed for removing carbon trace on the SiC surface that might have been formed during contact alloying.

3.2 Room temperature transport properties

The two sets of Hall hole area density data (for rH = 0.77, and 1) are plotted versus the implanted Al+ dose in Fig. 3.2. Both Hall hole area density and Al dose scales have been

converted into volume density scales (see the top and left axis of Fig. 3.3) by assuming an implanted layer thickness equal to the FWHM of the implanted Al profile. The use of logarithmic scales in Fig. 3.2 make the value differences less evident and the similar trend of these two sets of data is quite evident. Such a trend shows that the hole density at RT increases with an increasing Al+ ion dose over the entire dose range. This result is opposite to the saturation behavior observed in ref. [38] that is also shown in Fig. 3.2 for comparison.

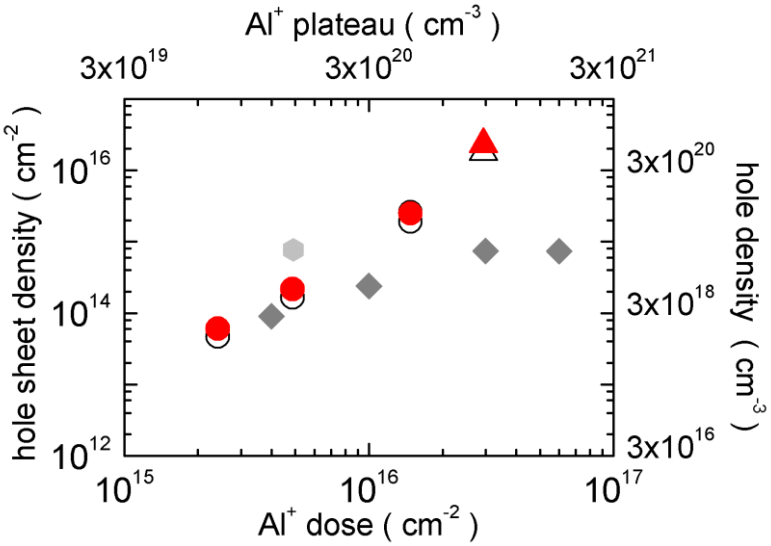

Figure 3.2: Hall hole density versus implanted Al+ dose for 4H-SiC samples that have been microwave annealed at 2000°C (○,●) and 2100°C (△,▲) for 30 s. Open and close symbols correspond to data obtained with r_H equal to 1 and to 0.77, respectively. Data of ref. [2] (◆) and [3] (⬟) are also shown for comparison.

This may be due to the higher post implantation annealing temperature of the present study, 2000-2100°C for microwave annealing compared to 1800°C for conventional annealing.

The measured free carrier density at RT indicates that the electrical activation efficiency of Al obtained in this study for every implanted Al concentration in 4H-SiC is better than that published until now in the literature [38], [41]. While the improvement is a factor of two or three for the lower Al doses, the improvement factor is 10 or more for the higher Al doses, which is quite exceptional. Values of 79% and 61% Al electrical activation at RT for r_H values of 1 and of 0.77, respectively, have been measured for the highest Al dose and microwave annealing at 2100°C. Such high values are unusual for Al in SiC and would be considered reasonable only if Al acceptor ionization energy had become very low, which could be due to, for instance, band-gap narrowing, or an intra-impurity band conduction that can take place in such a heavily Al doped 4H-SiC. Ruling out this as a measurement artifact has been excluded because the sign of the Hall coefficient always corresponds to positive charge carriers. The very high annealing temperature may result in a very efficient incorporation of the Al atoms in substitutional sites. A high Al concentration may also lead to the formation of impurity bands that favor the intra-band conduction at RT, or even the transition from the semiconductor to a metallic state. Low temperature Hall measurements may help to determine which of these two mechanisms is responsible for high conduction in our samples. Fig. 3.3 shows measured sheet resistance values versus implanted Al plateau concentrations. The vertical resistivity scale of Fig. 3.3 has been obtained by multiplying the sheet resistance scale by

the FWHM value (390 nm) of the implanted Al profile. A resistivity curve that has been computed by assuming a full electrical activation of the implanted Al and a hole mobility equal to that measured on epitaxial 4H-SiC materials [38] has also been shown in Fig. 3.3 for comparison. The sheet resistance values of Fig. 3.3 decrease for increasing Al concentration and reaches a minimum value of 550 Ω/□ for 8×10^{20} cm^{-3} Al+ and a microwave annealing at 2100°C for 30s. This minimum sheet resistance corresponds to a material electrical resistivity of 2×10^{-2}Ω·cm, which is about a factor of three lower than the minimum resistivity obtained in a previous study on microwave annealing of Al implanted 4H-SiC [15]. To the best of the authors knowledge, such a low value has never been obtained in Al implanted 4H-SiC that has been post implantation annealed in conventional furnaces.

In Fig. 3.3, the comparison between the resistivity values of Al+ implanted and microwave annealed 4H-SiC specimens and of epitaxial p-type 4H-SiC materials shows that the former is higher than the latter with a difference that decreases for increasing hole concentration values. Actually a direct comparison between implanted and epitaxial p-type SiC materials for hole concentration above about 4×10^{20} cm^{-3} is not yet possible because, to the best of the authors knowledge, such an elevated hole concentration has not yet been obtained by epitaxial growth.

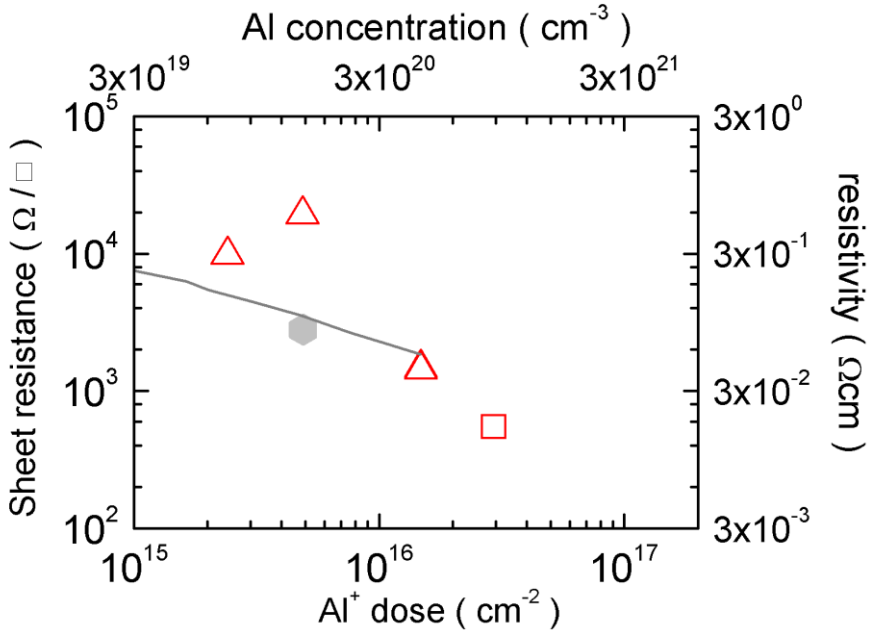

Figure 3.3: Sheet resistance/resistivity versus implanted Al^+ dose/ concentration for 4H-SiC samples that have been microwave annealed at 2000°C (△) and 2100°C (□) for 30 s. For comparison, the sheet resistivity curve for a full electrical activation of the implanted Al and a mobility equal to that in epitaxial p-type 4H-SiC material [2] (*continuous line*) is also shown. A datum from ref. [3] (⬟) is also shown for comparison.

Fig. 3.4 shows the Hall hole mobility values versus the Hall hole concentration for two different rH values. Like in Fig. 3.2, the trend differences between the two sets of data are minimal and every comment made about the Fig. 3.4 results is valid for both the data sets. The hole mobility curve of epitaxial p-type 4H-SiC [38] is also shown in this figure for comparison. In agreement with previously published data on Al implanted 4H-

SiC, the mobility data of Al implanted and annealed samples of this study are lower than those

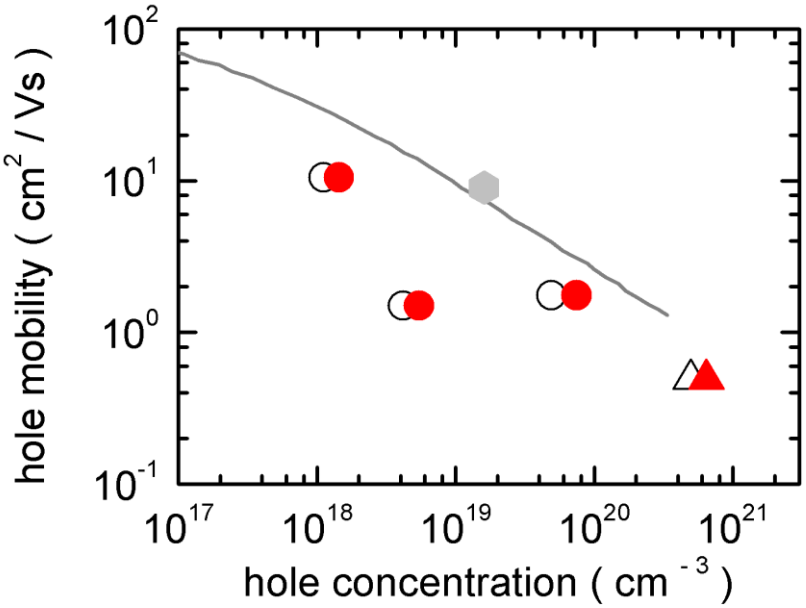

Figure 3.4: 7 Figure 3.0.2 Hall hole density versus implanted Al+ dose for 4H-SiC samples that have been microwave annealed at 2000°C (○,●) and 2100°C (△,▲) for 30 s. Open and close symbols correspond to data obtained with r_H equal to 1 and to 0.77, respectively. Data of ref. [2] (◆) and [3] (⬟) are also shown for comparison.

of 4H-SiC epitaxial materials. But mobility values as low as 0.5 cm^2/Vs and corresponding hole densities as high as those of Fig. 3.2 are in favor of the hypothesis that the status of the higher doses Al-implanted 4H-SiC layers is close to that of a metal in spite of the fact that in these sample current carriers are holes.

Because of differences in sample preparation and annealing conditions, a direct comparison between the results of this study and those of previous works is not possible. Nevertheless for the benefit of the readers in Figs. 3.2, 3.3 and 3.4, the results of the 1×10^{20} cm^{-3} Al+ implanted 4H-SiC microwave annealed at 1900°C for 30 s, data from ref. [15], have been added.

The Al profile plateau region of an Al implanted 4H-SiC behaves like a metal but the interface between the implanted layer and the bulk material can still behaves like a bipolar semiconductor thanks to the decreasing shape of the dopant profile at this interface that is intrinsic of the ion implantation processing. In ref. [42], the 4×10^{20} cm^{-3} Al+ implantation and 2100°C, 30 s microwave annealing has been exploited for the fabrication of a rectifying p-i-n 4H-SiC diode where the exceptionally high electrical activation of Al next to the surface has favored the formation of a ohmic contact on the p-type side of the p-n junction diode.

Conclusion

This study shows that microwave heating can be used for obtaining exceptionally high electrical activation for implanted Al concentration > 4×10^{20} cm^{-3} in 4H-SiC when the annealing temperature is > 2000°C. The elevated annealing temperature results in a better electrical activation at lower concentrations of implanted Al as well, but the elevated Al concentration may favor the formation of a new 4H-SiC material state that explains the exceptionally high value of the measured.

Chapter Four: Room Temperature Impurity Band Conduction in Al^+ Implanted 4H-SiC

Motivation and Background

The Ion implantation still is the most used technology for obtaining planar selective area doping and for achieving impurity doping far above the solid solubility limit. However, the process optimization to attain a low p-type sheet resistance ($<10^4\ \Omega/\square$) of SiC by ion implantation is still a bottleneck to exploit the full potential of SiC based bipolar devices. Due to the high thermal ionization energy of any acceptor species in SiC, at room temperature (RT) the activation percentage of implanted dopants is significantly low even for a high doping density, although an increased impurity concentration decreases the thermal ionization energy. In addition, high doping can lead to passivation of the acceptors by formation of precipitates and other defects, which leads to a drop in the hole mobility.

Aluminum (Al) is the preferred acceptor doping species in SiC because it does not diffuse during the mandatory post implantation thermal treatment [43], if implanted Al concentrations are lower than the Al solubility limit. A post implantation thermal treatment is necessary for the SiC lattice recovery and for the electrical activation of the implanted Al atoms. The state of the art in the electrical activation of implanted Al is >

70% with a compensation < 20% for implanted Al concentration in the range (0.5-1 × 10^{20} cm^{-3} by using post implantation annealing temperatures as high as 1950°C [44]. The increase of the post implantation annealing temperature to 2000°C by microwave heating has produced qualitatively similar results to those obtained by conventional annealing [45].

In this work the transport properties of p-type 4H-SiC materials with implanted Al concentrations in the range of $(1.5 – 5) \times 10^{20}$ cm^{-3} were studied after 1950 °C (by conventional furnace) and 2000 °C (by ultra-fast microwave heating system) post implantation annealing treatments. The implantation concentration is in the vicinity of Al solubility limit (2×10^{20} cm^{-3}) [46] which also provides the opportunity to explore the metal to insulator transition (MIT) of such degenerately doped large band-gap semiconductors.

4.1 Experimental

High purity semi-insulating, <0001> 8° off-axis (from c axis), 4H-SiC wafers was Al^+ implanted with different energy and dose values to obtain almost box shaped Al depth profiles next to the wafer surface. A Tandentron 1.7 MV accelerator (High Voltage Engineering Europa B.V.) and a 3 inches holder were used for sample mounting and heating. During implantation, the SiC samples were covered by a thick SiO_2 film and kept at 300°C or 400°C. Implantation schedules were decided by using SRIM2008 simulations and verified by Secondary Ion Mass Spectroscopy (SIMS) on few samples.

Homogeneous Al concentrations of 1.5×10^{20}, 3×10^{20} and 5×10^{20} cm^{-3} were obtained across a thickness of about 400 nm. The implanted wafers were diced into pieces of 5 mm × 5 mm for facilitating van der Pauw (vdP) Hall measurements. These pieces were annealed at 1950°C/5 min in a conventional inductively heated furnace ("conventional annealing," CA) or at 2000°C/30 s in a microwave heating system ("microwave annealing," MWA[21]. During CA and MWA the sample surface was protected by a carbon film (C-cap) which was obtained by a 900°C/2 min pyrolysis in forming gas of a 2-4 μm thick resist film [23]. Before the spinning of the resist film, the SiC native oxide was etched away in a hydrofluoric acid bath and samples were dried in nitrogen at 110°C for 30 min. After CA and MWA, C-cap was removed by 850°C/15 min dry oxidation.

C-cap is necessary to prevent SiC surface decomposition during the very high temperature post-implantation annealing [38]. Root mean square (rms) surface roughness after C-cap removal was measured by Atomic Force Microscopy in the tapping mode on a few samples and found to be in the range of 0.5-4.7 nm.

It is widely acepted that the Al implant does not outdiffuse during high temeprature annealing [15], [38]. Due to this reason, in this study it is assumed that the Al depth profiles in the as-implanted and annealed materials are identical.

Square van der Pauw (vdP) devices were obtained by fabricating triangular ohmic contacts on the four corners of each 5 mm × 5 mm annealed samples. For ohmic contacts, sputtered Ti(80nm)/Al(2%Si, 350nm) films alloyed at 1000°C for 2 min. in vacuum were used. Due to the non-negligible dimensions of the contacts compared to the device size,

correction factors were applied to the results of electrical measurements as suggested in Ref. [24].

Four point vdP Hall measurements were performed at the temperature range of 30-680 K using a 0.8 -1.0 T variable magnetic field. The samples of this study showed a Hall hole densities in the range of 7×10^{18} cm^{-3} to 1×10^{21} cm^{-3}. "Hall hole density" multiplied by the Hall factor r_H gives the "*drift* hole density" which is the true value of free carriers. Such a conversion was not always possible for most of the samples of this study for reasons which will be given in the "Results and Discussion" session of this chapter.

Table 4.1 Process parameters of the low resistivity *p*-type 4H-SiC here discussed. CA and MWA indicate conventional and microwave annealing, respectively: VI column specifies temperature and annealing times for each method. VII and VIII columns give experimental electrical data at room temperature (RT).

sample	**Nominal (SRIM2008) implanted Al density (cm^{-3})**	**Implant temp. (°C)**	**Measured (SIMS) implanted Al density (cm^{-3})**	**post implantation annealing**		**RT Hall hole density (cm^{-3})**	**RT resistivity (Ωcm)**
SiC305g	**1.5×10^{20}**	**400**	**n. m.**	**MWA**	**2000°C /30s**	**2×10^{19}**	**0.067**
SiC305b	**1.5×10^{20}**	**400**	**n. m.**	**CA**	**1950°C /5min**	**7×10^{18}**	**0.097**
SiC294c	**3×10^{20}**	**400**	**2.94×10^{20}**	**MWA**	**2000°C /30s**	**5×10^{19}**	**0.056**
SiC293a	**3×10^{20}**	**300**	**2.94×10^{20}**	**MWA**	**2000°C /30s**	**5×10^{19}**	**0.059**
SiC293e	**3×10^{20}**	**300**	**2.94×10^{20}**	**CA**	**1950°C /5min**	**5×10^{19}**	**0.052**
SiC296c	**5×10^{20}**	**300**	**5.34×10^{20}**	**MWA**	**2000°C /30s**	**3.5×10^{20}**	**0.023**
SiC296e	**5×10^{20}**	**300**	**5.34×10^{20}**	**CA**	**1950°C /5min**	**1.4×10^{20}**	**0.032**

4.2 Cryogenic transport result and discussion

RT In this section, the carrier transport characteristics of Al implanted 4H-SiC samples subjected to two different post implantation annealing methods (CA and MWA) are discussed. Table 4.1 summarizes the processing conditions and the RT electrical characteristics of all the samples of this study.

Figs. 4.1 and 4.2 depict the temperature dependence of the Hall hole density and mobility in samples of different implanted Al concentrations after 1950°C/5 min CA (closed symbols) and 2000°C/30 s MWA (open symbols). The different implant temperatures used did not have any significant effect on the transport properties. As is apparent, the MWA samples showed a higher carrier density and a correspondingly lower mobility compared to their CA counterparts for identical implant doses. These differences can be attributed to the 50 °C higher temperature of the MWA heating compared to the CA.

In Fig. 4.1, the sample with the lower Al implanted concentration of 1.5×10^{20} cm^{-3} shows a nearly exponential decay in the carrier concentration over the measured temperature range while the corresponding mobility increases, as shown in Fig. 4.2. These trends are typical of a carrier transport through extended states of the

valence band, in the hole freeze out regime. For these samples the hole density Arrhenius plots exhibit slopes which are consistent with a thermal activation energy of about 100 meV, in agreement with Ref. [44]. Moreover, at lower temperatures, the hint of a minimum in the Hall density data of the CA sample is evident in Fig. 4.1. Yet the corresponding mobility data in Fig. 4.2 exhibit an abrupt decrease with the decreasing temperature, steeper than the typical one due to ionized impurity scattering, which for a classical carrier gas follows a nearly $T^{3/2}$ power law or a weaker temperature dependence. The abrupt, steep decrease in mobility is generally recognized as mixed conduction effects due to the onset of a carrier transport through an impurity band [3], parallel to the valence band (VB) transport, which occurred around the temperature where the Hall carrier minimum appears, as depicted in Fig 4.1. Similar traits can be recognized for the samples with higher doping and conduction through impurity bands prevails at any temperature. In particular, a mixed conduction appears at higher measurement temperatures, revealed by a broadened minimum in the carrier density data, as shown in Fig 4.1. The temperature dependent carrier modulation shows a negative correlation with doping density. Moreover, the positions of the minima of the carrier density progressively shift towards a higher temperature with increasing doping density. In lower temperature regimes, the curves of both the 3×10^{20} cm^{-3} and 5×10^{20} cm^{-3} samples show carrier densities equal and higher than those measured at the higher temperatures, while the corresponding mobilities are quite low, as shown in Figs. 4.1 and 4.2. As elevated carrier density corresponds to a lower Hall voltage, the measurement becomes increasingly unreliable with the sample cooling, as evidenced by the progressive

increasing of the data scattering in both Figs. 4.1 and 4.2. Therefore, below a particular temperature, which is different for each sample with different implantation density, only

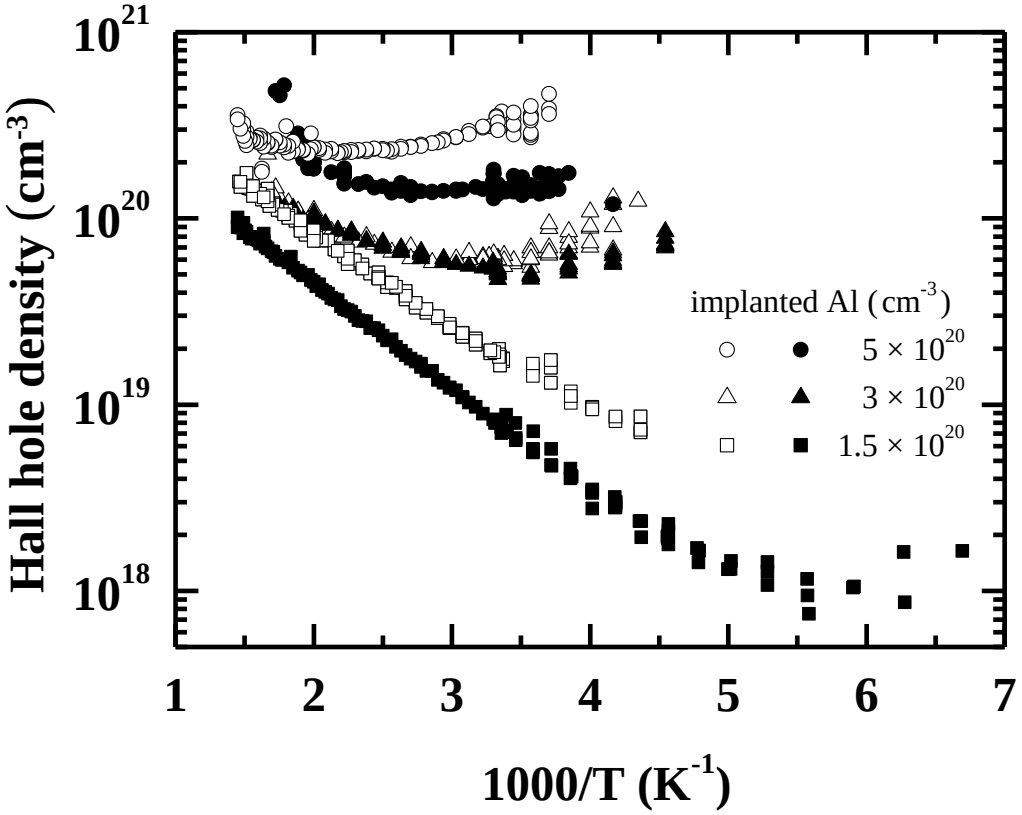

Figure 4.1: Temperature dependence of the Hall hole density of given Al implanted concentrations in <0001> 8° off-axis high-purity semi-insulating 4H-SiC and different post implantation annealing: CA 1950°C/5 min (full symbols), and MWA 2000°C/30 s (closed symbols). The experimental data were corrected for contact size systematic error (systematic error not discussed in text)

the results of the resistivity measurements are considered reliable. This is the reason that the temperature ranges of the Hall data of the 3×10^{20} cm^{-3} and 5×10^{20} cm^{-3} Al implanted samples are narrower than that of the 1.5×10^{20} cm^{-3} sample for both the post implantation annealing methods. In particular this is true for the 5×10^{20} cm^{-3} samples, whether annealed by CA or MWA, i.e., sample SiC296c or sample SiC296e, respectively: see Table 4.1 and Fig. 4.1.

A technologically relevant feature of the samples of this study is the observation of conduction through an IB near room temperature (RT), which is possible in p-type 4H-SiC owing to the high thermal ionization energy of the acceptors, but it effectively appears only for the implanted Al density $\geq 3\times10^{20}$ cm^{-3}. An IB conduction near RT has been previously reported for a much higher Al implanted concentration of 1.5×10^{21} cm^{-3} where the samples were annealed at a much lower temperature (1600°C/10 min) [47] than the present study. Such a feature opens up the possibility of obtaining Al implanted p-type 4H-SiC materials of almost constant hole concentration for any reasonable device working temperature resulting in more stable device characteristics for a given doping concentration. However, such heavily doped p-type Al implanted layers will have low carrier mobility [30]. This is highlighted in Fig. 4.3, where, for all the samples of this study, the RT Hall mobility is plotted as a function of Hall carrier concentration. In Fig. 4.3, the continuous line depicts the experimental trend of mobility for 4H-SiC epitaxial materials with hole densities in the range of 2×10^{17} - 2×10^{20} cm^{-3} [30]. However, it should be noted that for hole density > 1×10^{19} cm^{-3} , the mobility values reported by Matsunami et al. [30] are lower than those given by the extrapolation of the empirical

"Caughey and Thomas'' [31] algorithms [48]. This might be due to the fact that the highest carrier density of Matsunami et al. [30] exceeds the maximum density for Hatakeyama et al. (2×10^{18} cm^{-3}) [48] and Schaffer et al. (2×10^{19} cm^{-3}) [49]. This is relevant because the mobility trend described by the empirical "Caughey and Thomas'' formula is often taken as reference in the code for the simulation of the SiC device performances. In the present study, a direct comparison between experimental data of implanted and epitaxial 4H-SiC materials has been preferred. Fig. 4.3 shows that the implanted samples have a moderately lower mobility with respect to the epitaxial material of comparable carrier density. This can be due to the presence of a higher structural disorder (such as lattice mismatch between implanted and un-implanted layers or extrinsic stacking faults[50] in the implanted and annealed 4H-SiC material than in the epitaxial one

An important aspect of mobility comparison which is often disregarded in the literature is the synonymous reference of Hall mobility and the *true* (*drift*) mobility. As an example, in Fig. 4.3 the mobility depicted from this study are Hall mobility data. Yet, the data type of Matsunami et al [30] is not mentioned even though it is used in Fig 4.3 for comparison. Neither the data of this study could be converted into *drift* values as explained in the next section. However, such phenomena does not hamper the comparison between the MWA and CA data of Fig. 4.3, as all these data are Hall mobility versus Hall hole density. Such a comparison shows that the two different post implantation annealing technologies allow us to obtain p-type material with almost identical Hall mobility versus Hall hole density curves.

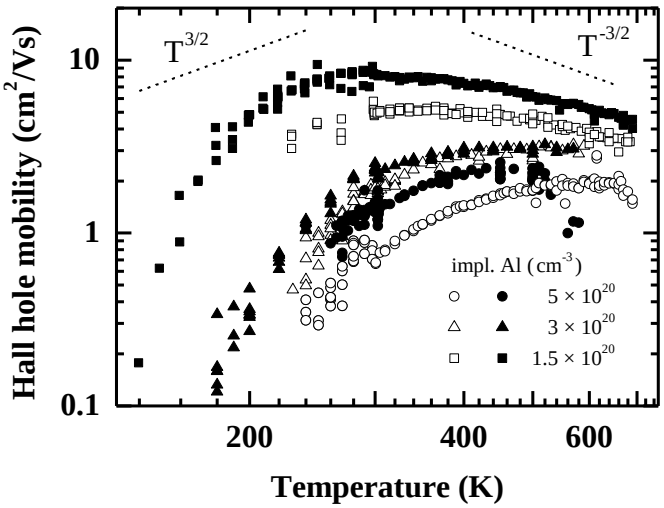

Figure 4.2: 9Temperature dependence of the Hall hole mobility of given Al implanted concentrations in <0001> 8° off-axis high-purity semi-insulating 4H-SiCand different post implantation annealing: CA 1950°C/5 min(full symbols), and MWA 2000°C/30 s (close symbols). The experimental data were corrected for contact size systematic error (see text). For comparison, the trends $T^{3/2}$ and $T^{-3/2}$ for ionized impurity scattering and non-polar phonon scattering, respectively, (classical hole gas) are shown as dashed lines.

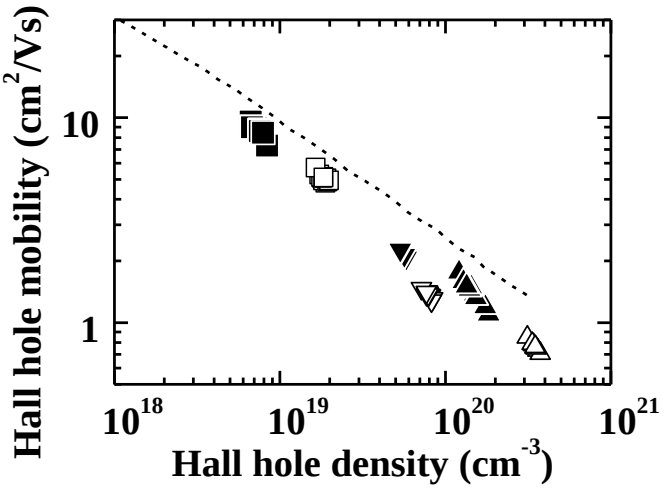

Figure 4.3: Hall hole mobility vs. Hall hole density at RT for the samples of the present work (symbols) and data for Al doped epitaxial 4H-SiC materials taken from the literature [30] (dashed line). Al implanted concentration of the 2000°C/30 s MWA (open symbols) and 1950°C/5 min CA samples (close symbols): (□ , ■) 1.5×10^{20} cm^{-3} , (▽, ▼) 3×10^{20} cm^{-3}, (△ , ▲) 5×10^{20} cm^{-3}.

To convert the Hall data into *drift* values requires a Hall factor correction. In a previous work [44] the validity of an empirically obtained Hall factor for hole transport through extended states in Al doped p-type 4H-SiC [51] was verified for acceptor concentration up to about 1×10^{20} cm^{-3}. The temperature range where electrical transport occurs only through valence bands can be reliably predicted, and an analysis of the Hall data can be performed by assuming the relaxation time approximation (RTA). For the samples of this study, such a data analysis is valid only in the cases of the low doped samples (1.5×10^{20} cm^{-3} implanted Al), featured by a hole freeze out of the Al acceptor states. Any other data of Figs. 4.1 and 4.2 would require a description of the Hall factor which takes into account a carrier transport though parallel channels due to extended and impurity states.

When the carrier conduction takes place through two parallel channels "1" and "2" the Hall factor can be written as

$$r_H = \frac{\sigma_1\mu_{1H} + \sigma_2\mu_{2H}}{(\sigma_1 + \sigma_2)(\mu_1 + \mu_2)} \qquad (4.1)$$

Eq. (4.1) is a general expression and can be easily extended for a higher number of parallel transport channels. In Eq. (1) σ_i and μ_{iH} are the conductivity and the Hall mobility in the i^{th} conduction channel (i = 1, 2). In the same channel of transport, the Hall and *drift* (*true*) mobility, μ_{iH} and μ_i, respectively, are generally different. The ratio μ_{iH}/μ_i is the *intra-valley* Hall factor, r_{Hi}, which, for a transport in a band of extended states (i.e. within the states of the valence or conduction band) can be computed in the frame of the relaxation time approximation. In this framework, r_{Hi} is defined as the

product of the scattering factor $r_{Si} = \langle \tau_i^2 \rangle / \langle \tau_i \rangle^2$ with the mass anisotropy factor r_{Ai}, that is $r_{Hi} = r_{Si} r_{Ai}$ [Wiley1975 and references therein][52]. The scattering factor r_{Si} accounts for the kinetic energy distribution of free carriers within a given band (for non-monokinetic carriers), whereas the mass anisotropy factor r_{Ai} is a correction to r_{Si} due to a possible anisotropy of such a band. For p-type 4H-SiC, Eq. (1) has been used in Refs. [39], [53], with some different assumptions, to describe the hole transport through the two parallel channels of the heavy and the light hole valence bands for acceptor concentration in the range 2×10^{15} - 1×10^{20} cm^{-3}. When a transport through impurity band is added to the transport through extended states, which is here the case for the 3×10^{20} cm^{-3} and 5×10^{20} cm^{-3} samples over the whole temperature range of measurements, a Hall factor similar to Eq. (1) generalized to three conduction channels should be used, but Eq. (1) in principle could still be applied under the assumption that, in one channel, carriers hop through localized impurities, and in the other one, carriers drift, for simplicity, in an effective valence band which include both heavy and light hole bands. For the hopping transport, the *intra-valley* Hall factor r_{Hi} can be considered equal to unity ($r_{Hi} = 1$), as for monokinetic carriers. In this case, in fact, the mobility is generally defined through a hopping probability which is thermally activated, and cannot be described in terms of an energy dependent relaxation time. A Hall factor for the samples of this study could be computed if the contributions of the two conduction channels could be decoupled, through the measurement of a magneto-resistance effect, for example. Unfortunately such a signal is too low to be detected in the samples of this study. Therefore, the conversion of the Hall values of Fig. 4.3 to *drift* ones is not possible.

Althought the *drift* carrier density values cannot be obtained from the data of Fig. 4.1 the following comment of these data can be made. Although none of the curves of Fig. 4.1 shows carrier exhaustion, the density data of the samples with the higher Al implanted concentration of 5×10^{20} cm^{-3}, which have a non-typical shape due to carrier freeze-out and show only a weak temperature dependence of the Hall carrier densities, could be used as a rough estimation of the net acceptor density (acceptor density minus compensating impurity density) in these samples. In fact, the latter can be considered approximately equal to the experimental density values measured at lower temperatures, where the IB transport dominates and a Hall factor value of 1 could be assumed. Such a very probable net acceptor value is about 3×10^{20} cm^{-3} for the 2000°C/30 s MWA sample, which may correspond to a 100% electrical activation for a 36% compensation, or to a 70% electrical activation for a 10% compensation. Both of these are reasonable hypotheses in the light of the electrical activation and compensation which has been obtained for Al implanted 4H-SiC samples in the range 5×10^{19}– 1.5×10^{20} cm^{-3} and 1950°C/5 min CA: 70% and 10-13%, respectively. [44]

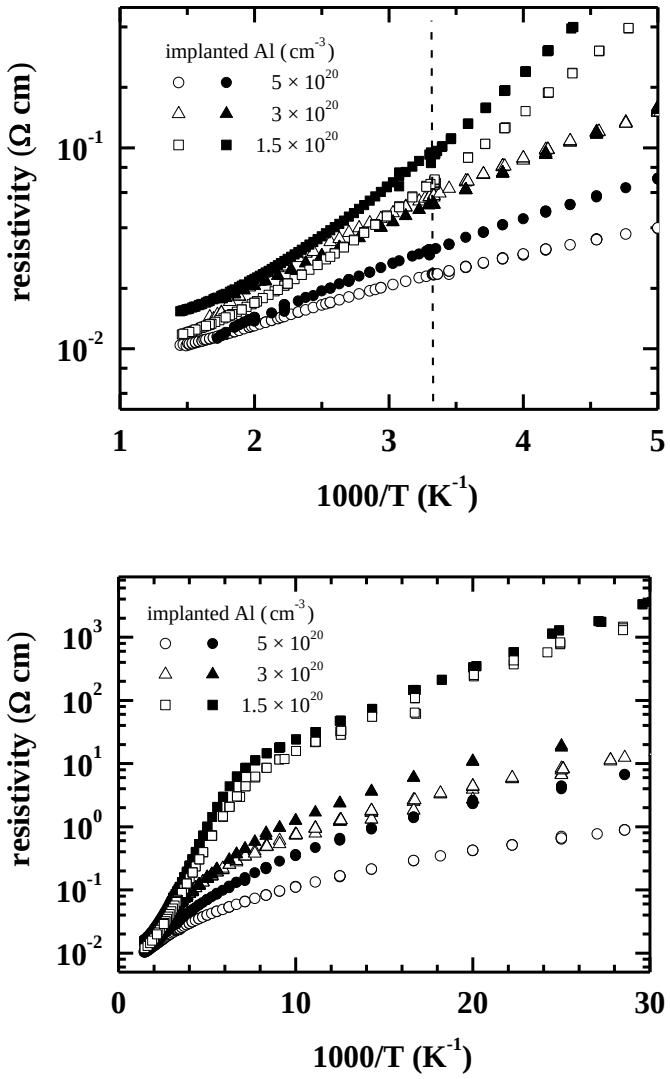

Figure 4.4: (a) (top)Arrhenius plot of the resistivity data for the samples here investigated, at temperatures near RT (what is the dashed line?). (b) (bottom)The same data in a wider temperature range. In both the figures, open and full symbols refer to samples annealed by MWA and CA, respectively. Continuous lines (I don't see any lines): fit of the low temperature resistivity with an activation law (evaluated activation energy: 20 meV).

The sheet resistance values are not affected by the Hall factor correction. Moreover, the sheet resistance measurements can be performed at lower temperatures than that of the Hall measurements as previously explained. Fig. 4.4(a) shows the Arrhenius plot of the resistivity data near RT. All the samples in this study have comparable trends in Fig. 4.4(a) featuring a thermally activated resistivity. The minimum RT resistivity obtained in this study is 0.023 Ωcm for the 5×10^{20} cm^{-3} Al implanted and 2000°C/30 s MWA sample. This value is only one order magnitude higher than the lowest n-type RT resistivity obtained for 4H-SiC by P^{+} implantation [42]. Fig. 4.4 (a) reveals the fact that for identical implanted Al concentration, a lower resistivity is obtained for the higher post implantation annealing temperature. In Fig. 4.4(a), the resistivity Arrhenius plot below RT shows a negative slope irrespective of the doping concentration featuring a semiconducting behavior. It should be mentioned that the experimental evidence of a MIT in p-type 4H-SiC was obtained for Al dopant concentration in the range 6.4×10^{20} - 8.7×10^{20} cm^{-3} in vapor-liquid-solid epitaxial 4H-SiC material [54]. Moreover implanted material is expected to contain much higher crystal disorders than epitaxial samples for identical dopant concentration. For a disordered material, hopping conduction could persist in spite of the elevated doping level which would result in the inhibition of the MIT.

Significant insight about the transport properties can be obtained from the resistivity Arrhenius plots as shown in Fig. 4.4 (b). As is evident, the Arrhenius plots of highest resistivity (Al concentration= 1.5×10^{20} cm^{-3}) samples exhibit two different slopes.

According to the pioneering model of Miller and Abrahams [55, p. 19], the conductivity can be written as the sum of three contributions:

$$\sigma(T) = \sigma_1 + \sigma_2 + \sigma_3 = \sigma_{01} e^{-\epsilon_1/K_B T} + \sigma_{02} e^{-\epsilon_2/K_B T} + \sigma_{03} e^{-\epsilon_3/K_B T} \qquad (4.2)$$

corresponding to the activation of the transport into an extended state band (ε_1), into the higher impurity Hubbard band (ε_2) and between impurity states (ε_3). Here K_B is the Boltzmann constant. Several experimental results [56], [57] support these predictions, more recently also supplemented by the Mott theory of the MIT [5] and by percolation theory (see for example Ref. [58]). Generally a linear trend in the Arrhenius plot of the low-temperature resistivity is attributed to nearest neighbor hopping conduction and its activation energy ε_3 varies with compensation and doping level [55], [56]. The possibility to detect the σ_2 contribution is restricted to a narrow temperature range and doping/compensation conditions [56], [57]. In this case, the slope of the low temperature linear behavior corresponds to an activation energy of about 20 meV, while the one near RT correspond to about 100 meV (see the discussion of the Figs. 4.1 and 4.2 data) for both CA and MWA samples. This piecewise linear type behavior is not clearly evident in the higher doped samples, where the transport between localized states extends to the higher temperatures (see Figs. 4.1 and 4.2).

Conclusion

In conclusion, the temperature dependences of the resistivity, of the Hall hole density and of the Hall mobility of Al^+ implanted HPSI 4H-SiC materials with Al concentrations in the range 1.5×10^{20} -3×10^{20}-5×10^{20} cm^{-3} and 1950°C/5 min CA or 2000°C/30 s MWA, feature: *i*) a semiconductor behavior for each implanted Al concentration; *ii*) the transition from a transport through extended states to a hopping transport through nearest impurity state below 200 K for the 1.5×10^{20} cm^{-3} implanted Al concentration; *iii*) hole density and hole mobility Arrhenius plots typical of a hole transport through impurity band states near RT for Al implanted concentration $\geq$ 3×10^{20} cm^{-3}.

The unusual electrical properties of the $\geq$ 3×10^{20} cm^{-3} Al implanted samples are due to the simultaneous occurrence of three aspects: *i*) implanted dopant concentration above the Al solubility limit at the temperature of post implantation annealing, i.e 1950-2000°C, *ii*) an improved efficiency of the electrical activation process due to the post implantation annealing temperature of 1950-2000°C, and *iii*) the high thermal ionization energy of the acceptors in p-type 4H-SiC permitting the favorable circumstance of the formation of an IB over a large temperature window around RT. Despite unavoidable defects due to implantation doping, slightly lower mobility values were obtained with respect to the epitaxial samples. The enhancement in carrier density achieved by the transport through the IB states overcomes the disadvantage of a reduced mobility typical for such conduction mechanism, resulting in a very low RT resistivity of 0.023 Ωcm for sample with 5×10^{20} cm^{-3} Al implantation dose and 2000°C for 30 s microwave anneal.

Chapter Five: Importance of Defect Mediated Conduction in Graphene-Metal Contact

Motivation and background

Understanding and controlling the graphene-metal interaction poses intriguing challenge for the graphene community. Controlled tailoring of the graphene-metal contact resistance (R_C) is essential for applications that exploit its extraordinary electronic, optical, thermal and mechanical properties. [59], [60]Both intrinsic and extrinsic effects contribute to graphene-metal R_C. Intrinsically, even though graphene is a semi-metal, the density of states (DOS) bottleneck near the Dirac point leads to an elevated R_C [61]. Moreover it has been suggested that the successive transformation between Dirac-like and Schrodinger-like carriers at the graphene-metal interface decreases the carrier transmission probability which results in a higher R_C.[62] Extrinsically, surface contamination introduced by polymers, solvents, chemicals and other adsorbates such as water-vapor during standard semiconductor processing modify the intrinsic properties of graphene through increased scattering [63]. Resist residue at the interface between the graphene and the metal has been shown to inhibit conformal deposition of metal on graphene, resulting in increased and inconsistent R_C[64]. Yet, unlike conventional semiconductors, resist residue on graphene surface cannot be cleaned using standard plasma-ashing due to the low selectivity between carbon-based resists and

graphene[65]. Also, p-n junction formation due to different work function between graphene and metal contacts may contribute significantly to R_C.[66]

In recent years, various strategies have been employed to achieve reproducible low contact resistance. Several groups have attributed low R_C to a clean graphene-metal interface [67], [68].Other approaches have enhanced the interfacial DOS and/or graphene-metal carrier transmission by intentionally damaging graphene by oxygen plasma[69], ultraviolet/Ozone treatment[70], contact area patterning [71],or by one-dimensional side contact[72]. Additionally, Wallace et al used *in-situ* X-ray photoelectron spectroscopy (XPS) to show that metal deposition on as grown chemical vapor deposition (CVD) graphene spontaneously form defects resulting in "end-contact" [73]. Another viable approach to tailor Rc is metal-graphene work function engineering[74]. Several groups have achieved relatively low contact resistance using Pd or Ni and higher contact resistance with Ti, Cr, and Al contacts[75]. However, Ti/Au contact resistances approaching quantum Rc values were recently reported [65], [67]. It has been theoretically suggested that the modulation in the graphene dispersion relation occurs when the metal chemisorbs on the graphene (Ti, Ni, Co, Cr and Pd) and not when the metal physisorps (Au, Ag, and Pt) [61], [73] which contradicts other experimental findings [75]. Moreover, Robinson *et al.*[69] have reported no significant dependence of R_C with contact metal.

One of the major limitations of prior contact resistance reports is that the graphene was always contaminated and/or modified before metal deposition by lithography resists, plasma etc. Recently two different groups [76], [77] have reported a

resist-free process to study residue free graphene-metal interface. Yet, in both studies, exfoliated graphene was used and due to the small size of the flakes, end contacting of the graphene was unavoidable.[77] In this work, we have developed a resist-free technique, which when used on large area epitaxial graphene(EG) grown on SiC permits the study of graphene–metal interaction without process induced artifacts such as resist residue or end-contacts due to mesa formation. Using this approach, we are able to determine whether a resist-free interface is sufficient and/or necessary to obtain a low R_C (limited by quantum contact resistance), and to verify if spontaneous defect formation during metal deposition is inherent to graphene.

5.1 Resist-free microstructures on epitaxial graphene:

5.1.1 Fabrication of Si shadow mask for metal deposition

The graphene samples were prepared by sublimation of silicon from a semi-insulating SiC (0001) substrate in an Ar atmosphere. The growth conditions have previously been shown to result in uniform graphene thickness[20]. van der Pauw (vdP) Hall and transfer length measurement (TLM) structures were fabricated by a photoresist-free process implemented with a custom made shadow mask (Fig. 5.1). In order to fabricate the shadow mask for contact metal deposition, a one μm thick SiO_2 film was deposited by plasma enhanced CVD (PECVD) on a standard 4-inch Si (100) wafer thinned to 100 μm by chemical-mechanical polishing (CMP). The test structures were then patterned on to the SiO_2/Si wafer by standard photolithography. The exposed SiO_2

was subsequently etched by a combination of wet-etch (buffered oxide etch) and dry-etch in a commercial deep reactive ion etching chamber (DRIE, 1000 W ICP, 150 W RF, 50 sccm CHF_3, 30 sccm O_2, 40 mT, 20°C). An SF_6-based chemistry was used to etch through the silicon wafer anisotropically in the same DRIE chamber (1000 W ICP, 9 W RIE, 100 sccm SF_6, 5 sccm O_2, 15 mT, -110 °C)[78]. The resulting SiO_2/Si mask was then placed on the graphene surface and a 50 nm thick Ni film was deposited by electron-beam evaporation.

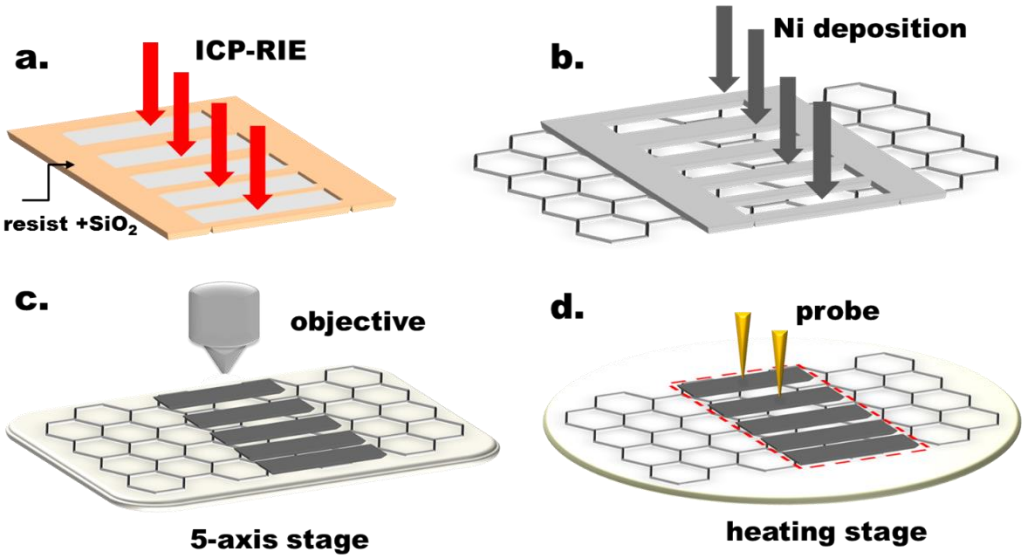

Figure 5.1: Process steps (a) Fluorine assisted ICP-RIE to prepare Si shadow mask. A stack of photoresist and SiO_2 was used as etch mask. (b) 50 nm Ni deposited by e-beam evaporator. (c) Device isolation by femtosecond laser. (d) *In-situ* annealing and electrical measurements. The red box shows isolated devices.

5.1.2 Femto-second laser assisted device isolation

For device isolation, the samples were illuminated by optical pulses from an amplified Ti:sapphire laser (Coherent RegA) at a repetition rate of 250 kHz with an 800 nm center wavelength and a 35 nm optical bandwidth (full width at half maximum)[79] . An optical pulse shaper located between the Ti:sapphire seed and amplifier pre-compensated for the system dispersion. BioPhotonic Solution's MIIPS system implemented the necessary feedback to the pulse shaper to produce 50-fs pulses at the sample.

The laser was focused with a 50x objective lens to approximately 1 μm diameter focal spot. Due to the tight focus, the Rayleigh range is also on the order of 1 μm. Thus, to maintain the focal spot while laterally scanning the sample requires <1 μm of height variation between our laser and the sample. To accomplish this, the sample was positioned on a 5-axis stage. The laser writing was performed by opening an electro-mechanical shutter and moving the sample in the two lateral dimensions to produce the desired pattern. Ablation of the graphene on a sub-micrometer scale was achieved with an average optical irradiance < 80 kW cm^{-2}, more than 4x less than for damage (not ablation) induced in graphene by continuous wave (cw) lasers [80]. Our average optical irradiance corresponds to < 3 nJ pulse energy and < 0.3 J cm^{-2} optical pulse fluence.

5.1.3 *in-situ* annealing and electrical, surface potential and Raman characterizations

Post isolation device electrical measurements were performed in a custom low vacuum (10^{-4} mbar) probe station. Measurements were performed *in situ* at room temperature (RT) before and after the sample was subjected to a 24 hr vacuum anneal at 200 °C. Immediately after the *in situ* anneal, RT Hall measurements were performed in air on 12×12 μm^2 vdP structures adjacent to the TLM structures. Post annealing characterization included scanning electron microscopy (SEM, Carl Zesis) and Raman spectroscopy (Thermo DXR) using a 9 mW 532 nm laser. Kelvin Probe Force Microscopy (KPFM) was performed on a Veeco D5000 scanning probe microscope in ambient conditions using a double pass technique with Co/Cr-coated silicon tip (radius of curvature of ~50 nm). Atomic force microscopy (AFM, Bruker Dimension Icon) and optical microscopy (Olympus BX51, edge detection Sobel filter mode) were employed to measure TLM pad distances (150 μm width, 5-60 μm spacings).

5.2 Results and discussion

Fig 5.2(a) depicts a SEM image of an isolated TLM structure before *in-situ* anneal. The deposited metal was conformal and extremely smooth with a rms roughness ≈ 0.25 nm (Fig 5.2(a)) inset). The isolation line width was about 800 nm as measured by SEM (not shown) and AFM (Fig. 5.2(b)). Some debris were produced during laser isolation and could be observed in the vicinity (≈1μm) of the isolation line, however, the active regions of the devices were free from debris, as can be seen in Fig. 5.2(d). A

Raman map of the graphene 2D peak intensity (Fig. 5.2(c)) shows the complete removal of graphene from the areas damaged with the laser. It should be noted that the graphene immediately neighboring the isolation line was not altered due to the use of a pulsed laser. Here, graphene is ablated on a femtosecond time scale where the irradiation is 4x lower than needed to damage the graphene with cw laser (the cw laser damage is likely due to local heating).[23] For cw lasers, the high heat capacity and thermal conductivity of graphene influence the ablation process and create a damaged area much larger than the laser spot size.

However, pulsed lasers have the potential for nonlinear absorption. Their subpicosecond energy absorption times are much faster than thermal or acoustic processes, thereby enabling patterning that has smaller damage areas with sharper boundaries.

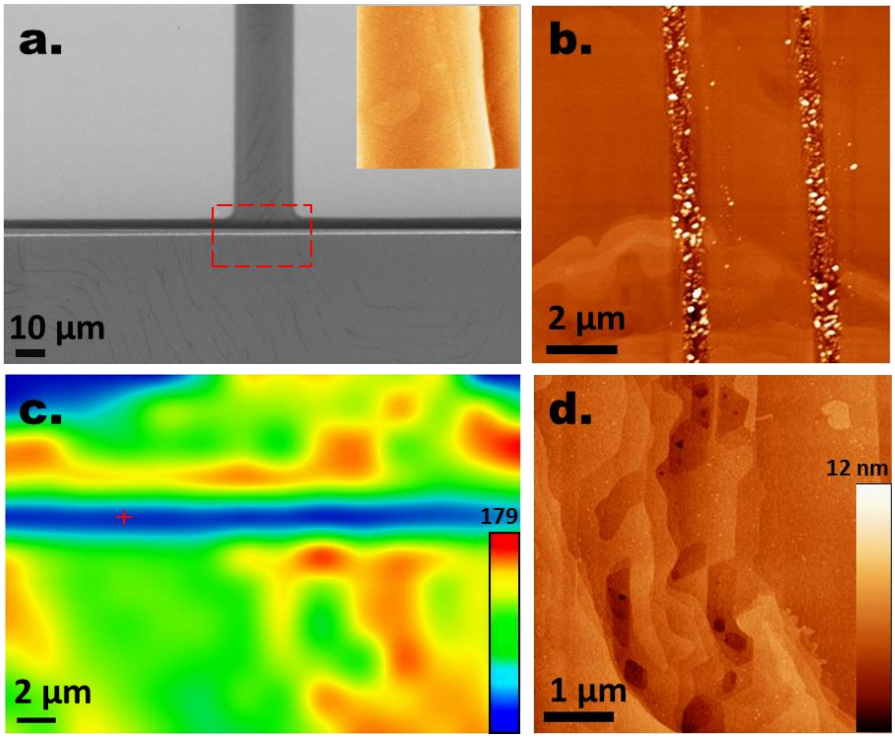

Figure 5.2: (a) InLense SEM image of an isolated TLM structure. The white straight line is the laser ablation. Inset 3 × 3 µm AFM height of image of Ni pad on graphene (rms roughness on terrace=0.24 nm). (b) AFM height image of isolation between adjacent TLM structures. (c) Raman 2D intensity map of the boxed area shown in (a). Color bar: arbitrary units. (d) AFM height image of graphene surface 5 µm away from the ablated lines shown in (b).

The size of the damaged region can be understood by incorporating the Gaussian spatial profile of the laser. A Gaussian beam diameter is determined at the points where the irradiance drops to $1/e^2$ of the peak value. However, a peak irradiance (e.g., >80% of the maximum value) occurs over a smaller diameter. Our 1-μm diameter laser spot used in this study produced a somewhat smaller damaged region in the graphene film. If the ablation threshold for graphene is met for an irradiance >80% of the peak value, then our laser-ablated region can be much smaller than the focussed laser's 1-μm ($1/e^2$) diameter.

Fig 5.3(a) shows an optical image of a representative Hall structure. The use of thinned Si wafer and optimized cryo-etch facilitated a shadow mask with a resolution ≈ 2 μm and SEM images (not shown) revealed no ragged edges indicating smooth sidewalls of the deposited metal. The Raman 2D peak full width at half maximum (FWHM) map of an isolated vdP cross is shown in Fig 5.3(b), where the isolation line is evident due to the absence of graphene 2D peaks. Fig 5.3(c) depicts AFM height image of a TLM structure. In this AFM image, a shadowing effect was observed due to the finite gap between the physical mask and graphene. However, it was ≈ 1 μm and included in the TLM calculation.

The KPFM image of the same TLM structure (Fig. 5.3(c)) reveals an average work function difference, $\Delta\phi = \phi_{Ni} - \phi_{graphene} \approx 0.35$ eV between Ni pads and graphene. This difference is roughly consistent with prior measurements of the Ni-(CVD) graphene work function difference of -0.2 to 0.4 eV by ultraviolet photoelectron spectroscopy (UPS) [74].

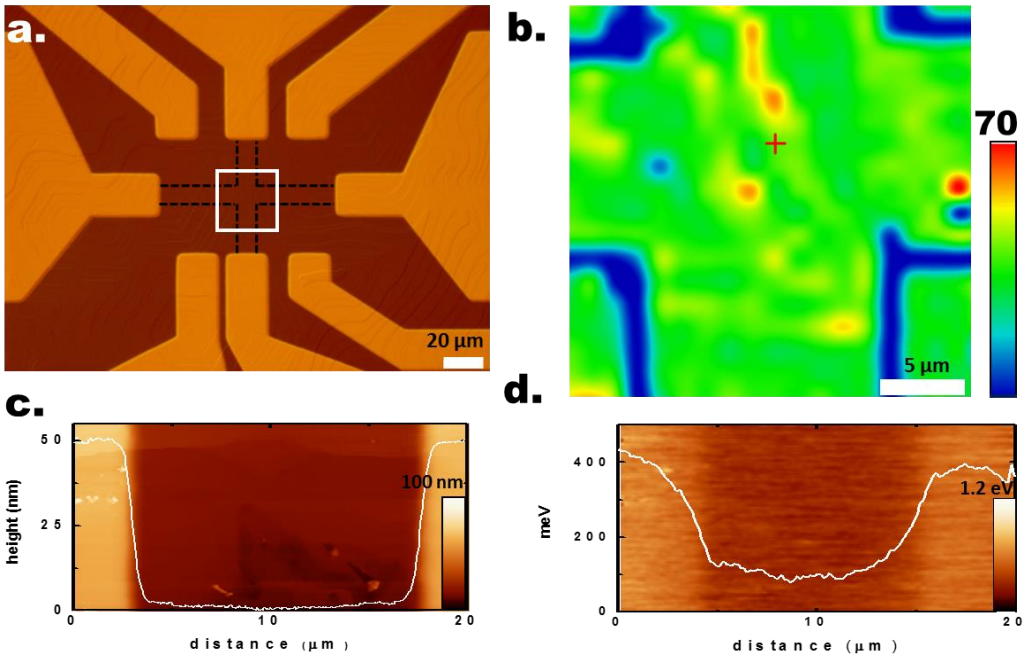

Figure 5.3: (a) Optical DIC image of a representative Hall structure fabricated by shadow mask (b) Raman 2D FWHM map of center portion of an isolated van der Pauw cross structure as shown in (a). (c) AFM and (d) KPFM height images of an isolated TLM pads.

Fig 5.5(a) depicts the RT I-V characteristics for various TLM separations of a representative device after annealing for 24 hr at 200° C. Ohmic behavior was observed for all three measured devices both before and after annealing. The inset of the Fig 5.4(a) shows the I-V behavior between two adjacent TLM structures which indicates good isolation. Fig 5.4.(b) plots the total resistance as a function of TLM pad spacing before

and after *in-situ* annealing. The contact resistances were calculated to be 2625± 105 Ω·μm

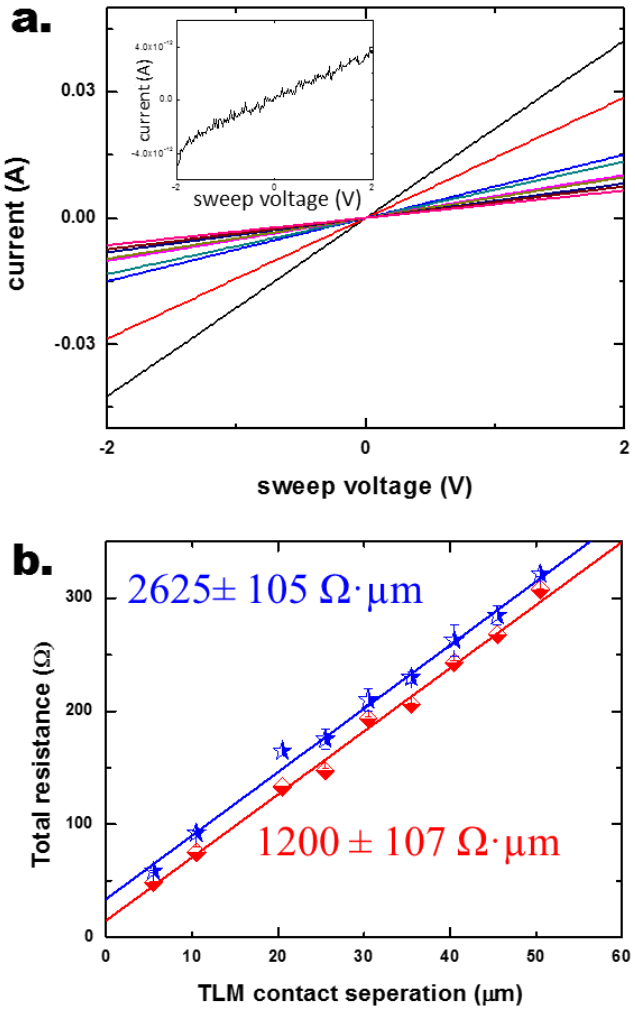

Figure 5.4: (a) RT I-V curves for different TLM separations after *in-situ* anneal showing Ohmic behavior. Inset shows isolation current. (b) TLM results before (blue stars) and after (red squares) *in-situ* annealing.

and 1200 ± 107 Ω·μm before and after annealing, respectively. However, , the sheet resistance under the metal before and after annealing were nearly identical, ≈ 840 Ω/□ as found from the slope of the TLM measurements.

The conductance (G) of a graphene-metal junction can be described by the Landauer-Buttiker model for one dimensional wire, $G = \frac{2e^2}{h}TM$ [81], [82] where T is the carrier transmission probability, M is the conduction mode in graphene, e is the electron charge and h is Planck's constant. Considering two valleys of graphene, it can be shown that the graphene-metal contact resistance is, $R_C = \frac{1}{T}\frac{h\pi^{1/2}}{4e^2 n^{1/2}}$,[72], [81] (5.1)

where n is the sheet density underneath the metal. We can calculate the quantum limited contact resistance from Eq. (1) by assuming perfect transmission (T=1) and using the measured Hall carrier concentration as an approximation of n. The room temperature 12 × 12 μm^2 vdP measurement showed an electron concentration ≈ 1.7 ×10^{12} cm^{-2}, mobility ≈ 1700 cm^2 V^{-1}.s^{-1} and sheet resistance (R_{Sh}) ≈ 2000 Ω/□. This results in a R_C of 88 Ω-μm, which is 12.5x lower than the value we obtained after annealing (1200 ± 107 Ω·μm).

The origin of such disparity can be attributed to two possible phenomena, neither of which is accounted for in our calculation. First, the carrier transmission probability (T) depends on $T_{M\text{-}G}$ (transport from the metal into the graphene) and T_C (transport from

graphene beneath the metal to the graphene channel), which can be expressed as $T = T_C T_{M\text{-}G}/(1\text{-}(1\text{-}T_C)(1\text{-}T_{M\text{-}G}))$[82]. Even though graphene is a semi-metal and exhibits high lateral conductivity, it essentially serves as an insulator for out-of-the plane conduction[83]. The absence of edge-state conduction in the TLM devices inhibits the metal-graphene carrier transmission hence reduces $T_{M\text{-}G}$. Additionally, theoretical work predicts that metal induced graphene doping depends on both the work function difference and graphene-metal surface distance [84]. In this study, the graphene Fermi level($\varepsilon_{F)}$ resides 0.35 eV above the Ni $\varepsilon_{F,}$ and it is expected that the graphene underneath the metal is p doped because of charge transfer, in agreement with the recent experimental evidence by Yang *et al* [74]. Since the graphene channel remains n-type, this will create a p-n junction. The transmission probability (T_C) through such a p-n junction will be smaller than unity [82]. Moreover intrinsic effects such as the momentum mismatch between the metal and graphene, finite graphene-metal distance, successive transformation from Dirac-like to Schrodinger-type carriers at the interface, carrier reflection due to non-normal incident angles also impede carrier transmission resulting in a higher contact resistance. Second, since the metal work function is unequal to that of the underlying graphene the *n* (hence R_{sh}) will differ from that of the graphene channel. Our RT vdP Hall measurement demonstrates this effect and the sheet resistances under the metal were markedly lower (more than 50%) than that of bare graphene.

In this study, a significant improvement (55%) of the R_C was achieved by vacuum annealing. From Eq. 1, contact resistance can be improved either by enhanced carrier transmission or by elevated carrier concentration. Generally, annealing reduces

adsorbates (which are responsible for weak p-type doping in graphene[85]) at the graphene-metal interface, hence reducing R_{Sh} underneath the metal[65]. This phenomenon was not observed in this study. We postulate that R_{Sh} was not improved by annealing either due to the absence of any extrinsic adsorbates at the interface or the graphene Fermi energy is pinned to a particular value due to the strong interaction with Ni [75]. As R_{Sh} is primarily dictated by the carrier concentration and sheet resistance was unchanged by anneal, we attribute the improvement of R_C to a significant enhancement of the carrier transmission, which is consistent with the previous studies[65], [71] .

5.3 Effect of Ni deposition and annealing on Epitaxial and CVD graphene

To unravel the effect of metal deposition on graphene lattice integrity, four 4x4 mm^2 epitaxial graphene samples (EG_1, 2, 3, 4; synthesized from one semi-insulating nominally on-axis SiC wafer) were patterned to contain large-area vdP Hall structures with Ti/Au (10 nm/300 nm) contacts deposited using e-beam evaporation through a shadow mask. Two of these samples (EG_2 and EG_4) were subsequently exposed to lift-off resist and S1811 (MICROPOSIT), flood exposed in deep UV and developed by CD-26 to simulate the effect of resist residue before metal deposition. 50 nm Ni was deposited by e-beam evaporation on all four EG samples and two CVD grown graphene samples (CVD_1, 2) after transferring on Si/SiO_2 by standard wet-transfer[31]. Samples (EG_3, EG_4 and CVD_2) were then annealed at 200˚C under vacuum (~10^{-4} mbar) for 24 hrs prior to etching the Ni film. The Ni was then etched from EG_1, EG_2 and

CVD_1 by the Ni etchant TFB at RT for ~5 min and confirmed by optical microscope and AFM. It was found that a much longer time (~15- 20 min.) was needed to completely etch the annealed Ni films as opposed to the un-annealed samples.

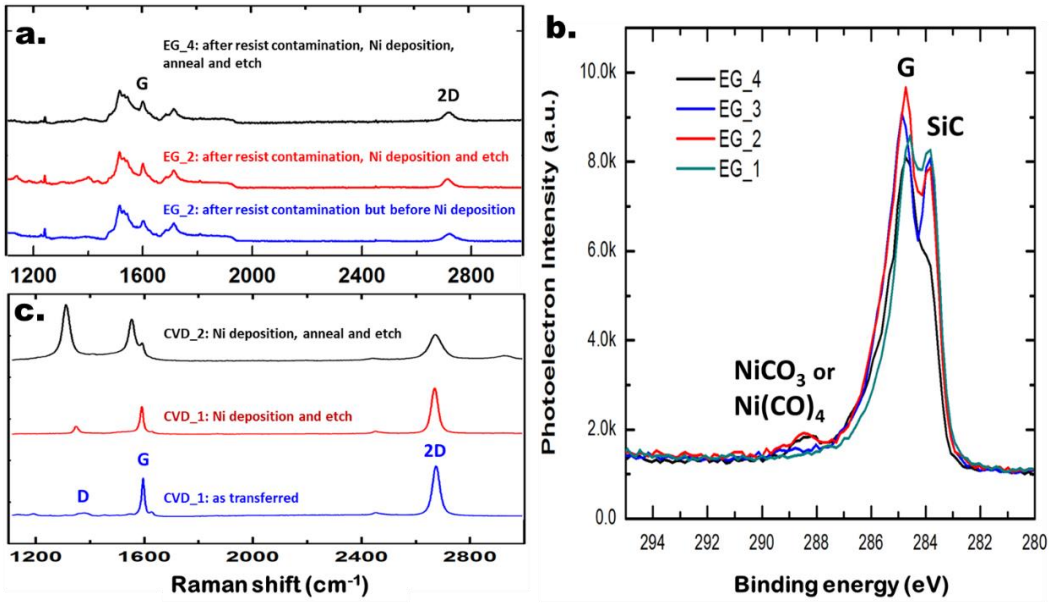

Figure 5.5: (a) Raman spectroscopy of graphene grown on SiC before and after Ni deposition and anneal (b) XPS data of four different samples as described in the text after Ni deposition and etch or Ni deposition, annealed and etched. (c) Raman spectroscopy of CVD grown samples before and after Ni deposition and anneal.

5.3.1 Raman characterization

Figure 5.5 depicts Raman spectra of EG (5.5(a)) and CVD samples (5.5(b)). The EG samples did not exhibit any defect peak (D peak ~1350 cm^{-1}) due to Ni deposition before or after vacuum annealing. However, the CVD films exhibited an increase in the D peak with the introduction of Ni. Additionally, the CVD films with the combination of Ni deposition and anneal treatment, have a prominent D peak indicative of significant damage to the underlying graphene lattice, as shown in Fig 5.5(b). Such a finding is in congruence with previous reports [17].

5.3.2 X-ray photo luminescence study

To gain more insight about the role of resist contamination at the graphene-metal interface, XPS was performed on all four samples with a Thermo Scientific k-Alpha system (spot size ~400 µm) using Al k-α radiation. Both the samples (EG_2 and EG_4) which were exposed to polymers showed (Fig 5.5(c)) an additional peak at 288.4 eV which are attributed to either $NiCO_3$ or $Ni(CO)_4$ [32]. However, samples with such contaminations showed similar or higher sheet resistance than those where no such peaks were observed (EG_1 and EG_3). Hence we infer that such contaminations are providing higher resistance paths than the graphene surface. Such non-conducting residues at graphene-metal interface potentially hinder carrier transmission which, incidentally, may alter the contact resistance. However the exact effect of such oxycarbide contaminants on R_C will be the subject of future study.

Nevertheless, two important conclusions can be drawn from this study. First, a clean graphene-metal interface is not sufficient to obtain a R_C limited only by quantum resistance, even though that might be a necessary condition for conformal metal deposition and reproducible contact resistance. Second, unlike CVD graphene, metal deposition does not form spontaneous "end-contacts" in epitaxial graphene, hence intentional edge-state conduction formation is required to obtain a low R_C[73]. Lastly, we surmise that the transmission coefficient is the intrinsic limiting factor for a pristine graphene-metal contact resistance.

Conclusion

In summary, we demonstrate a femto-second laser assisted direct patterning of graphene microstructures technique that enables us to study both intrinsic and extrinsic effects on the graphene-metal interface and graphene microstructures without modifying the graphene by polymers or other chemicals. We show that a clean graphene-metal interface is not sufficient to obtain contact resistance approaching the intrinsic limit set by the quantum resistance. We also found that the contact resistance is primarily limited by graphene-metal vertical carrier transmission and edge-state conduction is necessary to obtain contact resistance near the quantum contact resistance limit.

Chapter Six: *in-situ* Annealing Effect on Edge State Conduction of Graphene

Background and motivation

There has been a considerable effort in recent years to develop graphene devices that exploit its extraordinary electronic, thermal, and mechanical properties [59], [63]. However, during standard semiconductor processing, surface contamination introduced by polymers, e.g. lithography resists, modify the electronic properties through increased extrinsic scattering and uncontrolled doping.[63] Moreover, resist residue inhibits conformal deposition of metal on graphene, resulting in increased and inconsistent contact resistance (R_C).[64] Unlike conventional semiconductor materials, resist residues on graphene surfaces cannot be cleaned using O_2 plasma due to the low selectivity between carbon-based resists and graphene. While thermal annealing is routinely used to clean the graphene surface from physisorbed molecules,[86] it was found that poly(methyl methacrylate) (PMMA) residue on graphene was inadequately removed by this technique.[63] Current annealing[87] is not a viable approach for large area processing or before depositing metal contacts. Chloroform treatment[60] is not suitable for industrial application as it is harmful to the environment. Other methods employed are "gentle O_2 plasma",[69] low density inductive coupled Ar plasma[88] and ultraviolet (UV)/O_3 treatment.[70] These processes suffer from the drawback that if the process parameters are not properly tuned, plasma generated defects in the graphene result in

degradation of electronic properties. Hence these approaches are inappropriate for cleaning the active region of graphene-based devices, and may increase R_C due to damaged graphene in the contact area. Nevertheless, as benchmarks, Robinson *et al.*[69][b] reported a R_C of ≈ 100 Ω-μm by a combination of "gentle O_2 plasma" and post-metallization thermal annealing, and R_C ≈200 Ω-μm was obtained by UV/O_3 treatment.[70] The state-of-the-art graphene–metal contact resistance is below 100 Ω-μm,[67] but no information about sample processing is available.

Another approach to circumvent the resist residue problem is to deposit a removable protective layer prior to lithography. Various metals were investigated as protective layers, resulting in R_C ≈200-500 Ω-μm[68] and R_C ≈ 550 Ω-μm[89] using Al and Au, respectively. However, metal deposition can create defects in the graphene channel,[73] or modify the transport properties when metallic impurities are not completely removed from the channel region**.**

In this work, it is first shown that standard solvent cleaning and thermal annealing is insufficient to completely remove residue from the graphene surface left by any of the three different lithographic resists tested. However, by using a sacrificial lift-off resist (LOR) between the graphene and the same three resists, a clean graphene surface can be obtained following solvent cleaning and similar thermal annealing. Lastly, to assess the importance of such an approach, the temperature dependence of the graphene-metal R_C is studied.

6.1 Experimental: Achieving clean graphene surface by polymer-assisted conventional lithography technique

Epitaxial graphene was grown on 6H-SiC by sublimation of Si in ~100 mbar of Ar at 1520-1620^{0}C for 15-30 minutes.[90] Samples were then exposed to different families of polymer-based resists commonly used for device fabrication: Shipley 1811 (positive-tone photoresist), AZ 5214E (image reversal photoresist), PMMA (495-A2) and lift-off resist (LOR, MicroChem). LOR is a polydimethylglutarimide-based resist frequently used as an undercut layer in bi-layer metal lift-off processing. However, in this study, we have adapted LOR as a sacrificial layer. Table 1 describes the process flow for each polymer, with and without the LOR sacrificial layer. Post-fabrication annealing was conducted using either a commercial rapid thermal anneal system (Axic RTA), or in a custom ultra-high vacuum (UHV) chamber (base pressure 1 x 10^{-10} Torr). Post-processing characterizations were performed by tapping mode atomic force microscopy (AFM, Bruker Dimension Icon) and room temperature (RT) Hall measurements on 8 x 8 mm^2 samples using a fixed magnet van der Pauw (vdP) Hall system.

Table 6.1: Process steps using various photoresists with or without LOR sacrificial layer

Resists	Post bake	Exp. (nm)	Bake[a]	Exp[b] (nm)	Develop	Clean	Anneal
PMMA	170 °C/1 min	…	…	…	…	warm acetone, IPA[c], DI[d]	600 °C/10 min.(UHV)
AZ5214E	90 °C/1 min	320	110 °C/1 min	320	DI:AZ400K(4:1)	warm acetone, IPA, DI	400 °C/30 min. (Vac.)
S1811	120 °C/1 min	320	…	…	aqueous TMAH[e]	warm acetone, IPA, DI	400 °C/30 min.(Ar/H_2)
LOR, PMMA	Air dry, 170 °C/1 min	…	…	…	…	nmp[f] (60 °C), IPA, DI	400 °C/30 min.(Ar/H_2)
LOR, AZ5214E	170 °C/1min, 90 °C/1 min	320	110 °C/1min	320	DI:AZ400K(4:1), aqueous TMAH	nmp (60 °C), IPA, DI	400 °C/30 min.(Ar/H_2)
LOR, S1811	170 °C/1min, 120 °C/1 min	320	…	…	aqueous TMAH	nmp (60 °C), IPA, DI	400 °C/30 min.(Ar/H_2)

[a]Bake: reversible bake.
[b]Exp: reversible exposure.
[c]IPA is isopropyl alcohol.
[d]DI is distilled water.
[e]TMAH is tetramethylammonium hydroxide.
[f]nmp is N-methyl-pyrrolidinone.

6.2 Surface characterization

Fig 6.1(a) depicts an AFM topographic image of a sample that was processed with PMMA and underwent a standard wet clean and UHV anneal. It is evident from the speckling in the image that the high temperature anneal had limited success in cleaning PMMA residue from large areas of graphene. Moreover, the Hall mobility was reduced by 50% after our

UHV anneal, hence we performed subsequent anneals in a conventional RTA system at a lower temperature (400^0C) where no reduction in Hall mobility was observed. For AZ 5214E, it has been reported that the additional bake and exposure steps required when used as negative tone resist typically hardens the resist against solvent-based cleaning and results in residue at the metal/graphene interface.[91] In this study, we have found such residue is difficult to remove even by thermal annealing as shown in Fig 6. 1(b) where considerable debris is evident. The sample processed with S1811 revealed a

cleaner surface (Fig. 6. 1(c)) than the other two resists although residue after thermal annealing is present. To further confirm the interpretation of the AFM images, root mean square (RMS) roughness values extracted from 500 nm × 500 nm regions on the terraces of Fig. 6.1(a), (b), and (c) were 0.44 ± 0.07, 2.8 ± 0.2 and 0.43 ± 0.08 nm, respectively. These values are significantly higher than the RMS roughness of as-grown graphene, typically 0.1 ± 0.05 nm.

Fig 6.1(d, e, and f) depicts AFM topographic images of samples processed with a LOR sacrificial layer in addition to different resists used as top layers and processed as described in Table 1. As is evident, in each case it was possible to obtain a graphene surface exhibiting no evidence of residue after RTA. The AFM roughness of these samples was 0.09 ± 0.04 nm, similar to as-grown graphene roughness.

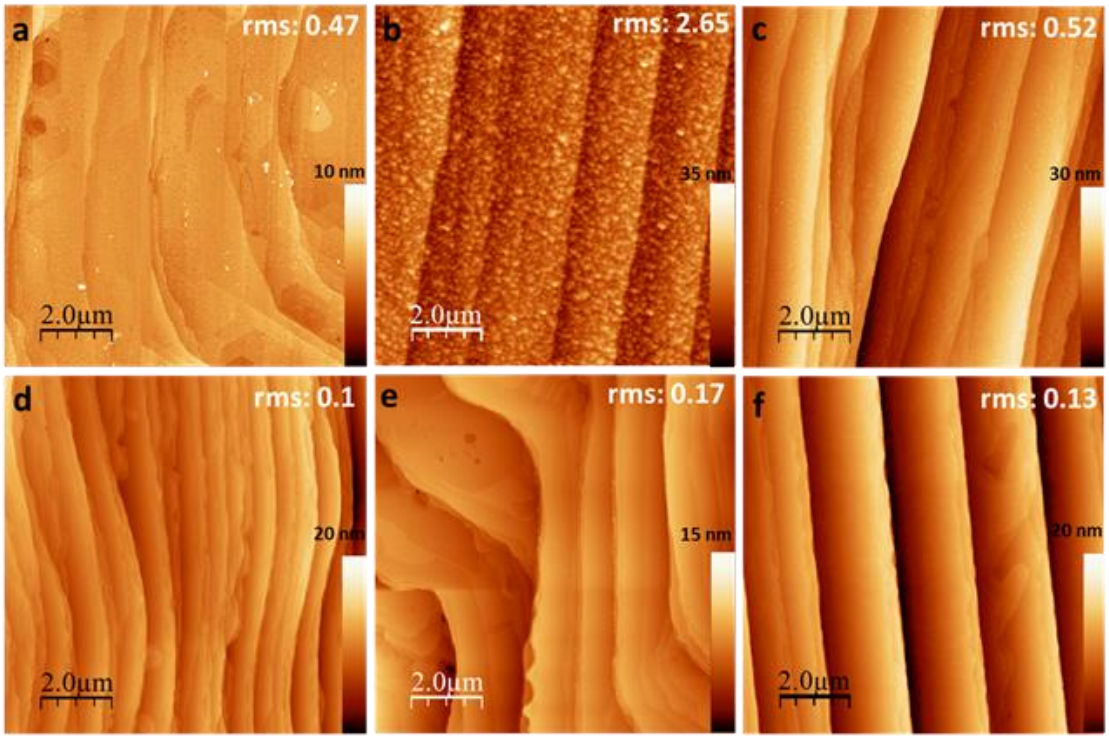

Figure 6.1: AFM images of samples after processing with (a) PMMA (b) AZ5214E (c) S1811 (d) LOR+PMMA (e) LOR+AZ5214E and (f) LOR+S1811, followed by solvent cleaning and thermal annealing as described in Table 6.1. Average RMS roughness of 0.5 x 0.5 μm^2 areas on the terrace for each sample is specified.

6.3 End-contacted Transfer length measurement device fabrication and *in-situ* anneal

To explore the effectiveness of the LOR sacrificial layer process, transfer length measurement (TLM) patterns were fabricated using standard photo-lithography. Only the LOR and S1811 resist process was used for the device fabrication part of this study since both positive and negative tone resists had similar surface morphologies following

optimization of the processing conditions. To facilitate TLM structures, isolated graphene rectangular mesas with varying gaps were patterned by O_2 plasma. Ti/Au (10 nm/50 nm) contacts were deposited by e-beam evaporation with ~ 5 μm graphene-metal overlap on each side of the individual mesas. We find this strategy ensures robust contact pads which is attributed to stronger SiC-metal adhesion than graphene-metal adhesion. Additionally, this strategy ensures edge contacts, which has been shown[72],[71] to lower the R_C. The TLM structures had a channel width of 140 μm and the length was varied from 4.5 μm to 24.5 μm in 5 μm steps. 12 × 12 μm^2 cross structures adjacent to the TLM structures were also fabricated for vdP Hall measurement. Since resist residue can result from each processing step, the LOR sacrificial layer was used prior to each application of the S1811 photoresist. Solvent-based cleaning and thermal annealing (Table 1) were performed after each lithography step. However, during the final patterning step (TLM metallization), the sample could be annealed only after metal deposition to avoid resist reflow. After metal deposition the sample was inserted in a custom low vacuum (10^{-4} mbar) probe station. Electrical measurements were performed starting at RT with subsequent measurements taken at 373, 473, and 523 K. The sample was then held at 523 K for 2 hours and electrical measurements were performed again at 523 K and subsequently at RT (hereafter the entire temperature dependent measurement cycle will be referred to as *in situ* anneal). Immediately before and after *in situ* anneal, RT vdP Hall measurements were performed in air on 12 × 12 μm^2 cross structures. After *in situ* annealing, further characterization included SEM (FEI Nova 600 Nanolab), electron

backscatter diffraction (EBSD) analysis using a hlk Technology Nordalys detector and Raman spectroscopy (Thermo DXR) using a 9 mW 532 nm pump and 0.7 µm spot size.

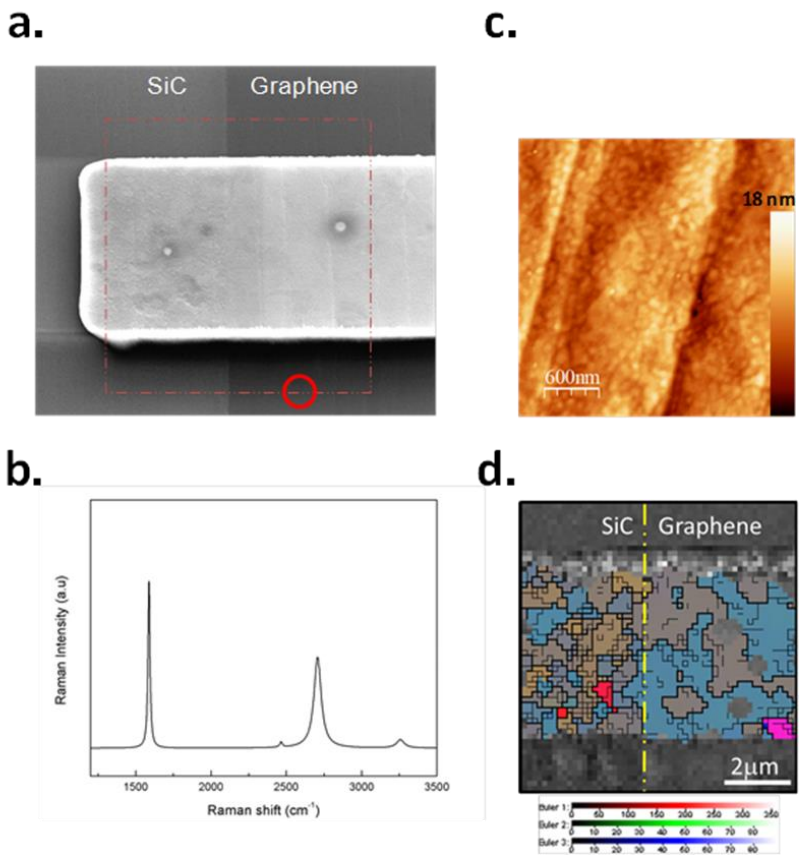

Figure 6.2: (a) SEM image of a metal finger on etched SiC (left) and on graphene (right) after annealing. (b) Raman spectroscopy of bare graphene (location given by red circle in panel a), after subtracting SiC peaks. (c) AFM image of metal on graphene (rms≈1 nm). (d) EBSD image of the boxed region in panel (a). The yellow line denotes the border between graphene and SiC. The scale bars show the coordination with Euler angle.

6.4 Surface morphology and structural characterization of graphene and metal on graphene

Fig. 6.2(a) depicts a SEM image of a metal finger on etched SiC and graphene after *in situ* annealing. The processing did not introduce significant defects into the graphene since Raman spectra, taken near the metal pad in Fig 6.2(a) and shown in Fig 6.2(b) did not exhibit a D peak near ≈1350 cm^{-1}. The SEM and AFM images, Fig 6.2(a and c), reveal conformal and uniform metal coverage that closely follows the underlying SiC steps. Since it was reported that Ni metal can grow epitaxially with a <111> texture only when deposited on resist-free graphene, [76] we characterized the metal using EBSD in conjunction with SEM. EBSD analysis of the boxed area of the SEM image is shown in Fig. 6.2(c), with all data reflecting Au phases since the Ti, Ti-carbide or Au-Ti phases are too thin for EBSD measurement. The image indicates that the Au over the SiC has a higher density of small grains (having a misorientation > 0.2º) than over the graphene surfaces (recall that the SiC was exposed to O_2 plasma during mesa isolation). Almost all phases of Au were oriented in the <111> direction, shifted by 60º. The only outliers in this were three red/pink grains, with <100> orientation. Recall that this sample could not be annealed prior to metal deposition, so the graphene-metal interface is not entirely free from resist residue. However, after *in situ* anneal, the EBSD analysis coupled with SEM and AFM reveals uniform and epitaxial metal growth on graphene. This implies that such optimized processing conditions reduce resist residue under the contacts and yields a clean exposed graphene channel. The latter is especially important

for top-gated devices, where the cleanliness of the interface between the graphene channel and the dielectric gate material is critical.[92]

6.5 Temperature dependent R_C behavior

For all measurement temperatures, the I-V curves in Fig. 6.3(a) showed reproducible linear behavior across the measured voltage range. Before *in situ* annealing, the sheet resistance (R_{Sh}) of the 12 × 12 μm^2 bare graphene vdP structure was 2068 Ω/□. Additionally, the Hall mobility and electron sheet concentration were 476 cm^2/Vs and 6.35 × 10^{12} cm^{-2}, respectively. The RT R_C was calculated to be 858 Ω-μm, and R_{Sh} under the metal was 1813 Ω/□. R_C decreased to 203 Ω-μm when the sample was heated and measured at 373 K. However, after this point the contact resistance gradually increased with increasing temperature, reaching 225 Ω-μm at 473 K and 301 Ω-μm at 523 K. After annealing the sample at 523 K for 2 hours, R_C reduced to 155 Ω-μm, which further decreased to 140 Ω-μm after the sample cooled to RT, as shown in Fig. 6.3(b) and (c). At this point, the sheet resistance under the metal was calculated to be 840 Ω/□, whereas the sheet resistance of the 12 × 12 μm^2 bare graphene was 1170 Ω/□ with a Hall mobility of 639 cm^2/Vs and electron sheet density of 8.34 × 10^{12} cm^{-2}. The vdP Hall measurements before and after *in situ* annealing confirm decreased carrier scattering following anneal since the final mobility increased despite an increase in carrier concentration. This could be a combined effect of removing resist residue and other adsorbates during the anneal, both of which are responsible for weak p-type doping in graphene.[85]

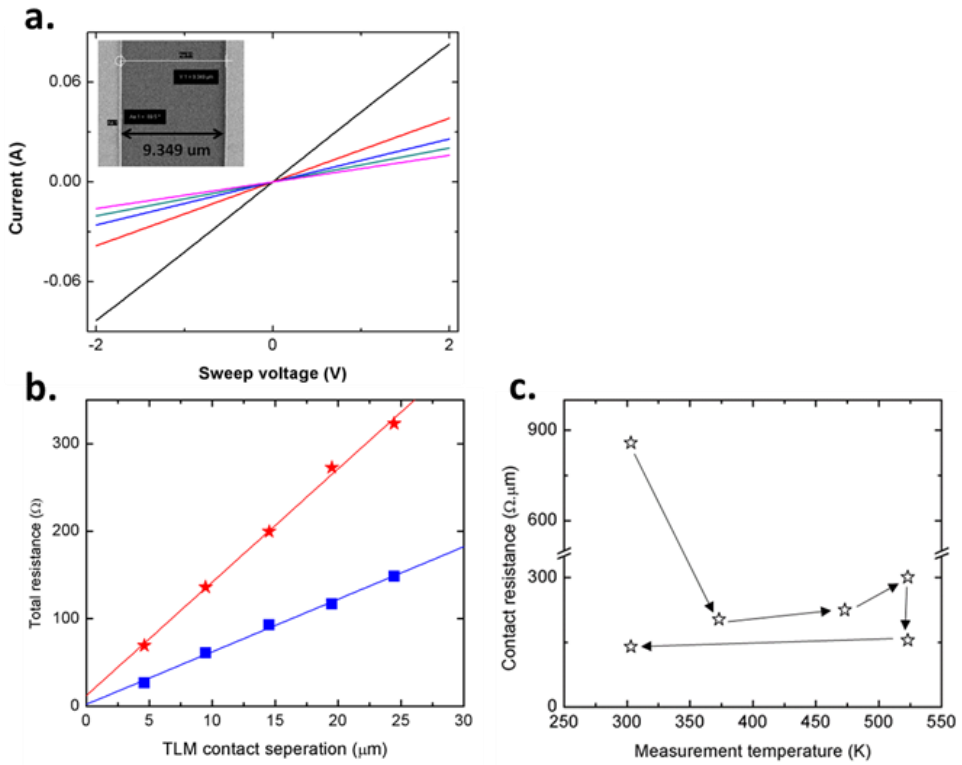

Figure 6.3: (a) Representative linear I-V characteristics of LOR+S1811 sample indicating ohmic behavior for varying TLM gaps at 100^0C. Inset showing SEM image of TLM structure. (b) Measured total resistance as a function of TLM separations. Red closed stars: before *in-situ* annealing. Blue closed squares: after *in-situ* annealing. (c) Contact resistance as a function of measurement temperature. The arrows indicate temporal directions.

6.6 Temperature dependent transport behavior of graphene-metal interface during *in-situ* annealing

Significant insight about graphene-metal interaction can be deduced from the temperature dependent TLM results. First, we attribute the dramatic improvement of R_C when the sample temperature was raised to 373 K to a significant increase in carrier transmission across the graphene-metal interface by bonding with the edge-contacted graphene, an interaction that is enhanced by the annealing process.[71] However, unlike a conventional semiconductor-metal junction, graphene-metal R_C is expected to increase with increasing temperature. This phenomenon can be explained by contact conductance (G) of graphene-metal junction using the Landauer-Buttiker model for one dimensional wire, $G = \frac{2e^2}{h}\sum_{i=1}^{N} T_i$ [81] where N is the number of occupied one-dimensional subbands, T is the carrier transmission probability, e is the electron charge and h is Planck's constant. The carrier transmission probability (T) depends on $T_{M\text{-}G}$ (transport from the metal into the graphene) and T_C (transport from graphene beneath the metal to the graphene channel), which can be expressed as $T = T_C T_{M\text{-}G}/(1-(1-T_C)(1-T_{M\text{-}G}))$.[82] $T_{M\text{-}G}$ can be represented by $\sqrt{\lambda/(\lambda_m + \lambda)}$, where λ_m is the graphene-metal coupling length and λ is the scattering mean free path. $T_{M\text{-}G}$ is expected to decrease with temperature since λ is inversely proportional to temperature due to enhanced carrier scattering at increased temperature whereas λ_m may only increase with temperature due to the anharmonic nature of the graphene-metal atomic vibrational potential. Hence, an increase in temperature leads to a decrease in $T_{M\text{-}G}$ and hence a decrease in T, which in turn, results in

increased contact resistance. For this analysis, we assumed T_C is unaltered and close to unity for our measurement temperature range due to Klein tunneling. [82]

We argue that during *in situ* anneal, two competing phenomena are taking place in the graphene-metal interface: 1) a decrease in R_C due to an improved graphene-metal interface as a result of annealing and 2) an increase in R_C as a result of decreasing carrier transmission at higher temperature. After initial improvement (phenomenon 1), the R_C is then dominated by increased scattering and/or increased graphene-metal coupling length during successive measurements at higher temperatures (phenomenon 2). However, after the sample was annealed for two hours at 523K, R_C was significantly lower (51%) than the prior value at 523 K and further decreased after the sample was cooled down to RT. Such a trend is consistent with our hypothesis about two competing effects during heating. This result contrasts with previous results[93] showing R_C continually decreasing over the same temperature range studied here, despite using similar metal contacts. We attribute such discrepancy to a graphene-metal interface dominated by resist residue which would result in reduced transmission probability.

Frequently, graphene-metal contact quality is quantified by contact resistivity which can be formulated as $L_T \times R_C$.[69], [93] The transfer length L_T is experimentally determined from TLM measurement. For conventional three dimensional semiconductors, this derivation assumes 1) the sheet resistances in the channel and in the semiconductor under the metal are identical and 2) semiconductor-metal contact is completely diffusive. Unfortunately, neither assumption holds for graphene. First, graphene will be doped by the top metal due to differing work functions and owing to its

two dimensional structure that leads to a different sheet resistance than that of the graphene channel. Our RT vdP Hall measurement demonstrates this effect as sheet resistances under the metal were always markedly lower than that of bare graphene. Second, the carrier mean free path in graphene is in the tens of nanometer range, so the graphene-metal junction is never truly diffusive.[82]

For ideal metal-graphene contact resistance, assuming perfect transmission (T=1), and two valleys of graphene, it can be shown that the graphene-metal contact resistance $R_C = \frac{h\pi^{1/2}}{4e^2 n^{1/2}}$, [72], [81] where n is the sheet density underneath the metal. Using the sheet carrier concentration measured in our work, n = 8 x 10^{12} cm^{-2}, R_C is predicted to be 40 Ω-μm which is 3.5X lower than the value we obtained. However, as discussed above, the graphene underneath the metal is always doped, further complicating the calculation. This analysis also assumes perfect transmission (T=1) which is unlikely in our sample owing to its relatively low mobility and the presence of steps.[94] Hence, we expect further reduction in contact resistance could be achieved in graphene with higher carrier mobility,[67], [82],[95] and by increasing the transmission probability and/or increasing sheet density of the graphene under the metal by contact area patterning[71] or gentle plasma cleaning.[69], [88]

Conclusion

In summary, we showed that employing a sacrificial LOR layer with conventional lithography resists, clean graphene surfaces were obtained after conventional solvent cleaning and thermal annealing. To assess the effectiveness of this approach, TLM

structures were fabricated using LOR and S1811. This approach did not impact the integrity of the graphene as shown by Raman measurements. Surface and crystallographic characterizations revealed uniform and epitaxial metal growth on graphene. It was necessary to anneal the contacts to 523 K for 2 hrs to obtain a room temperature R_C of 140 Ω-μm, which approaches current state-of-the-art results. Assuming the Landauer-Buttiker model, the temperature dependence of graphene-metal R_C was found to be consistent with carrier scattering. Further reduction of R_C is possible by increasing the transmission probability and/or increasing sheet density of the graphene under the metal.

Chapter Seven: Two Dimensional Disordered System: Functionalized Epitaxial Graphene

Background and motivation

The excitement generated by the achievement of metallic single layer graphene has obscured the fact that purely two-dimensional (2D) systems are not expected to be metallic.[7] A possible explanation for the metallic behavior is that massless Dirac electrons exhibit Klein tunneling and are thus, immune to the effects of disorder.[96], [97] This argument is contradicted by reports that the carriers actually have mass[98]–[100] and should, therefore, be described by the theory presented in reference 93. The clearly metallic behavior is an unquestionable addition to a series of systems such as high mobility metal-oxide field effect transistors (MOSFET)[101] and interface oxides[102] that have demonstrated such properties. These systems are presumed to be 2D due to their geometry but might have some three-dimensional character since the charge regions extend over finite distances that could explain their metallic transport properties. In contrast, graphene is a model system for studying the 2D metal-insulator transition (MIT). In this work, we systematically increase the resistivity of epitaxial graphene through exposure to low energy plasmas. These results reveal the existence of a 2D MIT in epitaxial graphene with carrier concentrations that are ~10^{12}-10^{13} cm^{-2} and mobilities that are ~10-1000 $cm^2/(V\text{-}s)$, values that are out of the range of applicability for the

models developed to describe the previous results on the high mobility MOSFETs[103], [104] but consistent with a more recent general scaling model.[105] In this case, the strongly localized state is separated from the metallic state by a weakly localized phase with $\sigma \sim \log T$ similar to results recently reported for thin films of RuO_2.

Key to unraveling this dilemma is determining whether an insulating state exists, whether a metallic state can be induced (clearly true) and, if so, understanding the nature of the 2D MIT. Previous work has shown that an MIT does indeed exist for graphene. For instance, Chen, *et al.* has demonstrated that insulating samples result through exposure to ion damage.[106] Bostwick, *et al.* claimed to observe an MIT by showing a large increase in room temperature resistance accompanied by a breakdown of the quasi-particle description as determined from photoemission in graphene exposed to atomic hydrogen although no low temperature data were reported.[107]On the metallic side of the transition, there have been several studies reporting weak-localization (WL) and/or enhanced electron-electron interaction (EEI), the two phenomena associated with the metallic phase above the MIT, in graphene with moderately high mobility.[108]–[115] Those results, while suggestive, are for graphene relatively far from the MIT where WL and EEI can be treated as corrections to the conductivity. That approach fails near the MIT, a quantum phase transition, where scaling models are needed to describe the properties.[2], [116] Thus, it appears that a scenario analogous to the three-dimensional case where the disorder driven MIT is described by a phase diagram with four regions:[117] insulating, critical, amorphous metal, and conventional metal can be observed for the 2D case. In this study the systematic increase in the graphene's sheet

resistance resulting from exposure to low energy plasmas has been used to determine a critical exponent of this phase transition and estimate the relative contributions of WL and EEI as the strongly localized phase is approached.

7.1 Experimental: Preparing and functionalizing epitaxial graphene

Several samples of epitaxial graphene were grown via Si sublimation from nominally on-axis SiC (0001) substrates.[90] Prior to graphene growth, substrates were etched in hydrogen at 1520°C, 100 mbar for 10-30 min. Graphene was then synthesized in 10 slm of Ar at 1540°C, 100mbar for 25-35 min. These conditions resulted in graphene with an average thickness of 1.5 layers. The samples were then fashioned into a pattern that enabled standard four-probe resistivity and Hall measurements with a polymer assisted fabrication process as described in chapter Six. Each sample was then systematically exposed to oxygen, fluorine, or nitrogen plasmas. Raman measurements indicated that the graphene remained intact after functionalization. It is important to note that very low currents were used for the measurements to ensure that local heating did not obscure the results.

As grown, the samples had R/square~1000Ω, carrier concentrations of ~10^{12}-10^{13} cm^{-2}, and mobilities ~700-900 $cm^2/(V\text{-}s)$ at room temperature. By exposing the graphene to the plasmas, the room temperature resistance eventually increased to values that exceed the quantum resistance $h/(2e^2)$. The samples can thus be driven through the MIT by systematically exposing the graphene to increasing plasma doses and

vacuum anneals (Fig. 7.1). The amount of induced disorder varied by element with F and O having the strongest influence. The sheet carrier concentration at 305K, as determined from Hall measurements, are $n \sim 10^{12}$-10^{13} cm^{-2} (supplementary). These values are comparable to those reported for MOSFET's ($\sim 10^{10}$-10^{12} cm^{-2})[118]. The calculated room temperature mobility as a function of calcination temperature shows significant scatter between ~100-1000 $cm^2/(V\text{-}s)$ (supplementary). These values are higher than those reported for oxide interface FET systems,[119]–[121] and smaller than those reported for conventional FET devices, $\sim 10^4$ $cm^2/(V\text{-}s)$.[118]

7.2 Metal-insulator transition in two-dimension

Fig. 7.1 a and b show data for N and O exposures clearly demonstrating transitions from conventional metallic behavior with $dR/dT>0$ (with low temperature deviations) to a state with $dR/dT<0$. At the highest oxygen doses the graphene exhibits behavior consistent with 2D variable range hopping (VRH), $R \sim \exp(1/T^{1/3})$ demonstrating the transition to a strongly localized insulating state (inset Fig 7.1b). The data for lower O exposures and for the N exposures did not show VRH behavior. Fluorine was so effective in increasing the resistance that only a few R(T) curves could be obtained before the strongly localized state was achieved.

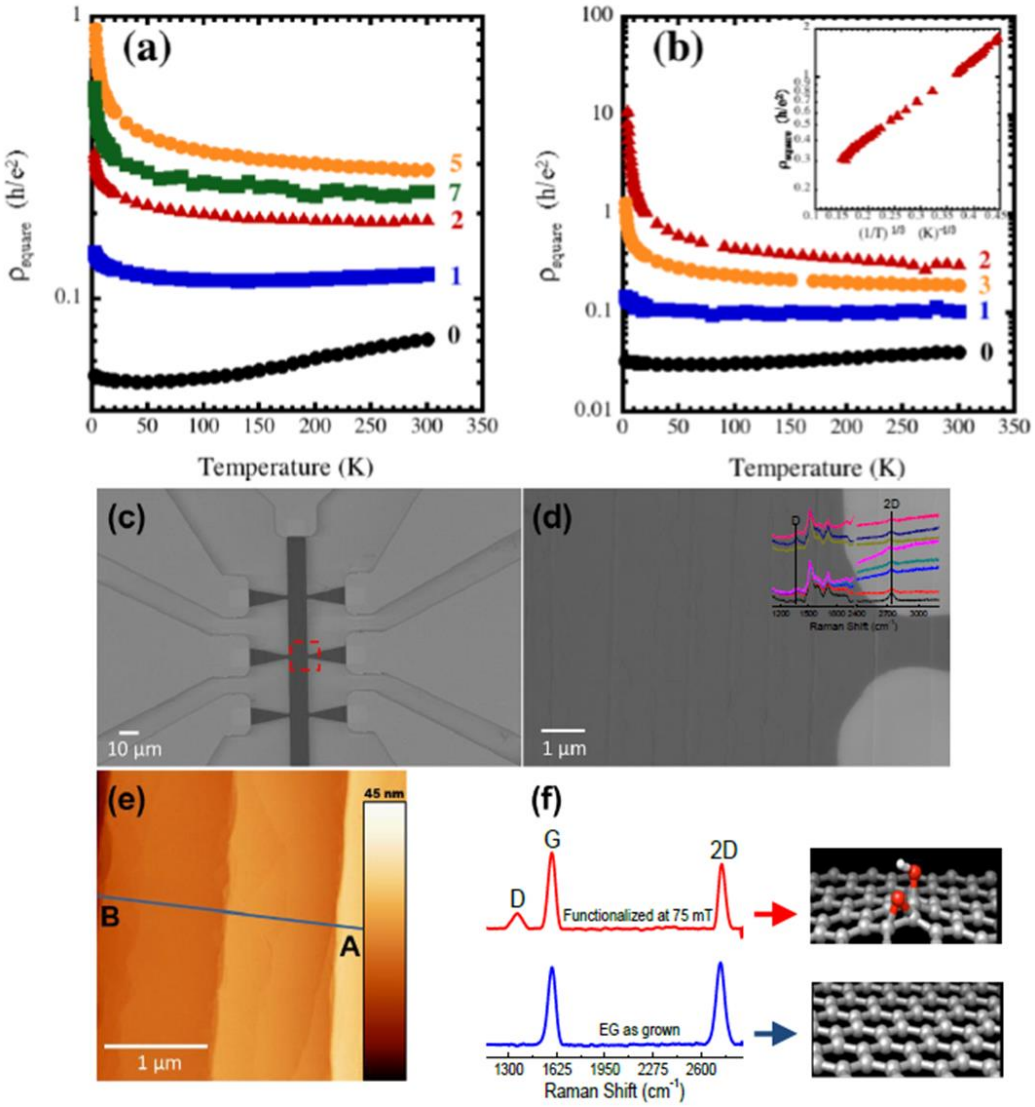

Figure 7.1: Resistance/square (plotted in units of h/e^2) for graphene exposed to (a) nitrogen and (b) oxygen. Nitrogen exposures for doses 0, 1, 2, 5, and 7 were 0, 5400, 10800, 25200, and 57600 mT-s. Oxygen exposures for doses 0-2 were 0, 300, and 7500 mT-s. Oxygen dose 3 was a 450°C anneal in vacuum for one hour. Inset (b): Log (resistance/square) vs. $(1/T)^{1/3}$, the behavior expected for 2D variable range hopping, for oxygen dose 2. (c)-(e) SEM, and AFM of representative devices. (d) inset and (f) shows Raman spectroscopy of before and after functionalization.

The original theoretical work on WL that described the three dimensional MIT[2] also predicted that all 2D systems will be insulators with $\sigma \sim \log T$. Later work indicated that this log(T) behavior would also result from enhanced electron-electron interactions in diffusive 2D systems.[122] Indeed, work on Si MOSFETS[123] and very thin films demonstrated this log(T) behavior.[124]–[128] Fig. 7.2 shows plots of conductance as a function of log(T) for the data in Fig. 7.1. These curves clearly show these samples having 2D transport characteristics at low temperatures. The relevant low temperature data were fitted to

$$\sigma=\sigma_{1K}+\sigma_2 \log T \qquad (7.1)$$

a generic function that can be used to describe 2D conductivity in disordered metals. Those fits are shown as solid lines in Fig. 7.2.

One of the key issues in understanding the MIT is the slope of the critical phase line, or "mobility edge," that describes the transition into the strongly localized state. In three dimensions, this line is usually defined as the relationship between a driving parameter, generically labeled as p, and σ_0^{3d}, the value of conductivity extrapolated to T=0.[2], [117]The usual formulation is $\sigma_0^{3d} \sim (p-p_c)^n$ where p_c is the critical value of p (where $\sigma_0^{3d}=0$) and where n is a critical exponent [2], [129]. Experimentally, p is often the carrier concentration, n. Another choice for p is the bare conductivity that can be approximated by the room temperature conductivity It has been shown that in three dimensions n=1/2 in Si:P[130] while n=1 in disordered metals. [2], [124].

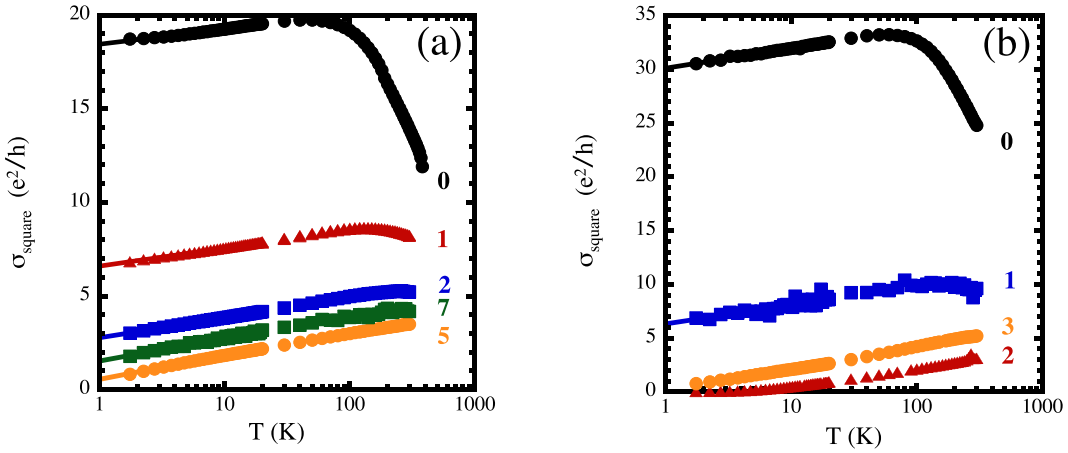

Figure 7.2: Conductivity per square plotted vs. logT as a function of dose for the data in figure 1. The solid lines are extrapolated fits to $\sigma=\sigma_0+\sigma_1 \log T$ for T<10K.

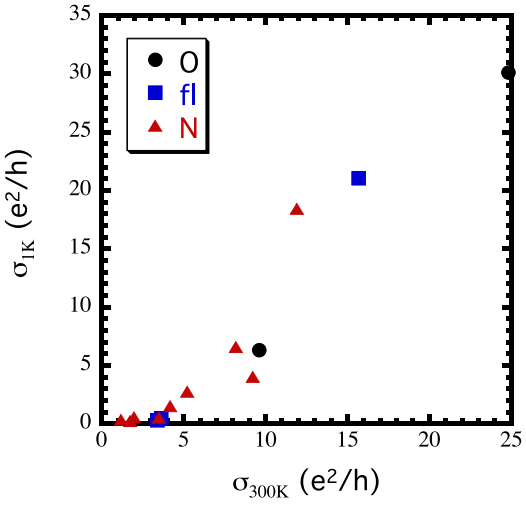

Figure 7.3: Conductivity at 1K vs. conductivity at 300K showing the continuous nature of the conductivity as the sample approaches the MIT similar to the linear "mobility edge" observed in many three dimensional systems.

In two dimensions, the data analysis is complicated by the fact that the data cannot be extrapolated to T=0. In this case, one can use σ_{1K} from equation 1 as an analog so the relevant expression becomes $\sigma_{1K} \sim (\sigma_{300K} - \sigma_c)^n$ where σ_c is the value of σ_{300K} for which $\sigma_{1K}=0$. The mobility edge is plotted in Fig.7.3 using data from the three types of exposures. The plot clearly shows that the transition is continuous with n=1, similar to many disordered 3-d systems. Furthermore, since the 2D Drude conductivity, $\sigma_{2D}=(e^2/h)k_F l$, the position of the critical room temperature conductivity indicates that the transition into the strongly localized state occurs for $k_F l \sim 3$ (assuming that the room temperature conductivity equals the Drude, or unrenormalized, conductivity).

7.3 Weak-localization vs. enhance electron-electron interactions

There have been several theoretical approaches for describing diffusive transport in disordered 2D conductors using scaling.[2], [122], [131], [132] These models predict insulating behavior in 2D. However, they require the suppression of WL, either by strong spin flip scattering, strong spin-orbit coupling, or a strong internal magnetic field (like in a ferromagnet) leaving EEI as the relevant phenomenon near the MIT.

Magneto-transport measurements, including the Hall resistance, provide a means to distinguish between the contributions of WL and EEI to conductance. Previous work on samples far from the insulating phase has demonstrated a wide variety of behaviors that include WL and/or EEI corrections to the conductance[108], [109], [115].

None of those studies considered samples close to the strongly localized state. For these functionalized samples the Hall resistance, R_{Hall} showed a log(T) temperature dependence at low temperatures. This behavior is consistent with that described by Altshuler and Aronov for EEI in disordered systems[122]

$$\frac{\Delta R_{Hall}}{R_{Hall}} = g\frac{\Delta R}{R} \qquad (7.2)$$

where $\gamma=0$ for no EEI,[133] $\gamma=2$ for EEI, and $\gamma>2$ if there are spin-orbit interactions. The values of γ at 1.75K were determined from the slopes of the R (T) and $R_{Hall}(T)$ data below 10K. These results are plotted in Fig. 7.4 as a function of σ_{1K}, a measure of the distance to the exponentially localized state. It is apparent that $\gamma<2$ with a clear trend in which γ approaches 0 as the system approaches the exponentially localized state. This is in contrast to the results reported by Lara-Avila, *et al.*[108] who found $\gamma\geq2$. The source of this discrepancy may be the fact that the mobilities of the samples studied in ref. 20 were ~6000-7000 $cm^2/(V\text{-}s)$ which is 10-100 times larger than those measured in this work. The systematic decrease in γ as the system approaches the strongly localized phase is similar to behavior observed in Si MOSFETS where $\gamma\sim2$ for low channel resistance but approached 1 as the channel resistance increased.[134] Thus, the Hall resistance results imply that the influence of EEI decreases as the system approaches the strongly localized phase and that transport properties should be dominated by WL.

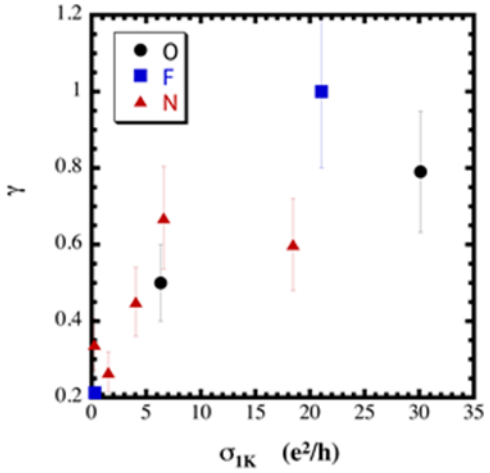

Figure7.4: The ratio $\gamma=(\Delta R_{Hall}/R_{Hall})/(\Delta R/R)$ at 1.75K as a function of σ_{1K}, a measure of the distance to the exponentially localized state.

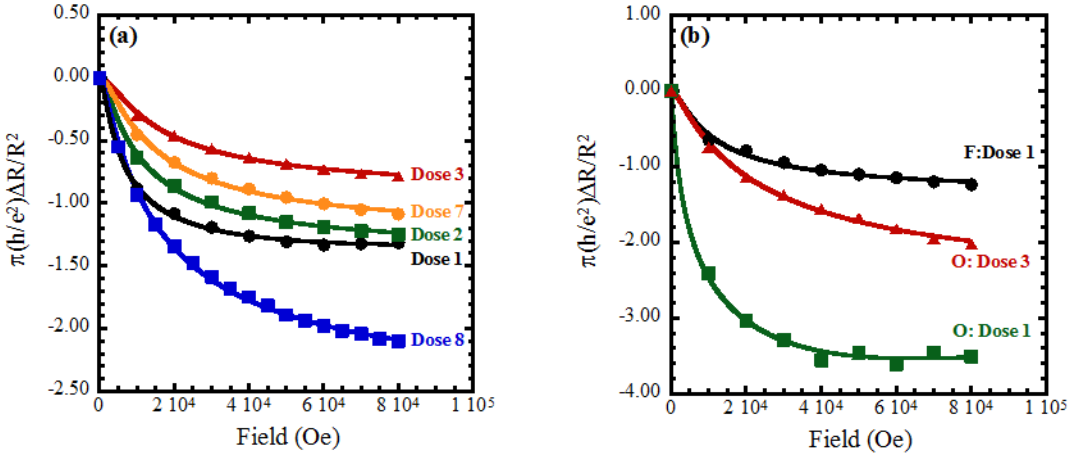

Figure 7.5: Magneto-resistance data obtained at 1.75K for (a) nitrogen, oxygen (b), and fluorine plasma doses (b). Exposures and σ(1K) for different doses. The solid lines are fits to the weak-localization model of McCann, *et al*. [135]

Magneto-resistance (MR) measurements, which are also influenced by WL and EEI, were performed simultaneous to the Hall measurements to further explore this question. Fig. 7.5 shows the MR results at 1.75K for the various plasma exposures plotted in the manner suggested by the theory of McCann, *et al.*[135] In that theory, the expression for the MR, $\Delta\rho(B) = \rho(B) - \rho(0)$, is

$$\Delta\rho(B) = -\frac{e^2\rho^2}{\pi h}\left[F\left(\frac{B}{B_\varphi}\right) - F\left(\frac{B}{B_\varphi + 2B_i}\right) - 2F\left(\frac{B}{B_\varphi + B_*}\right)\right] \tag{7.3}$$

where *F* is a function containing the natural logarithm and the digamma function,

$$F(z) = \ln(z) + \psi\left(\frac{1}{2} + \frac{1}{z}\right). \tag{7.4}$$

The terms in (3), which reflect the contributions of various diagrams, are such that neglect of certain diagrams, and thereby terms in (3), will neglect sizable effects, and so such approximations were avoided. Subscripted magnetic fields in the ratios the function *F* operates on, utilizing dimensionless quantities, are simply the effective magnetic representations of the relaxation times,

$$B_\varphi = \frac{\hbar c}{4De\tau_\varphi} \quad ; \quad B_i = \frac{\hbar c}{4De\tau_{inter}} \quad ; \quad B_* = \frac{\hbar c}{4De\tau_*} \tag{7.5}$$

where τ_{φ} and τ_{inter} are the relaxation times for inelastic decoherence and intervalley scattering, respectively, and intravalley scattering and trigonal warping are folded into intervalley scattering through

$$\tau_*^{-1} = \tau_{warp}^{-1} + \tau_{intra}^{-1} + \tau_{inter}^{-1} \quad . \qquad (7.6)$$

We note that the curves in Fig. 7.5 are for ρ_{xx} data. Formally, the inverse of the conductivity tensor should be used[109] but the contribution of ρ_{xy} is negligible and can be ignored. The plots clearly have the shape and negative MR that is characteristic of WL. In contrast, for EEI the MR is characterized by a B^2 magnetic field dependence [109], [136] and is usually positive.[2]. The solid lines in Fig. 7.5 are fits to equation 3. The characteristic time scales resulting from the fits are shown in the supplementary information. However, it must be emphasized that, while this model appears to provide a good fit to the data, the values of the parameters extracted should not be taken too seriously since the theory describes a correction to resistance of a weakly disordered metal, a situation far from that of the samples described here, which are close to the transition to the strongly localized state. The crucial finding is that, consistent with the Hall results, the MR results indicate that WL is the dominant transport phenomenon, contradicting the assumptions of the prevailing theoretical treatments of 2D disordered systems.[2], [122], [132]

In conclusion, we have demonstrated the existence of a continuous 2D MIT in epitaxial graphene consistent with a general scaling model by Dobrosavljevic´ *et al*[105].

These results clearly show that the phase diagram is analogous to that for three dimensions with the conductivity having a log(T) rather than $T^{1/2}$ dependence above the strongly localized phase. Magnetoresistance and Hall resistance measurements reveal that enhanced electron-electron interactions and WL and EEI effects both contribute to the transport properties but that the WL contribution dominates as the strongly localized state is approached contrary to the assumptions of the renormalization group theories that are believed to best describe 2D disordered systems. These results indicate that a new theoretical approach that is based on WL is needed to describe the MIT in two dimensions.

Future Work

In this work the implantation dose, sample preparation and the post-implantation annealing parameters for 4H-SiC have been optimized to obtain low surface roughness, low defect concentrations and ultra-low sheet resistivity for both n and p type materials, all of which are necessary components for high performance bipolar devices.

The future work would involve fabricating fully ion-implanted bipolar junction transistors and lateral *p-i-n* diodes employing such optimized parameters with the hope of improving the inversion layer mobilities in MOSFETs, and increasing the breakdown voltage and decreasing the on-resistance of the *p-i-n* diodes.

In graphene technology, employing the resist free technique, the intrinsic and extrinsic components of the graphene-metal interface carrier transmission as well as the work function dependence of contact resistance can be explored. Moreover the polymer assisted clean process can be employed to enhance graphene based devices such as RF transistors or THz detectors. The low-density plasma mediated disordered graphene could be employed to explore the validity of the scaling theory that predicts non-linear length dependent conductivity (σ) in 2D.

As the temperature required to activate implanted dopants in SiC and Si sublimation facilitated graphene growth are in close proximity, it opens up the possibility to fabricate both graphene and SiC planar or vertical devices on the same chip. Such technology will

exploit the high temperature and high voltage performance of SiC and the extraordinary electrical and optical properties of graphene.

REFERENCES

[1] P. Anderson, “Absence of Diffusion in Certain Random Lattices,” *Phys. Rev.*, vol. 109, no. 5, pp. 1492–1505, Mar. 1958.

[2] P. A. Lee and T. V. Ramakrishnan, “Disordered electronic systems,” *Rev. Mod. Phys.*, vol. 57, no. 2, pp. 287–337, Apr. 1985.

[3] N. F. Mott, “Conduction in non-Crystalline systems,” *Philos. Mag.*, vol. 22, no. 175, pp. 7–29, Jul. 1970.

[4] S. Baranovski, *Charge Transport in Disordered Solids with Applications in Electronics*. John Wiley & Sons, 2006.

[5] N. F. MOTT, “Metal-Insulator Transition,” *Rev. Mod. Phys.*, vol. 40, no. 4, pp. 677–683, Oct. 1968.

[6] R. Landauer, “Electrical resistance of disordered one-dimensional lattices,” *Philos. Mag.*, vol. 21, no. 172, pp. 863–867, 1970.

[7] E. Abrahams, “Scaling Theory of Localization: Absence of Quantum Diffusion in Two Dimensions,” *Phys. Rev. Lett.*, vol. 42, no. 10, pp. 673–676, Mar. 1979.

[8] M. Schadt, G. Pensl, R. P. Devaty, W. J. Choyke, R. Stein, and D. Stephani, “Anisotropy of the electron Hall mobility in 4H, 6H, and 15R silicon carbide,” *Appl. Phys. Lett.*, vol. 65, no. 24, pp. 3120–3122, Dec. 1994.

[9] H. Iwata, K. M. Itoh, and G. Pensl, “Theory of the anisotropy of the electron Hall mobility in n-type 4H– and 6H–SiC,” *J. Appl. Phys.*, vol. 88, no. 4, pp. 1956–1961, Aug. 2000.

[10] Y. Negoro, K. Katsumoto, T. Kimoto, and H. Matsunami, “Electronic behaviors of high-dose phosphorus-ion implanted 4H–SiC (0001),” *J. Appl. Phys.*, vol. 96, no. 1, pp. 224–228, Jul. 2004.

[11] A. Poggi, F. Bergamini, R. Nipoti, S. Solmi, M. Canino, and A. Carnera, “Effects of heating ramp rates on the characteristics of Al implanted 4H–SiC junctions,” *Appl. Phys. Lett.*, vol. 88, no. 16, p. 162106, Apr. 2006.

[12] R. Nipoti, A. Carnera, F. Bergamini, M. Canino, A. Poggi, S. Solmi, and M. Passini, "Ion Implanted p+/n 4H-SiC Junctions: effect of the Heating Rate during Post Implantation Annealing," in *Symposium B – Silicon Carbide 2006 – Materials, Processing and Devices*, 2006, vol. 911.

[13] S. G. Sundaresan, M. V. Rao, Y. Tian, J. A. Schreifels, M. C. Wood, K. A. Jones, and A. V. Davydov, "Comparison of Solid-State Microwave Annealing with Conventional Furnace Annealing of Ion-Implanted SiC," *J. Electron. Mater.*, vol. 36, no. 4, pp. 324–331, Apr. 2007.

[14] S. G. Sundaresan, Y. Tian, M. C. Ridgway, N. A. Mahadik, S. B. Qadri, and M. V. Rao, "Solid-state microwave annealing of ion-implanted 4H–SiC," *Nucl. Instrum. Methods Phys. Res. Sect. B Beam Interact. Mater. At.*, vol. 261, no. 1–2, pp. 616–619, Aug. 2007.

[15] S. G. Sundaresan, N. A. Mahadik, S. B. Qadri, J. A. Schreifels, Y.-L. Tian, Q. Zhang, E. Gomar-Nadal, and M. V. Rao, "Ultra-low resistivity Al+ implanted 4H–SiC obtained by microwave annealing and a protective graphite cap," *Solid-State Electron.*, vol. 52, no. 1, pp. 140–145, Jan. 2008.

[16] M. V. Rao, J. A. Gardner, P. H. Chi, O. W. Holland, G. Kelner, J. Kretchmer, and M. Ghezzo, "Phosphorus and boron implantation in 6H–SiC," *J. Appl. Phys.*, vol. 81, no. 10, pp. 6635–6641, May 1997.

[17] M. A. Capano, R. Santhakumar, R. Venugopal, M. R. Melloch, and J. A. C. Jr, "Phosphorus implantation into 4H-silicon carbide," *J. Electron. Mater.*, vol. 29, no. 2, pp. 210–214, Feb. 2000.

[18] M. Laube, F. Schmid, G. Pensl, G. Wagner, M. Linnarsson, and M. Maier, "Electrical activation of high concentrations of N+ and P+ ions implanted into 4H–SiC," *J. Appl. Phys.*, vol. 92, no. 1, pp. 549–554, Jul. 2002.

[19] S. G. Sundaresan, M. V. Rao, Y. Tian, M. C. Ridgway, J. A. Schreifels, and J. J. Kopanski, "Ultrahigh-temperature microwave annealing of Al+- and P+-implanted 4H-SiC," *J. Appl. Phys.*, vol. 101, no. 7, p. 073708, Apr. 2007.

[20] E. M. Handy, M. V. Rao, O. W. Holland, K. A. Jones, M. A. Derenge, and N. Papanicolaou, "Variable-dose (1017–1020 cm−3) phosphorus ion implantation into 4H–SiC," *J. Appl. Phys.*, vol. 88, no. 10, pp. 5630–5634, Nov. 2000.

[21] Y. Tian and M. Y. Tian, "Method and apparatus for rapid thermal processing and bonding of materials using rf and microwaves," US20090255926 A1, 15-Oct-2009.

[22] M. S. Janson, M. K. Linnarsson, A. Hallén, and B. G. Svensson, "Ion implantation range distributions in silicon carbide," *J. Appl. Phys.*, vol. 93, no. 11, pp. 8903–8909, Jun. 2003.

[23] R. Nipoti, F. Mancarella, F. Moscatelli, R. Rizzoli, S. Zampolli, and M. Ferri, "Carbon-Cap for Ohmic Contacts on Ion-Implanted 4H – SiC," *Electrochem. Solid-State Lett.*, vol. 13, no. 12, pp. H432–H435, Dec. 2010.

[24] R. Chwang, B. J. Smith, and C. R. Crowell, "Contact size effects on the van der Pauw method for resistivity and Hall coefficient measurement," *Solid-State Electron.*, vol. 17, no. 12, pp. 1217–1227, Dec. 1974.

[25] G. Rutsch, R. P. Devaty, W. J. Choyke, D. W. Langer, and L. B. Rowland, "Measurement of the Hall scattering factor in 4H and 6H SiC epilayers from 40 to 290 K and in magnetic fields up to 9 T," *J. Appl. Phys.*, vol. 84, no. 4, pp. 2062–2064, Aug. 1998.

[26] J. Pernot, W. Zawadzki, S. Contreras, J. L. Robert, E. Neyret, and L. D. Cioccio, "Electrical transport in n-type 4H silicon carbide," *J. Appl. Phys.*, vol. 90, no. 4, pp. 1869–1878, Aug. 2001.

[27] M. Bockstedte, A. Mattausch, and O. Pankratov, "Solubility of nitrogen and phosphorus in 4H-SiC: A theoretical study," *Appl. Phys. Lett.*, vol. 85, no. 1, pp. 58–60, Jul. 2004.

[28] J. Senzaki, K. Fukuda, and K. Arai, "Influences of postimplantation annealing conditions on resistance lowering in high-phosphorus-implanted 4H–SiC," *J. Appl. Phys.*, vol. 94, no. 5, pp. 2942–2947, Sep. 2003.

[29] J. Pernot, S. Contreras, J. Camassel, J. L. Robert, W. Zawadzki, E. Neyret, and L. D. Cioccio, "Free electron density and mobility in high-quality 4H–SiC," *Appl. Phys. Lett.*, vol. 77, no. 26, pp. 4359–4361, Dec. 2000.

[30] H. Matsunami and T. Kimoto, "Step-controlled epitaxial growth of SiC: High quality homoepitaxy," *Mater. Sci. Eng. R Rep.*, vol. 20, no. 3, pp. 125–166, Aug. 1997.

[31] D. M. Caughey and R. E. Thomas, "Carrier mobilities in silicon empirically related to doping and field," *Proc. IEEE*, vol. 55, no. 12, pp. 2192–2193, Dec. 1967.

[32] T. T. Mnatsakanov, L. I. Pomortseva, and S. N. Yurkov, "Semiempirical model of carrier mobility in silicon carbide for analyzing its dependence on temperature and doping level," *Semiconductors*, vol. 35, no. 4, pp. 394–397, Apr. 2001.

[33] E. Albertazzi and G. Lulli, “Monte Carlo simulation of ion implantation in crystalline SiC,” *Nucl. Instrum. Methods Phys. Res. Sect. B Beam Interact. Mater. At.*, vol. 120, no. 1–4, pp. 147–150, Dec. 1996.

[34] E. Morvan, P. Godignon, J. Montserrat, D. Flores, X. Jorda, and M. Vellvehi, “Mapping of 6H-SiC for implantation control,” *Diam. Relat. Mater.*, vol. 8, no. 2–5, pp. 335–340, Mar. 1999.

[35] G. Lulli, “Two-Dimensional Simulation of Undermask Penetration in 4H-SiC Implanted With Ions,” *IEEE Trans. Electron Devices*, vol. 58, no. 1, pp. 190–194, Jan. 2011.

[36] G. Lulli, E. Albertazzi, R. Nipoti, M. Bianconi, and A. Carnera, “The Monte Carlo Binary Collision Approximation Applied to the Simulation of the Ion Implantation Process in Single Crystal SiC: High Dose Effects,” *Mater. Sci. Forum*, vol. 353–356, pp. 599–602, 2001.

[37] L. Storasta and H. Tsuchida, “Reduction of traps and improvement of carrier lifetime in 4H-SiC epilayers by ion implantation,” *Appl. Phys. Lett.*, vol. 90, no. 6, p. 062116, Feb. 2007.

[38] Y. Negoro, T. Kimoto, H. Matsunami, F. Schmid, and G. Pensl, “Electrical activation of high-concentration aluminum implanted in 4H-SiC,” *J. Appl. Phys.*, vol. 96, no. 9, pp. 4916–4922, Nov. 2004.

[39] A. Koizumi, J. Suda, and T. Kimoto, “Temperature and doping dependencies of electrical properties in Al-doped 4H-SiC epitaxial layers,” *J. Appl. Phys.*, vol. 106, no. 1, p. 013716, Jul. 2009.

[40] G. Pensl, F. Schmid, F. Ciobanu, M. Laube, S. A. Reshanov, N. Schulze, K. Semmelroth, A. Schöner, G. Wagner, and H. Nagasawa, “Electrical and Optical Characterization of SiC,” *Mater. Sci. Forum*, vol. 433–436, pp. 365–370, 2003.

[41] M. Rambach, F. Schmid, M. Krieger, L. Frey, A. J. Bauer, G. Pensl, and H. Ryssel, “Implantation and annealing of aluminum in 4H silicon carbide,” *Nucl. Instrum. Methods Phys. Res. Sect. B Beam Interact. Mater. At.*, vol. 237, no. 1–2, pp. 68–71, Aug. 2005.

[42] R. Nipoti, A. Nath, Y. L. Tian, F. Tamarri, F. Moscatelli, P. De Nicola, and M. V. Rao, “Fully Ion Implanted Vertical p-i-n Diodes on High Purity Semi-Insulating 4H-SiC Wafers,” *Mater. Sci. Forum*, vol. 717–720, pp. 985–988, May 2012.

[43] V. Heera, A. Mücklich, C. Dubois, M. Voelskow, and W. Skorupa, “Layer morphology and Al implant profiles after annealing of supersaturated, single-

crystalline, amorphous, and nanocrystalline SiC," *J. Appl. Phys.*, vol. 96, no. 5, pp. 2841–2852, Sep. 2004.

[44] A. Parisini and R. Nipoti, "Analysis of the hole transport through valence band states in heavy Al doped 4H-SiC by ion implantation," *J. Appl. Phys.*, vol. 114, no. 24, p. 243703, Dec. 2013.

[45] A. Nath, M. V. Rao, Y.-L. Tian, A. Parisini, and R. Nipoti, "Microwave Annealing of High Dose Al+-implanted 4H-SiC: Towards Device Fabrication," *J. Electron. Mater.*, vol. 43, no. 4, pp. 843–849, Apr. 2014.

[46] M. K. Linnarsson, U. Zimmermann, J. Wong-Leung, A. Schöner, M. S. Janson, C. Jagadish, and B. G. Svensson, "Solubility limits of dopants in 4H–SiC," *Appl. Surf. Sci.*, vol. 203–204, pp. 427–432, Jan. 2003.

[47] V. Heera, K. N. Madhusoodanan, W. Skorupa, C. Dubois, and H. Romanus, "A comparative study of the electrical properties of heavily Al implanted, single crystalline and nanocrystalline SiC," *J. Appl. Phys.*, vol. 99, no. 12, p. 123716, Jun. 2006.

[48] T. Hatakeyama, M. Kushibe, T. Watanabe, S. Imai, and T. Shinohe, "Optimum Design of a SiC Schottky Barrier Diode Considering Reverse Leakage Current due to a Tunneling Process," *Mater. Sci. Forum*, vol. 433–436, pp. 831–834, 2003.

[49] W. J. Schaffer, G. H. Negley, K. G. Irvine, and J. W. Palmour, "Conductivity Anisotropy in Epitaxial 6H and 4H Sic," in *Symposium D – Diamond, Silicon Carbide and Nitride Wide Bandgap Semiconductors*, 1994, vol. 339.

[50] S. Sasaki, J. Suda, and T. Kimoto, "Lattice mismatch and crystallographic tilt induced by high-dose ion-implantation into 4H-SiC," *J. Appl. Phys.*, vol. 111, no. 10, p. 103715, May 2012.

[51] F. Schmid, M. Krieger, M. Laube, G. Pensl, and G. Wagner, "Hall Scattering Factor for Electrons and Holes in SiC," in *Silicon Carbide*, P. D. W. J. Choyke, P. D. H. Matsunami, and D. G. Pensl, Eds. Springer Berlin Heidelberg, 2004, pp. 517–536.

[52] J. D. Wiley, "Chapter 2 Mobility of Holes in III-V Compounds," in *Semiconductors and Semimetals*, vol. Volume 10, R.K. Willardson and Albert C. Beer, Ed. Elsevier, 1975, pp. 91–174.

[53] J. Pernot, S. Contreras, and J. Camassel, "Electrical transport properties of aluminum-implanted 4H–SiC," *J. Appl. Phys.*, vol. 98, no. 2, p. 023706, Jul. 2005.

[54] P. Achatz, J. Pernot, C. Marcenat, J. Kacmarcik, G. Ferro, and E. Bustarret, “Doping-induced metal-insulator transition in aluminum-doped 4H silicon carbide,” *Appl. Phys. Lett.*, vol. 92, no. 7, pp. 072103–072103–3, Feb. 2008.

[55] A. Miller and E. Abrahams, “Impurity Conduction at Low Concentrations,” *Phys. Rev.*, vol. 120, no. 3, pp. 745–755, Nov. 1960.

[56] E. A. Davis and W. D. Compton, “Compensation Dependence of Impurity Conduction in Antimony-Doped Germanium,” *Phys. Rev.*, vol. 140, no. 6A, pp. A2183–A2194, Dec. 1965.

[57] H. Fritzsche and M. Cuevas, “Impurity Conduction in Transmutation-Doped p-Type Germanium,” *Phys. Rev.*, vol. 119, no. 4, pp. 1238–1245, Aug. 1960.

[58] A. L. Efros and M. Pollak, *Electron-Electron Interactions in Disordered Systems*. Elsevier, 1985.

[59] A. K. Geim and K. S. Novoselov, “The rise of graphene,” *Nat. Mater.*, vol. 6, no. 3, pp. 183–191, 2007.

[60] Z. Cheng, Q. Zhou, C. Wang, Q. Li, C. Wang, and Y. Fang, “Toward intrinsic graphene surfaces: a systematic study on thermal annealing and wet-chemical treatment of SiO2-supported graphene devices,” *Nano Lett.*, vol. 11, no. 2, pp. 767–771, 2011.

[61] R. Ifuku, K. Nagashio, T. Nishimura, and A. Toriumi, “The density of states of graphene underneath a metal electrode and its correlation with the contact resistivity,” *Appl. Phys. Lett.*, vol. 103, no. 3, p. 033514, Jul. 2013.

[62] D. Dragoman, “Dirac-Schrödinger transformations in contacted graphene structures,” *J. Appl. Phys.*, vol. 113, no. 21, p. 214312, 2013.

[63] Y.-C. Lin, C.-C. Lu, C.-H. Yeh, C. Jin, K. Suenaga, and P.-W. Chiu, “Graphene annealing: how clean can it be?,” *Nano Lett.*, vol. 12, no. 1, pp. 414–419, 2011.

[64] P. Blake, R. Yang, S. V. Morozov, F. Schedin, L. A. Ponomarenko, A. A. Zhukov, R. R. Nair, I. V. Grigorieva, K. S. Novoselov, and A. K. Geim, “Influence of metal contacts and charge inhomogeneity on transport properties of graphene near the neutrality point,” *Solid State Commun.*, vol. 149, no. 27, pp. 1068–1071, 2009.

[65] A. Nath, A. D. Koehler, G. G. Jernigan, V. D. Wheeler, J. K. Hite, S. C. Hernández, Z. R. Robinson, N. Y. Garces, R. L. Myers-Ward, C. R. E. Jr, D. K. Gaskill, and M. V. Rao, “Achieving clean epitaxial graphene surfaces suitable for

device applications by improved lithographic process," *Appl. Phys. Lett.*, vol. 104, no. 22, p. 224102, Jun. 2014.

[66] Y. Wu, V. Perebeinos, Y. Lin, T. Low, F. Xia, and P. Avouris, "Quantum Behavior of Graphene Transistors near the Scaling Limit," *Nano Lett.*, vol. 12, no. 3, pp. 1417–1423, Mar. 2012.

[67] J. S. Moon, M. Antcliffe, H. C. Seo, D. Curtis, S. Lin, A. Schmitz, I. Milosavljevic, A. A. Kiselev, R. S. Ross, and D. K. Gaskill, "Ultra-low resistance ohmic contacts in graphene field effect transistors," *Appl. Phys. Lett.*, vol. 100, no. 20, p. 203512, 2012.

[68] A. Hsu, H. Wang, K. K. Kim, J. Kong, and T. Palacios, "Impact of graphene interface quality on contact resistance and RF device performance," *Electron Device Lett. IEEE*, vol. 32, no. 8, pp. 1008–1010, 2011.

[69] J. A. Robinson, M. LaBella, M. Zhu, M. Hollander, R. Kasarda, Z. Hughes, K. Trumbull, R. Cavalero, and D. Snyder, "Contacting graphene," *Appl. Phys. Lett.*, vol. 98, no. 5, pp. 053103–053103, 2011.

[70] L. Peng, K. P. Pernstich, T. Shen, A. R. Walker, G. Cheng, C. A. Hacker, and C. A. Richter, "UV/Ozone treatment to reduce metal-graphene contact resistance," *ArXiv Prepr. ArXiv12120838*, 2012.

[71] J. T. Smith, A. D. Franklin, D. B. Farmer, and C. D. Dimitrakopoulos, "Reducing Contact Resistance in Graphene Devices through Contact Area Patterning," *ACS Nano*, vol. 7, no. 4, pp. 3661–3667, 2013.

[72] L. Wang, I. Meric, P. Y. Huang, Q. Gao, Y. Gao, H. Tran, T. Taniguchi, K. Watanabe, L. M. Campos, and D. A. Muller, "One-dimensional electrical contact to a two-dimensional material," *Science*, vol. 342, no. 6158, pp. 614–617, 2013.

[73] C. Gong, S. McDonnell, X. Qin, A. Azcatl, H. Dong, Y. J. Chabal, K. Cho, and R. M. Wallace, "Realistic Metal–Graphene Contact Structures," *ACS Nano*, 2013.

[74] S. Yang, P. Zhou, L. Chen, Q. Sun, P. Wang, S. Ding, A. Jiang, and D. W. Zhang, "Direct observation of the work function evolution of graphene-two-dimensional metal contacts," *J. Mater. Chem. C*, Aug. 2014.

[75] S. M. Song, J. K. Park, O. J. Sul, and B. J. Cho, "Determination of Work Function of Graphene under a Metal Electrode and Its Role in Contact Resistance," *Nano Lett.*, vol. 12, no. 8, pp. 3887–3892, Aug. 2012.

[76] K. Nagashio, R. Ifuku, T. Moriyama, T. Nishimura, and A. Toriumi, "Intrinsic graphene/metal contact," in *Electron Devices Meeting (IEDM), 2012 IEEE International*, 2012, pp. 4–1.

[77] W. S. Leong, C. T. Nai, and J. T. L. Thong, "What Does Annealing Do to Metal–Graphene Contacts?," *Nano Lett.*, vol. 14, no. 7, pp. 3840–3847, Jul. 2014.

[78] M. D. Henry, "ICP etching of silicon for micro and nanoscale devices," California Institute of Technology, 2010.

[79] M. Currie, J. D. Caldwell, F. J. Bezares, J. Robinson, T. Anderson, H. Chun, and M. Tadjer, "Quantifying pulsed laser induced damage to graphene," *Appl. Phys. Lett.*, vol. 99, no. 21, p. 211909, Nov. 2011.

[80] Y. Zhou, Q. Bao, B. Varghese, L. A. L. Tang, C. K. Tan, C.-H. Sow, and K. P. Loh, "Microstructuring of graphene oxide nanosheets using direct laser writing," *Adv. Mater.*, vol. 22, no. 1, pp. 67–71, 2010.

[81] S. Datta, *Electronic transport in mesoscopic systems*. Cambridge university press, 1997.

[82] F. Xia, V. Perebeinos, Y. Lin, Y. Wu, and P. Avouris, "The origins and limits of metal-graphene junction resistance," *Nat. Nanotechnol.*, vol. 6, no. 3, pp. 179–184, 2011.

[83] E. Cobas, A. L. Friedman, O. M. J. van't Erve, J. T. Robinson, and B. T. Jonker, "Graphene As a Tunnel Barrier: Graphene-Based Magnetic Tunnel Junctions," *Nano Lett.*, vol. 12, no. 6, pp. 3000–3004, Jun. 2012.

[84] G. Giovannetti, P. A. Khomyakov, G. Brocks, V. M. Karpan, J. Van den Brink, and P. J. Kelly, "Doping graphene with metal contacts," *Phys. Rev. Lett.*, vol. 101, no. 2, p. 026803, 2008.

[85] A. N. Sidorov, K. Gaskill, M. B. Nardelli, J. L. Tedesco, R. L. Myers-Ward, C. R. Eddy Jr, T. Jayasekera, K. W. Kim, R. Jayasingha, and A. Sherehiy, "Charge transfer equilibria in ambient-exposed epitaxial graphene on (0001) 6 H-SiC," *J. Appl. Phys.*, vol. 111, no. 11, p. 113706, 2012.

[86] M. Ishigami, J. H. Chen, W. G. Cullen, M. S. Fuhrer, and E. D. Williams, "Atomic structure of graphene on SiO2," *Nano Lett.*, vol. 7, no. 6, pp. 1643–1648, 2007.

[87] J. Moser, A. Barreiro, and A. Bachtold, "Current-induced cleaning of graphene," *Appl. Phys. Lett.*, vol. 91, no. 16, p. 163513, 2007.

[88] Y.-D. Lim, D.-Y. Lee, T.-Z. Shen, C.-H. Ra, J.-Y. Choi, and W. J. Yoo, "Si-compatible cleaning process for graphene using low-density inductively coupled plasma," *ACS Nano*, vol. 6, no. 5, pp. 4410–4417, 2012.

[89] J. Lee, Y. Kim, H.-J. Shin, C. Lee, D. Lee, C.-Y. Moon, J. Lim, and S. C. Jun, "Clean transfer of graphene and its effect on contact resistance," *Appl. Phys. Lett.*, vol. 103, no. 10, p. 103104, 2013.

[90] L. O. Nyakiti, V. D. Wheeler, N. Y. Garces, R. L. Myers-Ward, C. R. Eddy, and D. K. Gaskill, "Enabling graphene-based technologies: Toward wafer-scale production of epitaxial graphene," *MRS Bull.*, vol. 37, no. 12, pp. 1149–1157, 2012.

[91] M. T. Ghoneim, C. E. Smith, and M. M. Hussain, "Simplistic graphene transfer process and its impact on contact resistance," *Appl. Phys. Lett.*, vol. 102, no. 18, p. 183115, 2013.

[92] V. Wheeler, N. Garces, L. Nyakiti, R. Myers-Ward, G. Jernigan, J. Culbertson, C. Eddy Jr, and D. Kurt Gaskill, "Fluorine functionalization of epitaxial graphene for uniform deposition of thin high-κ dielectrics," *Carbon*, vol. 50, no. 6, pp. 2307–2314, 2012.

[93] V. K. Nagareddy, I. P. Nikitina, D. K. Gaskill, J. L. Tedesco, R. L. Myers-Ward, C. R. Eddy, J. P. Goss, N. G. Wright, and A. B. Horsfall, "High temperature measurements of metal contacts on epitaxial graphene," *Appl. Phys. Lett.*, vol. 99, no. 7, p. 073506, 2011.

[94] M. K. Yakes, D. Gunlycke, J. L. Tedesco, P. M. Campbell, R. L. Myers-Ward, C. R. Eddy Jr, D. K. Gaskill, P. E. Sheehan, and A. R. Laracuente, "Conductance anisotropy in epitaxial graphene sheets generated by substrate interactions," *Nano Lett.*, vol. 10, no. 5, pp. 1559–1562, 2010.

[95] Z. Guo, R. Dong, P. S. Chakraborty, N. Lourenco, J. Palmer, Y. Hu, M. Ruan, J. Hankinson, J. Kunc, and J. D. Cressler, "Record maximum oscillation frequency in C-face epitaxial graphene transistors," *Nano Lett.*, vol. 13, no. 3, pp. 942–947, 2013.

[96] A. H. Castro Neto, F. Guinea, N. M. R. Peres, K. S. Novoselov, and A. K. Geim, "The electronic properties of graphene," *Rev. Mod. Phys.*, vol. 81, no. 1, pp. 109–162, Jan. 2009.

[97] S. Das Sarma, S. Adam, E. H. Hwang, and E. Rossi, "Electronic transport in two-dimensional graphene," *Rev. Mod. Phys.*, vol. 83, no. 2, pp. 407–470, May 2011.

[98] M. S. Fuhrer, “Critical Mass in Graphene,” *Science*, vol. 340, no. 6139, pp. 1413–1414, Jun. 2013.

[99] B. Hunt, J. D. Sanchez-Yamagishi, A. F. Young, M. Yankowitz, B. J. LeRoy, K. Watanabe, T. Taniguchi, P. Moon, M. Koshino, P. Jarillo-Herrero, and R. C. Ashoori, “Massive Dirac Fermions and Hofstadter Butterfly in a van der Waals Heterostructure,” *Science*, vol. 340, no. 6139, pp. 1427–1430, Jun. 2013.

[100] E. Tiras, S. Ardali, T. Tiras, E. Arslan, S. Cakmakyapan, O. Kazar, J. Hassan, E. Janzén, and E. Ozbay, “Effective mass of electron in monolayer graphene: Electron-phonon interaction,” *J. Appl. Phys.*, vol. 113, no. 4, p. 043708, Jan. 2013.

[101] S. V. Kravchenko, G. V. Kravchenko, J. E. Furneaux, V. M. Pudalov, and M. D’Iorio, “Possible metal-insulator transition at B=0 in two dimensions,” *Phys. Rev. B*, vol. 50, no. 11, pp. 8039–8042, Sep. 1994.

[102] A. Ohtomo and H. Y. Hwang, “A high-mobility electron gas at the LaAlO3/SrTiO3 heterointerface,” *Nature*, vol. 427, no. 6973, pp. 423–426, Jan. 2004.

[103] A. Punnoose and A. M. Finkel’stein, “Metal-Insulator Transition in Disordered Two-Dimensional Electron Systems,” *Science*, vol. 310, no. 5746, pp. 289–291, Oct. 2005.

[104] S. Anissimova, S. V. Kravchenko, A. Punnoose, A. M. Finkel’stein, and T. M. Klapwijk, “Flow diagram of the metal–insulator transition in two dimensions,” *Nat. Phys.*, vol. 3, no. 10, pp. 707–710, Oct. 2007.

[105] V. Dobrosavljević, E. Abrahams, E. Miranda, and S. Chakravarty, “Scaling Theory of Two-Dimensional Metal-Insulator Transitions,” *Phys. Rev. Lett.*, vol. 79, no. 3, pp. 455–458, Jul. 1997.

[106] J.-H. Chen, W. G. Cullen, C. Jang, M. S. Fuhrer, and E. D. Williams, “Defect Scattering in Graphene,” *Phys. Rev. Lett.*, vol. 102, no. 23, p. 236805, Jun. 2009.

[107] A. Bostwick, J. L. McChesney, K. V. Emtsev, T. Seyller, K. Horn, S. D. Kevan, and E. Rotenberg, “Quasiparticle Transformation during a Metal-Insulator Transition in Graphene,” *Phys. Rev. Lett.*, vol. 103, no. 5, p. 056404, Jul. 2009.

[108] S. Lara-Avila, A. Tzalenchuk, S. Kubatkin, R. Yakimova, T. J. B. M. Janssen, K. Cedergren, T. Bergsten, and V. Fal’ko, “Disordered Fermi Liquid in Epitaxial Graphene from Quantum Transport Measurements,” *Phys. Rev. Lett.*, vol. 107, no. 16, p. 166602, Oct. 2011.

[109] B. Jouault, B. Jabakhanji, N. Camara, W. Desrat, C. Consejo, and J. Camassel, "Interplay between interferences and electron-electron interactions in epitaxial graphene," *Phys. Rev. B*, vol. 83, no. 19, p. 195417, May 2011.

[110] A. M. R. Baker, J. A. Alexander-Webber, T. Altebaeumer, T. J. B. M. Janssen, A. Tzalenchuk, S. Lara-Avila, S. Kubatkin, R. Yakimova, C.-T. Lin, L.-J. Li, and R. J. Nicholas, "Weak localization scattering lengths in epitaxial, and CVD graphene," *Phys. Rev. B*, vol. 86, no. 23, p. 235441, Dec. 2012.

[111] S. Pezzini, C. Cobaleda, E. Diez, and V. Bellani, "Disorder and de-coherence in graphene probed by low-temperature magneto-transport: weak localization and weak antilocalization," *J. Phys. Conf. Ser.*, vol. 456, no. 1, p. 012032, Aug. 2013.

[112] A. Mahmood, C. Naud, C. Bouvier, F. Hiebel, P. Mallet, J.-Y. Veuillen, L. P. Lévy, D. Chaussende, and T. Ouisse, "Epitaxial graphene morphologies probed by weak (anti)-localization," *J. Appl. Phys.*, vol. 113, no. 8, p. 083715, Feb. 2013.

[113] Y.-F. Chen, M.-H. Bae, C. Chialvo, T. Dirks, A. Bezryadin, and N. Mason, "Magnetoresistance in single-layer graphene: weak localization and universal conductance fluctuation studies," *J. Phys. Condens. Matter*, vol. 22, no. 20, p. 205301, May 2010.

[114] Y.-F. Chen, M.-H. Bae, C. Chialvo, T. Dirks, A. Bezryadin, and N. Mason, "Negative and positive magnetoresistance in bilayer graphene: Effects of weak localization and charge inhomogeneity," *Phys. B Condens. Matter*, vol. 406, no. 4, pp. 785–788, Feb. 2011.

[115] J. Jobst, D. Waldmann, I. V. Gornyi, A. D. Mirlin, and H. B. Weber, "Electron-Electron Interaction in the Magnetoresistance of Graphene," *Phys. Rev. Lett.*, vol. 108, no. 10, p. 106601, Mar. 2012.

[116] D. Belitz and T. R. Kirkpatrick, "The Anderson-Mott transition," *Rev. Mod. Phys.*, vol. 66, no. 2, pp. 261–380, Apr. 1994.

[117] W. L. McMillan, "Scaling theory of the metal-insulator transition in amorphous materials," *Phys. Rev. B*, vol. 24, no. 5, pp. 2739–2743, Sep. 1981.

[118] S. V. Kravchenko and M. P. Sarachik, "Metal–insulator transition in two-dimensional electron systems," *Rep. Prog. Phys.*, vol. 67, no. 1, p. 1, Jan. 2004.

[119] T. Fix, F. Schoofs, J. L. MacManus-Driscoll, and M. G. Blamire, "Charge Confinement and Doping at LaAlO3/SrTiO3 Interfaces," *Phys. Rev. Lett.*, vol. 103, no. 16, p. 166802, Oct. 2009.

[120] E. Breckenfeld, N. Bronn, J. Karthik, A. R. Damodaran, S. Lee, N. Mason, and L. W. Martin, "Effect of Growth Induced (Non)Stoichiometry on Interfacial Conductance in LaAlO3/SrTiO3," *Phys. Rev. Lett.*, vol. 110, no. 19, p. 196804, May 2013.

[121] F. J. Wong, R. V. Chopdekar, and Y. Suzuki, "Disorder and localization at the LaAlO3/SrTiO3 heterointerface," *Phys. Rev. B*, vol. 82, no. 16, p. 165413, Oct. 2010.

[122] B. L. Altshuler and A. G. Aronov, "Fermi-liquid theory of the electron-electron interaction effects in disordered metals," *Solid State Commun.*, vol. 46, no. 6, pp. 429–435, May 1983.

[123] D. J. Bishop, D. C. Tsui, and R. C. Dynes, "Nonmetallic Conduction in Electron Inversion Layers at Low Temperatures," *Phys. Rev. Lett.*, vol. 44, no. 17, pp. 1153–1156, Apr. 1980.

[124] N. Nishida, T. Furubayashi, M. Yamaguchi, M. Shinohara, Y. Miura, Y. Takano, K. Morigaki, H. Ishimoto, and K. Ono, "Transport properties of amorphous Si1−xAux: Metal-insulator transition and," *J. Non-Cryst. Solids*, vol. 59–60, Part 1, pp. 149–152, Dec. 1983.

[125] G. J. Dolan and D. D. Osheroff, "Nonmetallic Conduction in Thin Metal Films at Low Temperatures," *Phys. Rev. Lett.*, vol. 43, no. 10, pp. 721–724, Sep. 1979.

[126] D. Abraham and R. Rosenbaum, "Localization in thin copper films," *Phys. Rev. B*, vol. 27, no. 2, pp. 1409–1412, Jan. 1983.

[127] D. E. Beutler and N. Giordano, "Localization and electron-electron interaction effects in thin Bi wires and films," *Phys. Rev. B*, vol. 38, no. 1, pp. 8–19, Jul. 1988.

[128] L. Van den dries, C. Van Haesendonck, Y. Bruynseraede, and G. Deutscher, "Two-Dimensional Localization in Thin Copper Films," *Phys. Rev. Lett.*, vol. 46, no. 8, pp. 565–568, Feb. 1981.

[129] T. F. Rosenbaum, K. Andres, G. A. Thomas, and P. A. Lee, "Conductivity Cusp in a Disordered Metal," *Phys. Rev. Lett.*, vol. 46, no. 8, pp. 568–571, Feb. 1981.

[130] M. A. Paalanen, T. F. Rosenbaum, G. A. Thomas, and R. N. Bhatt, "Stress Tuning of the Metal-Insulator Transition at Millikelvin Temperatures," *Phys. Rev. Lett.*, vol. 48, no. 18, pp. 1284–1287, May 1982.

[131] C. Castellani, C. Di Castro, P. A. Lee, and M. Ma, “Interaction-driven metal-insulator transitions in disordered fermion systems,” *Phys. Rev. B*, vol. 30, no. 2, pp. 527–543, Jul. 1984.

[132] T. R. Kirkpatrick and D. Belitz, “Existence of a phase transition in Finkelshtein’s model for a disordered Fermi liquid,” *Phys. Rev. B*, vol. 40, no. 7, pp. 5227–5230, Sep. 1989.

[133] H. Fukuyama, “Hall Effect in Two-Dimensional Disorderd Systems,” *J. Phys. Soc. Jpn.*, vol. 49, no. 2, pp. 644–648, Aug. 1980.

[134] M. J. Uren, R. A. Davies, and M. Pepper, “The observation of interaction and localisation effects in a two-dimensional electron gas at low temperatures,” *J. Phys. C Solid State Phys.*, vol. 13, no. 33, p. L985, Nov. 1980.

[135] E. McCann, K. Kechedzhi, V. I. Fal’ko, H. Suzuura, T. Ando, and B. L. Altshuler, “Weak-Localization Magnetoresistance and Valley Symmetry in Graphene,” *Phys. Rev. Lett.*, vol. 97, no. 14, p. 146805, Oct. 2006.

[136] I. V. Gornyi and A. D. Mirlin, “Interaction-induced magnetoresistance in a two-dimensional electron gas,” *Phys. Rev. B*, vol. 69, no. 4, p. 045313, Jan. 2004.

BIOGRAPHY

Anindya Nath received his Bachelor of Technology from West Bengal University of Technology in 2005. He was employed as a research fellow under Department of Science and Technology, India from 2006 to 2008 before joining graduate program of George Mason University. He subsequently received his Masters in Electrical Engineering and his Ph.D. in Electrical and Computer Engineering, both from George Mason University, in December 2012, and December 2014, respectively.